Enhanced Geothermal Systems

Contact: Dan McMorrow — dmcmorrow@mitre.org

December 2013

JSR-13-320

REPORT DOCUMENTATION PAGE

1. REPORT DATE *(DD-MM-YYYY)*	2. REPORT TYPE	3. DATES COVERED *(From - To)*
December 2013	Technical	

4. TITLE AND SUBTITLE	5a. CONTRACT NUMBER
Enhanced Geothermal Systems	
	5b. GRANT NUMBER
	5c. PROGRAM ELEMENT NUMBER

6. AUTHOR(S)	5d. PROJECT NUMBER
	13139022
R. Jeanloz, H. Stone et al.	5e. TASK NUMBER
	PS
	5f. WORK UNIT NUMBER

7. PERFORMING ORGANIZATION NAME(S) AND ADDRESS(ES)	8. PERFORMING ORGANIZATION REPORT NUMBER
The MITRE Corporation JASON Program Office 7515 Colshire Drive McLean, Virginia 22102	JSR-13-320

9. SPONSORING / MONITORING AGENCY NAME(S) AND ADDRESS(ES)	10. SPONSOR/MONITOR'S ACRONYM(S)
US Department of Energy Energy Efficiency and Renewable Energy 1000 Independence Ave, SW Washington, DC 20585	
	11. SPONSOR/MONITOR'S REPORT NUMBER(S)

12. DISTRIBUTION / AVAILABILITY STATEMENT
Approved for public release

13. SUPPLEMENTARY NOTES

14. ABSTRACT

DOE, through the Geothermal Technologies Office (GTO) within the Office of Energy Efficiency and Renewable Energy, requested this study, identifying a focus on: i) assessment of technologies and approaches for subsurface imaging and characterization so as to be able to validate EGS opportunities, and ii) assessment of approaches toward creating sites for EGS, including science and engineering to enhance permeability and increase the recovery factor.

Two days of briefings provided in-depth discussion of a wide range of themes and challenges in EGS, and represented perspectives from industry, government laboratories and university researchers. JASON also contacted colleagues from universities, government labs and industry in further conversations to learn the state of the field and potential technologies relevant to EGS.

15. SUBJECT TERMS

16. SECURITY CLASSIFICATION OF:			17. LIMITATION OF ABSTRACT	18. NUMBER OF PAGES	19a. NAME OF RESPONSIBLE PERSON
					Mr. Douglas Hollett
a. REPORT	b. ABSTRACT	c. THIS PAGE	UL		19b. TELEPHONE NUMBER *(include area code)* 703-746-1453
Unclassfied	Unclassified	Unclassified			

Contents

1   EXECUTIVE SUMMARY

DOE, through the Geothermal Technologies Office (GTO), requested that JASON study Enhanced Geothermal Systems (EGS), with a focus on: i) assessment of technologies and approaches for subsurface imaging and characterization, so as to be able to validate EGS opportunities; and ii) assessment of approaches toward creating sites for EGS, including science and engineering to enhance permeability and increase the energy recovery factor.

Geothermal resources currently provide peak capacity of 3.4 GW_e (average 2.5 GW_e based on capacity factors above 70%) baseload non-carbon power in the U.S., which corresponds roughly to 0.5 percent of domestic electrical energy generation at present. EGS incorporates a range of activities, from stimulation and expansion of existing hydrothermal fields to developing methods for mining Earth's heat to depths of 1-5 km (e.g., hot dry rock).

Briefings from industry, government laboratories and university researchers, combined with independent JASON analyses and consultation with additional experts, led JASON to the following findings and recommendations.

Findings

1. Near-term (perhaps 5-10 year) geothermal potential, including from sites developed through enhanced geothermal systems, is an additional 5-10 GW_e for the U.S., with a larger potential once this success is achieved.

2. Major challenges for EGS are i) the cost of drilling, with a near-exponential increase in the cost C of drilling to depth z, $C \propto \exp(z/d)$ with d=0.5-3 km; ii) the small heat-recovery factors found in practice (about 1-5% of the heat in the reservoir at depth is recovered at the wellhead); and iii) uncertain and potentially limited lifetimes of EGS well pairs.

3. The nature of the subsurface flow network, including its variation in

space and time, presents a major technical uncertainty for EGS, affecting heat-recovery factors, production rates and well lifetimes.

4. Thermal drawdown reduces both thermal power and Carnot efficiency of EGS over time, with mitigation strategies including tailored production schedules.

5. Water availability can be a significant factor in operating geothermal plants in areas of water scarcity, and could become a limiting constraint for EGS at scale.

6. Induced seismicity i) is associated directly with geothermal operations, ii) is a partially understood hazard, and iii) offers benefits for subsurface characterization.

Recommendations

1. To pursue EGS, an integrated program of laboratory and field studies, combining experiments with modeling, simulation and theory, should be undertaken to reduce i) uncertainties in the nature of the subsurface (permeability, stress, etc.), and consequent heat-recovery factors, thermal-drawdown losses and well lifetimes; and ii) the difficulty and cost of drilling to depth. Such a program for validating methods and ideas can benefit from developing and applying recent technical advances in subsurface characterization, developed at field-scale as needed, such as: microdrilling with sensor deployment at depth; advanced seismic imaging; electromagnetic monitoring; and tracer tests.

2. The portfolio of EGS activities should at present emphasize enhancing conventional geothermal production. Combining better understanding of the subsurface with advances in well design, drilling and operational procedures provides opportunities for improved production of geothermal energy.

3. Water-use plans with realistic contingencies should be developed for EGS at scale.

4. A thorough technical evaluation of the hazards associated with induced seismicity includes continued monitoring of induced earthquakes along with targeted studies of their causes and possible mitigation.

5. Deleterious effects of corrosion and scaling of equipment and subsurface channels, by gases (e.g., HCl or H_2S mixed with steam) or by carbonates dissolved in brine should be further assessed, with ongoing development of mitigation strategies.

2 INTRODUCTION

Enhanced geothermal systems (EGS) refer to methods of harvesting energy from Earth's crust by passing fluid through a zone of enhanced permeability in rock at depth. The enhancements come from 1) drilling to sufficient depths that high temperatures are reached; 2) creating enough permeability that fluid can be flushed at significant rates through the hot rock deep in the crust, the objective being to transfer the thermal energy to the fluid without excessive loss of fluid into the rock; and 3) extracting the energy from the fluid to produce useful effects, either in terms of electricity generation or heating operations (see Figures 5-9, 5-1 and 4-8 for summaries, respectively, of typical production, heat-transfer and rock-fracture geometries).

EGS refers to a spectrum of approaches, with enhancement of conventional geothermal production at one extreme. Conventional geothermal extraction depends on naturally occurring waters bringing heat from Earth's interior to the surface. The necessary hydrothermal conditions are relatively rare, however, occurring predominantly in volcanic regions with abundant groundwater. Thus, for the U.S., conventional geothermal power supplies 2.5 GW_e at present, and the electric power generation potential from additional identified resources is estimated as about 9 GW_e (Williams, et al., 2008) [1]. Where available, conventional geothermal resources provide an attractive base-load power source that can be economically competitive without subsidies (Figure 2-1).

At the other extreme is hot dry rock, which is in principle available anywhere around the world if one drills deep enough and can appropriately stimulate the rock (i.e., create sufficient permeability) at those depths. Realistically, the target depths must be less than 7-10 km because high pressures (due to overburden) and high temperatures cause difficulties in maintaining open boreholes and controlling permeability at depth (e.g., Emmermann and Lauterjung, 1997) [2]. This is true even for cold rock, and all the more so for hot rock because the rate of plastic deformation (e.g., sealing cracks)
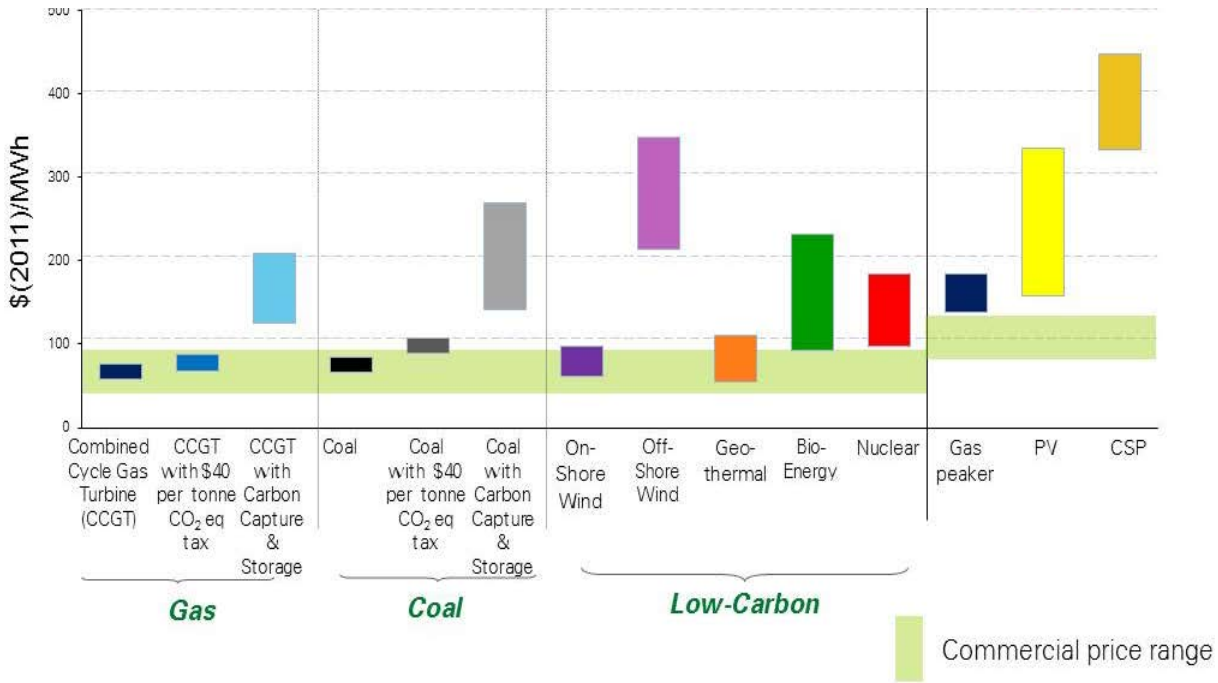
Figure 2-1: Levelized cost of electrical power production in 2011, based on new build with a commercial rate of return on capital invested, and 2011 prices for gas and coal. The orange bar is representative of currently operating geothermal resources. Source: BP Alternative Energy Strategy (similar products can be obtained from DOE-EIA)

increases exponentially with temperature (e.g., Frost and Ashby, 1982) [3].

EGS activities can range from enhancing conventional geothermal systems, in which extra fluid is flushed through a hydrothermal system (in addition to the naturally available groundwater) and perhaps with stimulation to create additional permeability, all the way to hot dry-rock (HDR) in which there would be no natural geothermal potential without artificial pumping of fluids at depth (e.g., Augustine, 2011) [4]. This spectrum of activities greatly increases the amount of thermal energy that is accessible, with the potential generating capacity from all EGS approaches estimated by Williams, et al. (2008a, b) to exceed 500 GW$_e$ for the U.S. [1, 5], which represents nearly half the current capacity from all domestic sources (AEO2013) [6].

For the present study, we consider a depth interval of 1-5 km for the rock to be stimulated. The upper limit of 5 km may be conservative in the long run, but is suggested by current capabilities in drilling through rock (Tester, et al., 2006; Williams, et al., 2008) [7, 1]. The shallow limit, $z_0 = 1$ km, reflects the needs both to access hot dry rock at depth (i.e., where groundwater is not available or effective in bringing heat to the surface) and to avoid – or at least reduce – environmental problems, with 1) contaminating potable aquifers and 2) triggering earthquakes that are felt at the surface being among key concerns. Naturally occurring temperature gradients across the U.S. reach about 80 K/km, so drilling must extend down to thousands rather than hundreds of meters in order to reach the desired high temperatures of hundreds of degrees Celsius in the crust (Ch. 2 of Tester, et al., 2006) [7].

There is now a baseline of experience in different aspects of EGS, providing a roadmap for identifying the technical issues that need to be addressed for EGS approaches to add value beyond the present U.S. conventional geothermal resource base (e.g., Ziagos, et al., 2013) [8]. Major technical issues are:

- The ability to identify well sites where the subsurface features will allow rates of water circulation across hot rock sufficient to produce economically valuable rates of water or steam production.

- The ability to design, drill and operate wells in increasingly difficult geological media for wells at the hot dry rock end of the spectrum of EGS.

- The ability to design and execute stimulation methods that optimize permeability and water exposure to hot rock.

There are significant opportunities to make progress on each of these topics due to recent advances in geophysical imaging driven both by academic and industry research, advances in drilling technologies, and rapidly developing technologies related to fracturing to stimulate fossil-fuel-bearing

rock. As will be described in subsequent sections of the report, research on these topics has the potential to impact the development of EGS methods with initial commercial impacts in enhancing conventional geothermal systems. Key areas of research opportunity include:

- Imaging and characterizing the subsurface

    - Characterization of natural fractures as paths of high permeability

    - Real-time monitoring of stimulation and intervention

    - Characterization of actual flow paths

- Drilling

    - Microhole drilling for subsurface characterization, including sensor emplacement, well intervention and stimulation, and lateral drilling from production or injection well bores

    - Hard rock drilling

- Improving permeability and extending well lifetime

    - Physical well intervention

    - Chemical well intervention

While the JASONs cannot independently substantiate projections of U.S. geothermal energy recovery to 100s of GW (addressed below, in Section 3), a well-planned technical program should allow steady progress in advancing the range of geothermal resource that is economically accessible. Technical issues and opportunities are described in more detail in Sections 4 and 5, and summarized in Section 6.

2.1 Study Charge and Process

DOE, through the Geothermal Technologies Office (GTO) within the Office of Energy Efficiency and Renewable Energy, requested this study, identifying a focus on: i) assessment of technologies and approaches for subsurface imaging and characterization so as to be able to validate EGS opportunities, and ii) assessment of approaches toward creating sites for EGS, including science and engineering to enhance permeability and increase the recovery factor.

Two days of briefings provided in-depth discussion of a wide range of themes and challenges in EGS, and represented perspectives from industry, government laboratories and university researchers. JASON also contacted colleagues from universities, government labs and industry in further conversations to learn the state of the field and potential technologies relevant to EGS.

3 ESTIMATES OF U.S. GEOTHERMAL RE-SOURCE

3.1 Geological Setting

The ultimate source of heat for EGS, as for geothermal energy more generally, is a combination of naturally occurring radioactivity and the heat associated with Earth's formation (and, to a much more limited degree, Earth's subsequent evolution: tidal effects are negligible in the current context, for example). The buildup of heat in a given volume of crust comes from local heat production due to radioactivity, as well as the net heat transport (i.e., balance of gain vs. loss of heat) into the region of interest due to conduction and advection; radiative transport is negligible (e.g., Turcotte and Schubert, 1982) [9].

Radioactive heat production is unlikely to be important at the local scale of interest for EGS, say at depths of 1-5 km over regions of lateral dimension $\sim$1-10 km. For measured values of radioactive heat production in Earth's crust (e.g., Figure 2-1 of Furlong and Chapman, 2013 [10]) the temperature rise amounts to 30 K/Myr (Table 3.1), implying tens of millions of years (Myr) being required to build up enough heat by radioactivity in order that temperature increases by hundreds of K. Meanwhile, hot crust is buoyant, so that it rises and is eroded at rates of $\approx$ 0.1-1 km/Myr (it also moves laterally at rates of $\approx$ 10 km/Myr due to plate tectonics). Therefore, as a broad generality, hot crust tends to be destroyed about as quickly as it is being produced by natural radioactivity.

Similarly, transport of heat by conduction is relatively ineffective over distances greater than tens of km. Thermal diffusion, of order 1 mm^2/s = 30 km^2/Myr (Table 3.1), shows that conductive transport is only effective over distances of $\approx$ 5.5, 55 and 370 km over time periods 1 Myr, 100 Myr and the age of the Earth (4.5×10^3 Myr), respectively.

Instead, hot crust is created most effectively by advection of heat. Solid-state convection is reflected in the large horizontal motions of plate tectonics, at velocities $\approx$ 1-10 cm/yr = 10-100 km/Myr, and associated uplift. Uplift at the rates of 0.1-1 mm/yr quoted above can bring temperatures of hundreds of degrees Celsius to within the top 10 km of Earth's crust, for example. In addition, magmas or hydrous fluids formed by partial melting can similarly transport heat upward at rates of m/yr to km/yr, causing local uplift (e.g., Stolper, et al., 1981; Jeanloz and Morris, 1986) [11, 12]. Therefore, regions with greatest EGS potential generally tend to be undergoing uplift (hence extension), reflecting the heat at depth, and/or exhibiting volcanism (reflecting fluid advection of heat through the crust).

This is very much the situation for Western North America, which shows the highest geothermal (and EGS) potential for the U.S [1, 5]. The fundamental source of heating, and associated uplift and extension of the Basin and Range, is due to subduction of the East Pacific Rise under southwestern North America starting about 30 Myr ago [13, 14]. Advection of heat from the subducted mid-ocean ridge has no doubt penetrated toward the surface in well under 10 million years, causing partial melting under the Basin and Range as well as heating and uplift of the continental crust (see also [15]).

3.2 Resource Estimates

The current geothermal electrical generation capacity in the U.S. is approximately 3.4 GW_e (with capacity factors at or above 70%), and hence the installed base provides approximately 22,000 GWh of electrical energy (1 MW_e provides 8.76 GWh in a year at 100% capacity).

In 2008, the USGS performed a thorough assessment of the domestic geothermal energy resource (Williams, et al., 2008) [1]. They identified a mean value of geothermal power generation potential of 9 GW_e from full development of known geothermal resources. The USGS assessment also estimated the electrical generation potential of undiscovered resources, based

on mapping, temperature information, and auxiliary information indicative of where geothermal resources are likely to be found. The mean estimated value of the power-producing potential from undiscovered resources located on private and accessible public lands (i.e., excluding national parks) was 30 GW_e.

Hence, the anticipated technically recoverable domestic electrical generation potential of current geothermal systems is in the range of 40 GW_e, i.e., on the order of 5% of current domestic electricity consumption on a kWh/yr basis. An economic assessment of the expanded potential of conventional geothermal prepared by NREL concludes that with present technical approaches, about one half the technically recoverable geothermal resource is economically recoverable, as illustrated in Figure 3-1.
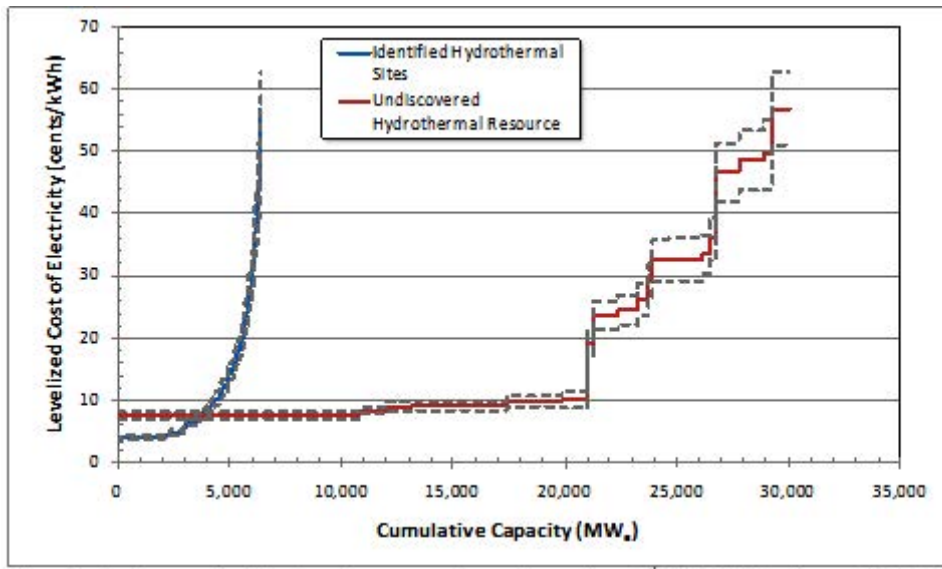
Figure 3-1: NREL supply curves for hydrothermal electricity in 2008 U.S.$ (Augustine, et al., 2010; Augustine 2011) [16, 4].

There is little question that the heat in place in the crust offers an enormous energy resource relative to current domestic annual energy consumption. The recoverable heat in place is estimated by the MIT Future of Geothermal Energy report to be on the order of 200×10^{21} J (i.e., 200 ZJ), as compared to the total U.S. primary domestic annual energy consumption

13

of 97 quadrillion Btu, i.e. $\sim 100 \times 10^{18}$ J (100 EJ) (Tester, et al., 2006) [7]. However, heat content by itself is not a useful metric of recoverable energy: thermodynamics demonstrates that heat must be delivered at sufficient temperature to allow conversion to mechanical work and thereby to electrical power. As a result, calculations of 'heat in place' only represent an upper limit, and do not identify the energy that is necessarily recoverable in practice.

Practical issues in recovering power from geothermal heat are summarized in the power equation

$$P = \rho C_p \Delta T Q \eta \qquad (3\text{-}1)$$

where ρ is the density of the circulating fluid (here usually water), C_p is the specific heat of the fluid at constant pressure, ΔT is the temperature drop across the heat exchanger in the heat engine, Q is the volume flow rate of the fluid, and η is a measure of overall efficiency (see Williams, et al., 2008 [1], for example). Both ΔT and the efficiency depend on the temperature to which the water circulating through the hot dry rock can be raised; and, with C_p in J/K/kg, the product ρ C_p has units J/K/m^3 and is referred to as the volumetric heat capacity elsewhere in this report. The flow rate Q must be restricted to a value that allows heat transfer from the rock to raise the temperature of the working fluid to the needed value. Issues in optimizing the flow rate and the deliverable fluid temperature are discussed in later sections of this report.

Experience to date with power delivery from geothermal heat, as well as the drilling and operation costs expected for a well in dry rock, allow estimates of the accessible resource from hot dry rock in economic terms. NREL cost-curves for HDR enhanced geothermal show that the cost would be much higher than conventional geothermal, at least given present technology and subsurface reservoir understanding (Figure 3-2). An important role of technology would therefore be to make economically accessible the much larger resources associated with enhanced geothermal, including HDR at depths down to 5-6 km below Earth's surface.
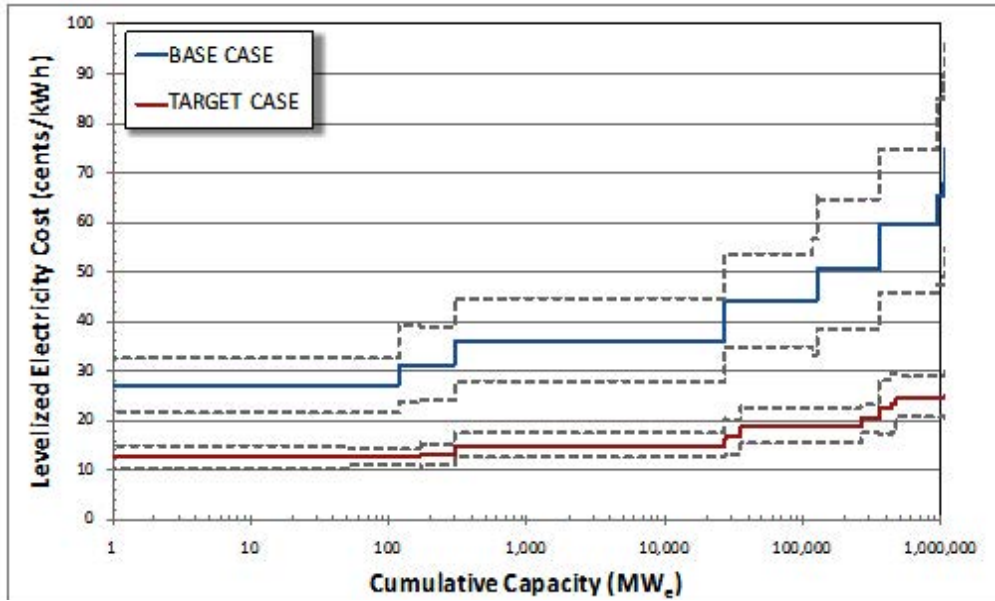
Figure 3-2: Estimated supply curve for electricity from deep EGS in 2008 U.S.$, plotted on a semi-log scale of LCOE vs cumulative capacity (Augustine, et al., 2010; Augustine, 2011) [16, 4]. The base case assumes current technology and the target case assumes enhanced technologies, in particular with production flow rates and EGS reservoir lifetimes increased from 30 to 60 l/s and from about 5 to 30 years, respectively.

Many factors impact the ability to bring high temperature fluids to the surface at sufficient flow rates to deliver useful power generation, so advancing EGS development will require balancing the relative benefits of different technology investments. Cost-benefit scaling can help with establishing priorities. Here we provide an example based on one of the key cost drivers in EGS, which is drilling.

The economic value of the energy stored in oil and gas has driven development of sophisticated drilling capabilities. While this investment in technical development is available for application to geothermal wells, the actual cost of using drilling technology remains a serious consideration for the rates of energy delivery expected for EGS: the costs of drilling geothermal wells are an appreciable factor in the cost of delivering geothermal power, as summarized in Figure 3-3 (see also Augustine, 2011) [4].
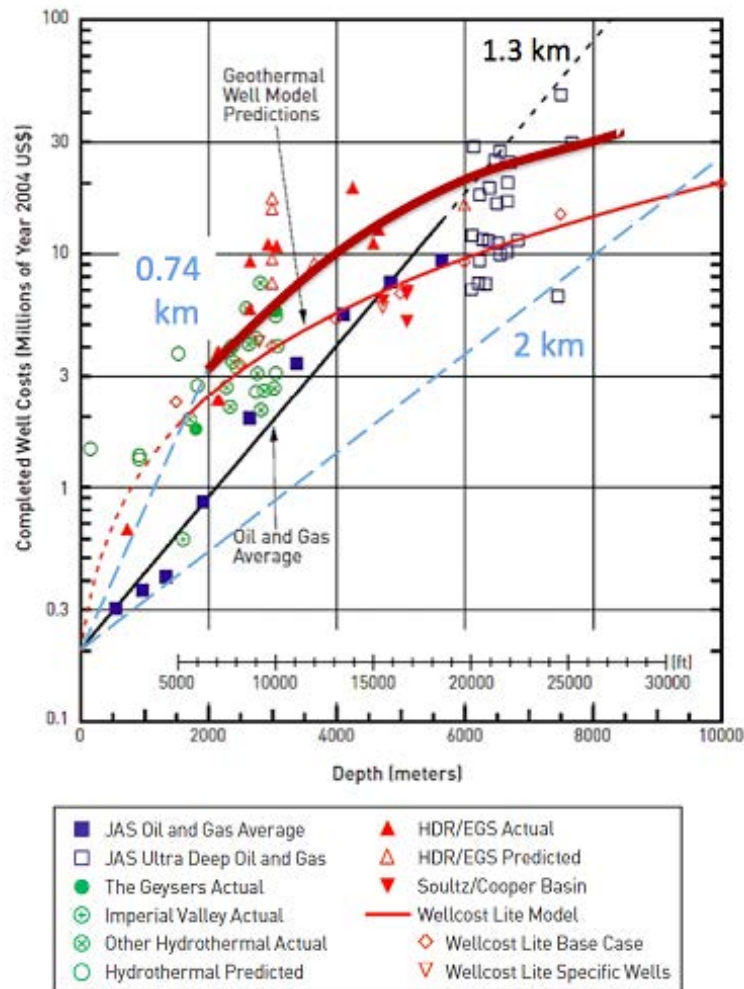
Figure 3-3: Cost (in 2004 U.S.$) as a function of depth of drilling onshore wells, with reference slopes indicated for *e*–folding distances of $d = 0.74$, 1.3 and 2 km (*dashed-blue lines* and *solid- and dashed-black line*, the latter summarizing costs for oil and gas wells); the *solid- and dashed-red curve* is from the Wellcost Lite model (adapted from Tester, et al., 2006) [7]. The *heavy brown curve* shows the GEOPHIRES model of Beckers, et al. (2013) [17], with cost in 2009 U.S.$. The most abundant data are represented by the JAS Oil and Gas Average (*filled blue points*).

A simple cost-benefit analysis compares the benefits against the costs of extracting heat as a function of depth (z). Assuming the temperature gradient with depth (dT/dz) is constant, which is true for the top of Earth's crust where heat is lost primarily by conduction, the specific heat content (J/kg) increases linearly with depth

$$Q \approx C_P \frac{dT}{dz} \delta z \approx 36\delta z(\text{km}) \text{ kJ/kg} \tag{3-2}$$

using values in Table 3.1. In geothermal mining, the temperature is reduced by a given amount of order $-\delta T \approx 10 - 100$ K for the lifetime of a geothermal well (e.g., Tester, et al., 2006) [7]. Therefore, the extractable heat increases linearly with depth, at a rate

$$\delta Q \approx C_P \delta T \approx 12 - 120 \text{ kJ/kg} \tag{3-3}$$

(i.e., per kg of rock accessed with increasing depth). The actual heat extracted has to be multiplied by a recovery factor of order 2 percent [1, 22].

We model this extractable heat as a benefit B that increases linearly with depth

$$B = a + b z = b(z - z_0) \tag{3-4}$$

where $z_0 = -a/b$ is the minimum depth from which heat is extracted. Shallower levels may be inaccessible due to environmental concerns, or may simply be overburden that is too cold to mine; z_0 can be zero in a region of natural geothermal activity.

The cost C of drilling is approximately exponential with depth (Figure 3-3),

$$C = c \exp(z/d) \tag{3-5}$$

[7]. Combining 3-4 and 3-5 gives the ratio of benefit to cost

$$B/C = (b/c)(z - z_0) \exp(-z/d), \tag{3-6}$$

which has a maximum at $z_{\max} = d + z_0$ independent of the parameters b and c that determine the conversion of heat or drilling cost to depth (Figure 3-4). Thus, the maximum in the ratio B/C is set by the cost curve for drilling.

17

Table 3.1: Properties of Earth's Continental Crust Relevant to EGS[1]

Density (ρ)	2.5×10^3 kg/m^3	typical for granite
Thermal diffusivity (k)	≈ 1 mm$^2/s = 10^{-6}$ m^2/s	
Mean atomic weight	≈ 0.021 kg/mole of atoms	
Heat capacity (C$_p$)[2]	1.2 kJ/K/kg	ρ C$_p = 3.0$ MJ/K/m^3
Thermal conductivity (k)	$\kappa \rho$ C$_p = 3$ W/m/K	
Radioactive heat production (H)	$\approx 3 \mu$W/m^3	
Instantaneous temperature change due to radioactive decay[3]	$\approx 10^{-12}$ K/s	
Large-scale tectonic movements, uplift, erosion	$\approx 1 - 10$ cm/yr horizontal $\approx 0.1 - 1$ mm/yr vertical	
Compressibility	$3.3 - 6.9 \times 10^{-10}$ Pa^{-1}	
Thermal expansion coefficient (α)	2.4×10^{-5} K $^{-1}$	
Heat transfer coefficient (h)	0.8-8 kW/m^2.K	With water; ref. Robertson [18], p. 92
Temperature gradient	25 K/km – 40 K/km	
Geothermal heat flux	80-120 mW/m^2	Average to high values over the Earth; thermal energy transferred by this mechanism over the continental U.S. = 500 GW (9.8×10^6 km^2)

[1] Properties derived from Ahrens (1995) and Clauser (2011a,b) [19, 20, 21].

[2] Typical value at high temperatures, with actual values being lower by 20-50% at temperatures of 20-400° C ($\sim$ 300-700 K).

[3] Heat production due to Earth's natural radioactivity decreases exponentially over time with a half-life of order 10^9 yr (e.g., Turcotte and Schubert, 1982) [9]. Current radioactive heat production is therefore about half its value 3×10^9 yr ago; for our purposes, we treat the heating rate due to radioactive decay as being constant.

Typical values of d lie in the range 1.3-2.1 km, though field data indicate values as small as $d = 0.74$ km for depths of $z = 0$-2 km and as large as 2.1-2.6 for depths approaching 8 km (0.74 km corresponds to the near-surface trend of the Wellcost Lite model: Tester, et al., 2006 [7]). The GEOPHIRES model uses a power law, $C = 1.1\ z^{1.6}$ with cost in \$M and depth in km (Beckers, et al., 2013) [17], implying an e-folding length-scale $d = (d \ln C/dz)^{-1} = z/1.6 = 0.6$ to 3.1 km for $z = 1$-5 km. Therefore, z_{max}=1.8 ($\pm$ 1.2) km + z_0, meaning that peak values of benefit/cost are well within the range accessible to current drilling technologies.
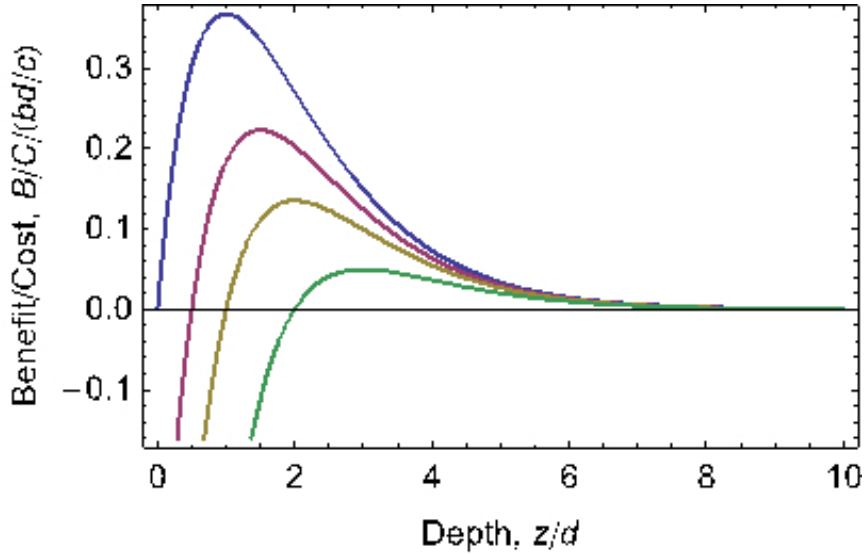
Figure 3-4: Normalized Benefit/Cost ratio (B/C)/(bd/c) as a function of normalized depth z/d for overburden depths $z_0/d = 0$ (blue), 0.5 (purple), 1 (olive) and 2 (green), according to (3.6). In each case, the maximum value is at $z_{\max} = d + z_0$ and B/C is negative for depths less than z_0.

This simple analysis shows that with an exponential increase in drilling cost with depth, the cost/benefit ratio decreases below about 2-4 km depth (assuming $z_0 = 1$ km). With better understanding of the factors governing the depth dependence of the benefits and costs of EGS, analyses going beyond this toy model can be refined to assess the practicality of different development approaches and identify decision points for the research program.

3.3 Overview

Recent supply curves show the potential for geothermal energy to contribute 5-18 GW_e within the current cost range of about \$40-80/MWh (4-8 cents/kWh) which is comparable to the cost of other available energy resources (compare Figure 2-1 and Figure 3-5). In particular, development of geothermal technology mainly increases the potential for near-hydrothermal field EGS to contribute in the near term, as compared to the longer term implied by higher costs (cf. target vs. base cases). A conservative estimate is

therefore that an additional 5-10 GW_e of geothermal power can be expected in the near future, say 5-10 years, including through the development and application of EGS technologies (however, not entirely dependent on such advances).

We may be overly cautious in this assessment, but note that the NREL study on which these cost estimates rely assumes a drilling cost 30 percent down from the 2008 value (as quantified by the Bureau of Labor Statistics Producer Price Index, PPI). In fact, the price of drilling has instead continued to rise in recent years, and is now 15 percent above the 2008 PPI. Given the importance of drilling costs on practical development of geothermal energy (Augustine, et al., 2010; Augustine, 2011) [16, 4], this difference between model and current reality suggests the need for caution (see also p. 31 of DOE 2011) [23].
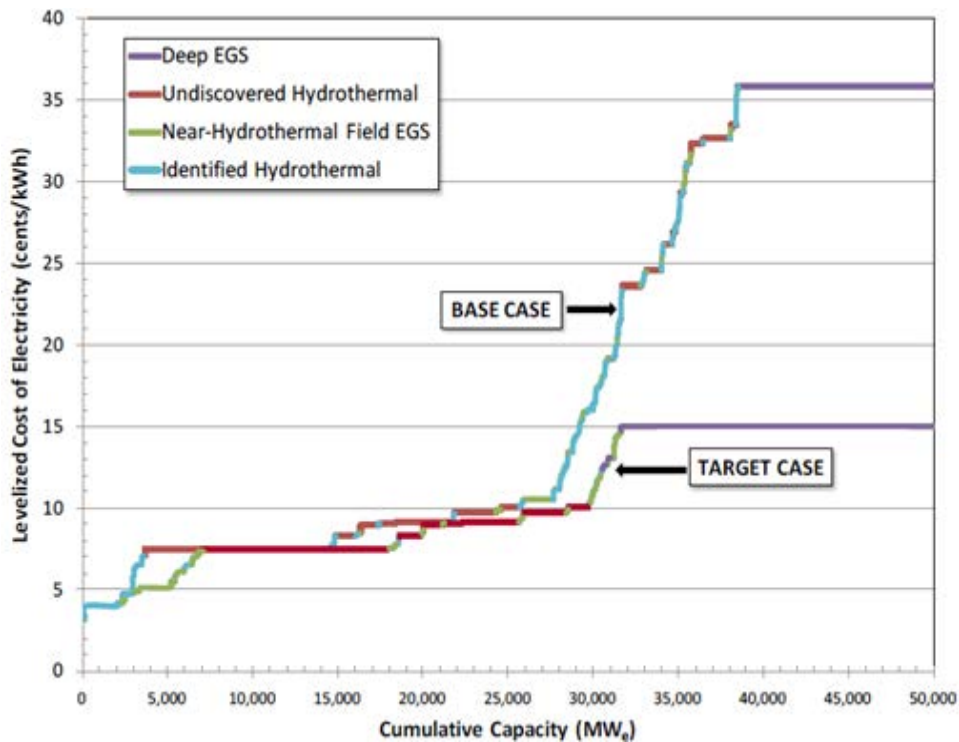
Figure 3-5: Supply curves for geothermal technologies according to NREL models, with base and target cases described in Figure 3-2 (Augustine, 2011). We consider both near-hydrothermal field EGS and deep EGS to be part of EGS in the present report.

In summary, we see evidence for U.S. geothermal power production realistically increasing two- to four-fold from its current contribution of 2.5 GW_e, with EGS technologies playing an important role in realizing this advancement in the near term, the coming 5-10 years (see also Harto, et al., 2013) [24]. This in itself would be a notable success, opening the door to the far greater potential of geothermal energy as EGS technology is more broadly developed and deployed. In particular, current extrapolations suggest another two- to five-fold increase in capacity toward the 100 GW_e potential mid-term (beyond $\sim$ 10 years) potential identified at present (Figure 3-5).

Our review of technology opportunities below supports a strategy of emphasizing expansion of hydrothermal capabilities in the use of EGS (e.g., near-hydrothermal field EGS) as a prudent means of nurturing the science and engineering that can lead to technical breakthroughs, in line with current DOE planning (e.g., DOE 2011) [23].

4   IMAGING AND CHARACTERIZATION

DOE has broad interests in characterizing the subsurface, and is therefore engaged with a variety of technologies for imaging and monitoring regions within Earth's crust (e.g., Snieder, et al., 2007) [25]. The needs of EGS are sufficiently distinct, however, that it is worth identifying promising opportunities for characterizing 1) regions being considered for future stimulation and production; 2) the spatial extent and characteristics of a stimulated volume; and 3) the spatial-temporal evolution of the region from which heat is being extracted.

Stimulation by hydrofracturing, for example, is expected to create vertical fractures because the principal normal stress is vertical at the depths being contemplated for EGS. Therefore, reflection seismology that is so heavily used in oil and gas exploration (because it typically gives the highest resolution over the greatest distances) needs to be performed at depth, in order to have near-normal incidence relative to the vertical fractures. This is in contrast to the (roughly) horizontal layering of oil and gas fields that allows data collection from Earth's (horizontal) surface for hydrocarbon exploration.

There is a tradeoff between range and resolution of features that can be imaged in the subsurface, with Figure 4-1 showing typical values for high-frequency seismic (kHz-MHz) and electromagnetic (MHz-GHz) methods. In detail, the values depend on material properties such as seismic-wave velocities and dielectric constant, the latter being especially sensitivity to the presence of moisture (a key factor in use of ground-penetrating radar, GPR). Nevertheless, resolution of meters or less generally requires imaging at distances less than tens to hundreds of meters, which implies getting sources and sensors near the region of interest.

This requirement of close-in imaging may be relaxed by turning to non-linear methods, which will be described in a subsequent section. We first describe an interferometric approach that can facilitate elastic imaging at depth.

4.1   Ambient-Field Seismic Imaging
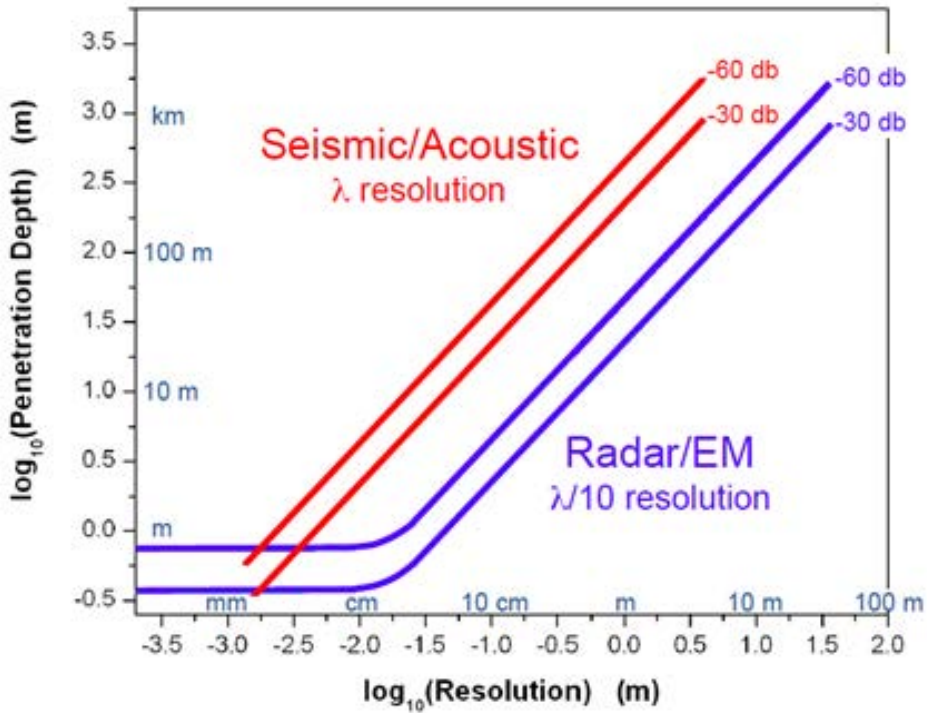
Figure 4-1: Calculated distances (penetration depth or range) over which high-frequency seismic (acoustic) and electromagnetic (Radar/EM) wave-based imaging can achieve a given resolution for return signals 3-6 orders of magnitude smaller than transmitted (-30 and -60 db). We assume linear elasticity and absorption (compressional-wave velocity and quality factor v_p = 5 km/s and Q = 100 at seismic frequencies of 100-1500 kHz; attenuation increasing from 2 to 20 m^{-1} at 15-1400 MHz and corresponding variations in dielectric constant for EM), with assumed resolution criteria (λ and $\lambda/10$, with λ being wavelength) that depend on processing methods used. The plot, applicable to high-resolution seismic reflection and ground-penetrating radar (GPR) measurements, implies resolution of 1 m at distances of order 10^2 and 10^1 m, respectively.

The only means of achieving near-normal incidence for vertical fractures at depth is to emplace sources and sensors in the subsurface. This is possible through conventional drilling, and may in the future be significantly enhanced by micro-drilling approaches we describe below.

A major development in seismology is to dispense with sources – which in this case would also need to be deployed at depth (and in different locations from the sensors) – through the use of interferometry. In particular, the ambient seismic field (background seismic noise) present in the crust can be used as a form of seismic "daylight" that illuminates the subsurface (Snieder and Wapenaar, 2010; Snieder and Larose, 2010) [26, 27].

The basic idea is to cross-correlate the signals from distinct detectors, effectively turning one sensor into a virtual source with respect to the other detector(s). With an array, which could simply be a string of detectors down a borehole, one has enough detector-pair combinations to be able to reconstruct images akin to those of reflection seismology, and so make possible imaging of vertical structures in the subsurface.

Ambient-field reflection seismology has been demonstrated from the surface (Figure 4-2) (Draganov, et al., 2007, 2009) [28, 29], with an application to imaging a geothermal field summarized by Tibuleac and Eneva (2011) [30], for example. In principle, one ought to be able to similarly image vertical structures in the subsurface through ambient-field seismic-reflection imaging in boreholes. In fact, the concept has been demonstrated through imaging of the San Andreas Fault from the side, in this case with nearby drilling serving as the source of seismic energy (Figure 4-3).

Snieder and Wapenaar (2010) [26] point out that shear-wave polarization can be used to determine fracture orientations at depth, and that cross-correlation of ambient seismic and electromagnetic fields can additionally provide a basis for characterizing subsurface permeability and fluid flow through poro-elastic effects. deRidder and Biondi (2013) [32] offer a recent
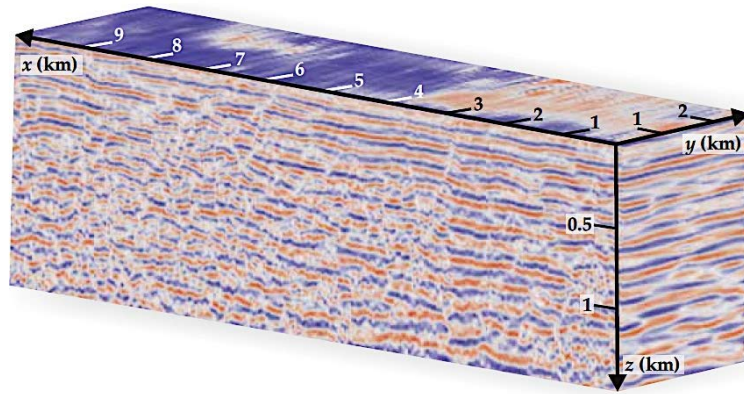
Figure 4-2: Three dimensional reflection image of crustal structure beneath the Libyan desert based on data obtained by cross-correlating 11 hours of ambient noise measured at the surface, illuminating horizontal discontinuities in seismic velocities (rock layers) at depth (Snieder and Wapenaar, 2010, based on results of Draganov, et al., 2009) [26, 29].
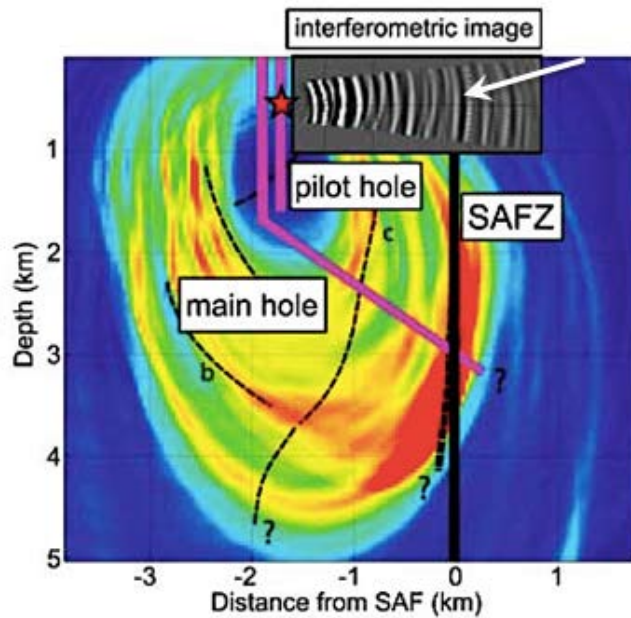
Figure 4-3: Interferometric image of the San Andreas Fault Zone (SAFZ) (*inset*) near Parkfield, CA, produced by recording in the pilot hole (*right magenta line*) drilling noise from the main hole (*left magenta line*), shows multiple reflections, including one due to the main SAF fault (*white arrow*). The target receiver used for imaging is indicated (*red star*), and the background color image (with thin dashed lines, question marks, and "b" and "c" labels) is from independent seismic imaging (colors indicate seismic-velocity variations) [31].

26

example of monitoring daily changes in an oil field at several hundred meters depth through ambient seismic noise.

4.2 Nonlinear Elastic Response

Nonlinear elasticity potentially offers unique benefits for subsurface imaging relevant to EGS. First, the nonlinear response of rock – deviations of observed strain from being directly proportional to the stress applied to a volume of rock – is highly sensitive to the presence of fractures under low effective stress (i.e., when fluid pressure inside the fractures closely matches the normal stresses due to overburden). The condition of low effective stress is of interest for i) identifying subsurface regions susceptible to stimulation for EGS; ii) quantifying the degree (success) and spatial extent of stimulation; and iii) monitoring the temporal evolution of a stimulated zone at depth.

Second, it is not individual fractures but the zone that is (incipiently) fractured that is imaged: that is, dimensions of meters to perhaps hundreds of meters instead of crack widths of millimeters to meters. Therefore, the need for spatial resolution is far less demanding than required for the usual linear-elastic imaging of structures (Figure 4-1).

The basic idea is that fractures can be opened and closed by externally imposed stresses, assuming a condition of low effective stress. The elastic response of a fractured volume differs greatly (non-linearly), depending on whether the cracks are in the process of opening up or are clamped shut (e.g., shear waves with polarization in the plane of the cracks being scattered or not, respectively). Therefore, regions of a rock insonified with a mix of, say, low-frequency waves (that open and close fractures, where present) and high-frequency pulses (that scatter off opening cracks) can in principle be used to reveal the presence of fractured zones (Figure 4-4).

Imaging depends on matching the timing, at each location in the rock volume, between high-frequency (probe) waves being present at a fracture

27

when the low-frequency (forcing) wave has the appropriate phase to open the crack rather than clamping it shut. In practice, the presence of cracks produces scattered waves at the sum and/or difference frequencies of the forcing and pulse frequencies, and localization is obtained by means of travel-time measurements to a detector array.
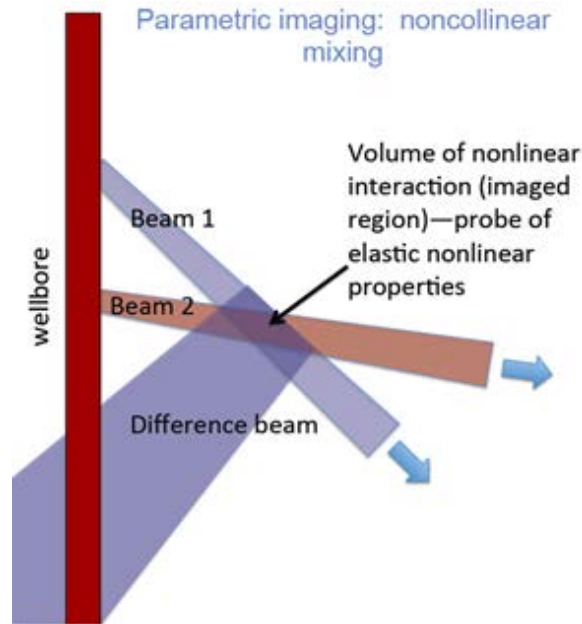
Figure 4-4: Schematic of nonlinear elastic imaging as applied to the subsurface, using arrays of transducers in a borehole to send two beams (low-frequency forcing beam plus high-frequency probe beam) in order to insonify and image a region of interest, as revealed by the difference (and/or sum) beam that emerges from the volume of nonlinear interaction (courtesy of P. A. Johnson).

Nonlinear elasticity of rock has been studied in the laboratory for more than 25 years, and shown to provide highly sensitive information about the presence, nature and spatial distribution of fractures, grain boundaries and other structural defects (e.g., Johnson, et al., 1987 [33]; Johnson and Shankland, 1989 [34]; Guyer and Johnson, 1999 [35]; Pasqualini, et al., 2007 [36]). One implementation that might be applied to the subsurface is documented by Kazakov, et al. (2002) [37], who showed that a crack insonified by a low-frequency wave is effective in scattering a high-frequency probe beam so as to produce an image of the crack (Figure 4-5); not surprisingly, the
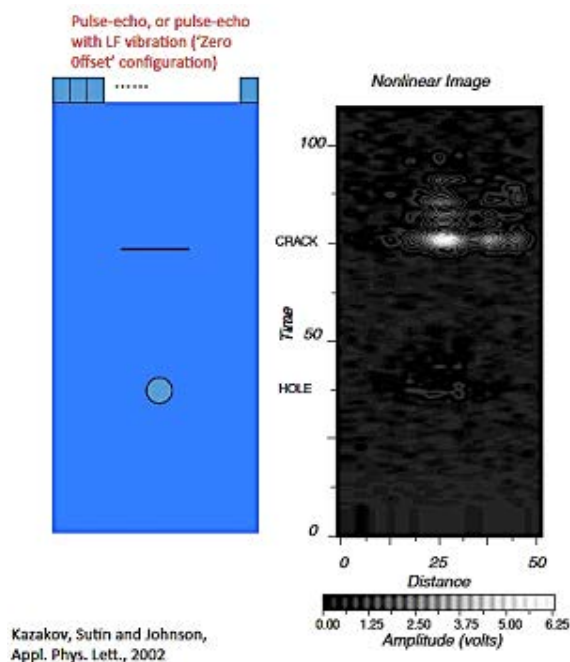
Figure 4-5: Laboratory demonstration of nonlinear elastic imaging of a crack in a steel plate that also contains a hole (after Kazakov, et al., 2002 [37]). The nonlinear image (*right*) shows the presence of the crack, as illustrated in the schematic (*left*). Because of its thin dimension, the crack is barely visible in a linear-elastic image (not shown).

crack was nearly impossible to resolve by standard (linear-elastic) methods. If scaled up from laboratory to field distances, nonlinear elasticity could offer an important advance in subsurface imaging relevant to EGS.

Time-reversal imaging of nonlinear elastic response is established as a means of non-destructive evaluation of materials at the laboratory scale (e.g., Ulrich, et al., 2008) [38]. What now needs to be done for application to EGS is to validate this method at field scales of tens to hundreds of meters in order to determine the practical ranges and sensitivities of the method. For example, over what distances can cracks be sufficiently insonified to produce a nonlinear elastic response, and is background (elastic) heterogeneity of the rock small enough to allow nonlinear imaging at ranges of interest? Initial field experiments do not need to be performed at great depth (e.g, meters to tens of meters would be sufficient, rather than the km depths of EGS),

and would mainly be used to document tradeoffs between range, resolution and sensitivity that can be achieved. The potentially confounding effects of background clutter are unlikely to be important at distances of meters (i.e., not much larger ranges than achieved in the laboratory), so there is much information to be gained as one scales up to distances of tens and then hundreds of meters. Subsequent work could take the field experiments to greater depths.

In addition to characterizing the quality of signal that can be acquired, there will be practical considerations of equipment and configurations to be used. For example, low-frequency insonification might best be driven from the surface, using Vibroseis or related technologies, rather than via down-hole transducers (Figure 4-4). Optimal frequency ranges will also have to be determined.

In this regard, seismic energy is not the only means of applying a forcing stress (or strain) to a volume of subsurface rock. Changes in temperature cause thermal strains, and these have again been shown to produce nonlinear changes in elastic properties that can be used to image damage zones – at least at laboratory scales (e.g., Ohara, et al., 2013) [39]. Another form of low-frequency forcing comes from natural tides that stress Earth's crust with a well-known spectrum of periodicities and may therefore be able to reveal modified properties of freshly stimulated regions at depth. It is further conceivable that seismic daylight, as described above (ambient seismic field), could be used to image the resulting nonlinear elastic response.

In summary, there are opportunities for developing nonlinear elastic imaging to document thermal and other time-dependent changes of rock that are relevant to EGS characterization at depth in the crust.

4.3 Drilling

Drilling plays many roles for EGS, from exploration and characterization of likely sites to development and production of a field [40]. Because drilling is so important to characterization of the subsurface, whether by directly sampling the rock at depth or by providing access for other instrumentation (e.g., seismic and electromagnetic sensors described above, as well as tracer experiments discussed below), we discuss drilling technologies next. However, this text applies just as well to EGS creation and production, as discussed in a later section. We recognize that explosives can be used to complement drilling for EGS, and encourage consideration of this technology, as well.

Many of the challenges that arise with drilling for EGS are the same as arise in drilling for hydrocarbons (see Maurer, 1980) [41]. EGS thus can take advantage of technologies developed for the much larger hydrocarbon industry.

4.3.1 Conventional holes

Drilling is based on applying shear stress by friction with a hard bit pressed against rock, leading to tensile and shear failure behind and around the sliding contact. This is particularly important for hard rock because the shear strength is significantly less than the uniaxial compressive strength (e.g., 200 MPa versus 5 MPa for granites). Drilling for conventional geothermal has been among the most challenging drilling activities because the rock is hard and the holes must be large. Polycrystalline diamond compact (PDC) bits now widely used in other applications (oil and gas) were originally developed 30 years ago for geothermal drilling. There have been modest improvements in the relevant conventional drilling technology with PDC, and they are becoming more widely used than conventional roller cone bits. Schlumberger reports a 1/3 increase in average run lengths for its newest bits for high-temperature hard rock drilling (Schlumberger, 2012) [42].

Some new materials have been developed. Further improvements in PDC have been reported by SNL, drilling a 3000 ft geothermal well at an average rate of 30 ft/hr over four days, three times better than standard roller cone bits (Sandia, 2012) [43]. These compacts have been improved by the use of microwave sintering (e.g., tungsten carbide to diamond composites). Other materials potentially useful for hard rock include nanopolycrystalline diamond (Nakamoto et al., 2011) [44] and tough CVD diamond (Liang et al., 2009) [45], which have been proposed for deep drilling. Though tougher than polycrystalline diamond, wear resistance tests in the field have not been done.

4.3.2 "Microholes"

Developing technology for rapid drilling of small holes is of interest to both the hydrocarbon industry and EGS for exploration and seismic sensing (noise levels are much lower even at a few hundred feet of depth than at the surface, and EGS requires monitoring microseisms that indicate fracturing). Conventional deep big holes start at >20" diameter and taper down with progressively smaller casing reaching 6-7" at depth. Microholes are defined as those less than 5", typically 2-2.5" which would give a 1" ID hole with casing. In comparison to the larger holes, the casing can be light, there is significantly less hole waste and rock damage, and they can be drilled quickly to minimize cost and to allow more extensive and accurate monitoring. Real and perceived potential hazards from induced seismicity, as well as its use as a mapping tool provides additional impetus for developing better monitoring of EGS systems. Tomographic monitoring is accomplished from a distribution of holes containing an array of geophones. Another driver for small holes has been gas control for coal mine safety (Lu et al., 2013) [46].

As described by Majer (2013) [47], the target is for boreholes that (a) can be drilled at 100 to 200 ft/hr to minimize cost, (b) extend to depths of at least 5000 ft at these high drilling rates; (c) have minimum waste, which maximizes speed while minimizing permitting issues; (d) have small

rig footprint, for rapid deployment as well as minimizing permitting issues; (e) have minimum formation damage to borehole walls and surrounding rock to improve monitoring; (f) have a small diameter that allows better seismic coupling of instrumentation to the rock.

For many technologies, drilling in homogeneous hard rock is straightforward. Encountering zones in which pressure is lost by washout, fractures, faults, and boundaries between rock types creates difficulties. Then balance must be struck between drilling pressure (air, water or mud) and the formation pressures/fluids (rock and fluid). Small holes would require an order of magnitude less material than conventional holes, a significant saving.

A program to develop both the drilling and the sensor technology was started by the DOE in 2005 but ended within a couple of years (Long, 2005; 2007) [48, 49]. It led to developments that included technologies for drilling small holes such as resonant drilling, high pressure fluid enhanced cutting, and high-speed drilling. Laser drilling and microwave drilling were also considered but remained far from proven in the field. The program also showed that small holes can accommodate small geophones and other tools (Long, 2007) [49], such as 3 mm Fabry-Perot MEMS accelerometers for seismic imaging (Lumedyne). Mapping with accelerometers/tilt meters was begun (Pinnacle Technologies), with tests carried out at the NSF-funded San Andreas Fault Observatory at Depth (SAFOD).

Reaching >5000 ft with microholes would provide the opportunity for arrays for 'horizontal' imaging as discussed in Sections 4.1-4.2. The lower noise and better coupling of instruments in shallower microholes may enable more extensive vertical seismic profiling up to four times the hole depth (Majer 2013) [47]. Vertical seismic arrays permit both active and passive seismic monitoring. Active monitoring examines fine scale structural features, including the locations of fractures/faults. Passive monitoring provides information on the dynamics of the fracture creation and induced seismicity resulting from changing stress.

Equipment that may be used in microdrilling is shown in Figure 4-6. The equipment for coiled tubing drilling (CTD), a method of drilling narrow diameter holes in which a drill bit driven by a motor in a bottom hole assembly (BHA), is contained within a lining of flexible narrow-diameter tubing that is unrolled from a coil. Unlike conventional drilling, there is no rotating drill string extending from the surface and no need to withdraw and relower it many times to add additional pipe. CTD is not a new technology, but has chiefly been used in well completion and re-entry, rather than as the principal means of drilling a new hole. However, it may become the optimal means of drilling narrow holes for emplacing sensors at depth or *in situ* measurement of rock properties.

Figure 4-6: Coil tubing rig capable of 1500 foot hole developed by LANL.

4.3.3   Resonant drilling

In rotary drilling, fluid is required to move the drilled material out of the way of the bit. Flushing media for sonic drilling can be as simple as

air and water. A sonic drill bit oscillates vertically, thus creating turbulent flow at the drilling interface that pushes loose drilled material aside. When flushing media are required, the actual amount required is small compared to rotary drilling.

Sonic (termed resonant, because a drill pipe is oscillated at its lowest resonant frequency) drilling is being developed for comparatively shallow wells, generally in soft or unconsolidated material. It may be useful for drilling the shallow wells (to 500 ft) needed in larger numbers for emplacement of seismic sensors. Drilling rates have been reported to be several times faster than for conventional drilling. Whether or not it can be applicable to deeper drilling for EGS injection and production wells will require additional research and development. Critical factors include the need to balance the force of a long drill string to promote cutting without fusing of the tip with the rock, damping losses due to contact with the borehole walls, and changes in rock properties with depth (see Lucon, 2013) [50].

4.3.4   Fluid injection drilling

Abrasive jet cutting was proposed early on for drilling (see Kolle, 1999) [51]. H_2O or CO_2 can be used as the fluid. Use of a CO_2 slurry mix, nozzle and high-pressure slurry pump has been demonstrated in the lab to have high penetration rates in basalt. If a larger bore is required, rotation of the nozzle(s) can be provided with a small down hole hydraulic or electric motor. The pump accelerates and pressurizes the slurry. A nozzle can be focused to concentrate the slurry stream on the periphery of the drill hole, reducing the work required, as demonstrated in the 1960s (Maurer, 1980) [41]. Limited field studies have been conducted with small coiled tubing (for example with 1" OD tubing). The entire bottom hole assembly is inexpensive such that the coiled tubing can be cut and cemented in place when the desired depth is reached.

The original CO_2 technique grew out of the technology developed by LANL, and has been used for drilling to 1500 ft. High pressure (3000 – 5000 psi) is used to cut through the rock. There is near zero "weight on bottom hole", gravity guiding the drilling direction. LANL used this to drill 1.25" ID holes in which 48 levels of geophones (0.85" OD sensors) were mounted. A surface pumping system mixes the proper fluids and solids concentration and pressurizes such slurries. High pressure pump systems developed for these slurries operate at up to 15,000 psi and 15 gal/min.

Abrasive jet drilling has not succeeded in drilling deep holes because of the difficulty of handling and delivering the amounts of abrasives required at depth, the need to balance the high-pressure of the jet with the pressure of fluid in the hole, and difficulties in steering. Wear on the nozzles by the abrasive could be reduced with the use of toughened materials discussed above (e.g., diamond-based materials). Work continues on developing hybrid technologies that involve abrasive jets and impact drilling (e.g., Lu et al., 2013 [46]) but field tests in EGS-relevant environments apparently have not been reported.

4.3.5   High-speed dual string drilling

High-speed ($\sim$ 5000 rpm) grinding mechanisms (Figure 4-7) must put very little weight on the bit because the frictional power dissipated is proportional to the product of the rotation rate, the applied force and a coefficient of friction (Kolle, 1996) [52]. This method produces pulverized stone with sub-millimeter particles, in contrast to the large broken up rock typically produced from slow grinding (Able, 2013) [53]. The lower weight on the bit produces less wear. Both diamond impregnated bits and PDC have been used. The first high-speed dual string system will be tested in the field this year.
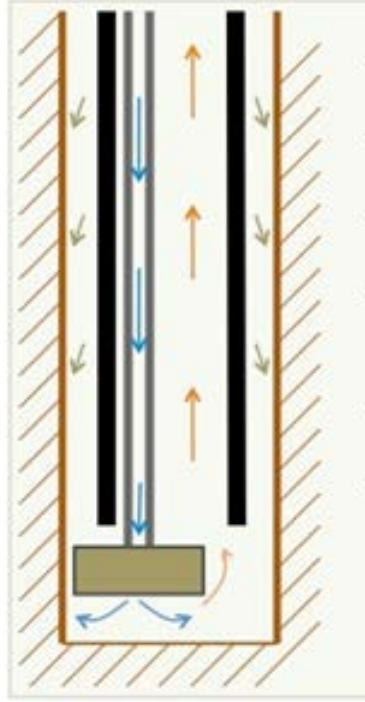
Figure 4-7: Schematic of a high-speed dual string drilling (Able, 2013) [53].

4.3.6 Summary

In summary, although we are not aware of any single breakthrough technology, developments that may lead to drilling small holes for exploration and monitoring warrant further study. These may take advantage of continued developments of small deployable sensors for downhole monitoring, including imaging. Overall, we conclude that microhole research and development begun during the past decade should be followed up with the appropriate field tests.

4.4 Physical Description and Time Evolution of an EGS Reservoir

It is useful to describe in order of magnitude terms the basic physical processes associated with fluid flow, heat transfer and tracer transport as all

are important for the response and characterization of the thermal system. First, we assume that hydraulic or other fracturing operations occur, which produce a crack-like network, that is combined with existing fractures and faults in the rock (Figure 4-8). Ideally, the fracture network extends from the injection well to the production well, but the spatial characteristics (e.g. typical dimensions and the heterogeneity) of the fracture network are a significant unknown. A major goal of subsurface imaging and characterization is to more accurately determine the spatial structure of the flow network. Because Earth is effectively an elastic medium, albeit with nonlinear and time-dependent, hysteretic (viscous) properties, the flow network, e.g. the typical crack openings, can evolve in response to time varying applied pressures.
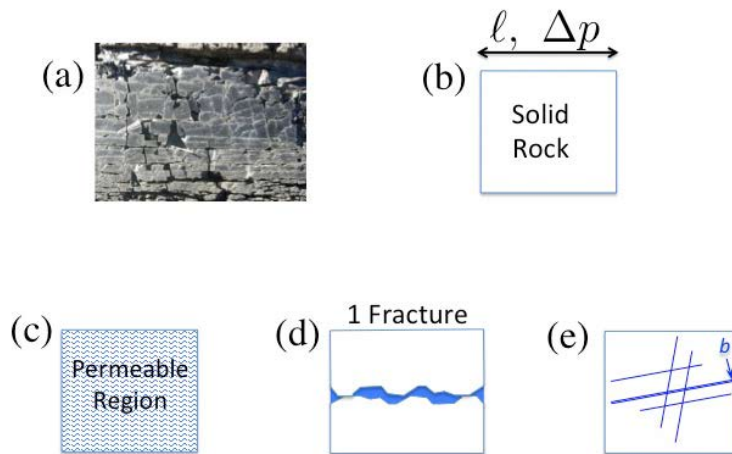
Figure 4-8: Models of a fracture network in a rock. (a) Image of a typical rock in the field setting (S. Petty briefing to JASON). (b) A pressure drop Δp is applied between injection and production wells a distance ℓ apart in order to extract energy from hot rock in the subsurface. (c) The subsurface may be modeled as uniformly permeable. (d) A single fracture produces a local region of high permeability in a region of otherwise low permeability. (e) A network of cracks: as discussed in the text, the flow rate is proportional to b^3 ("cube law"), so is dominated by the widest crack.

For now we simply assume that a fracture network exists. It is natural to expect that the network has a distribution of channel openings (b), which represent the smallest dimensions in the network, spans a distance $h \gg b$

perpendicular to the flow and is in the plane of the crack (for a simple uniform crack), and lengths $\mathcal{O}(\ell)$, where ℓ is the distance between the injection and production wells. We assume $b \ll h \lesssim \ell$ (see Figure 4-9).
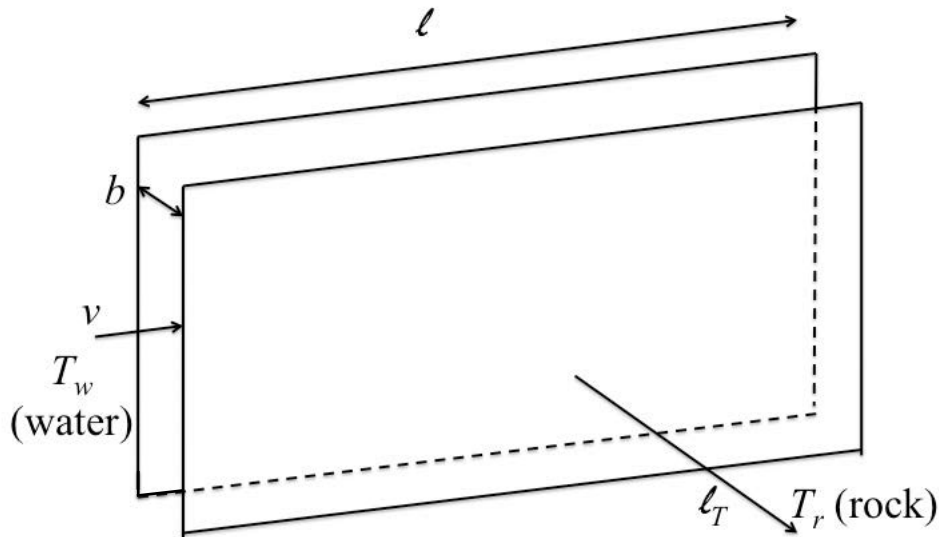
Figure 4-9: Schematic of the model geometry for flow in a crack of width b, with other common notation indicated.

4.4.1 Some characteristic scales of the crack network for flow and heat transfer

If a crack opening b is too large then fluid flows rapidly through it without being heated close to the rock temperature. Even if energy is extracted, the Carnot efficiency of water in an energy producing cycle is low. Also, if crack openings are too narrow, their low hydrodynamic admittance (or large viscous resistance) requires more hydrodynamic work and a higher pressure drop between injection and production wells in order to extract the desired power. Note that generation of geothermal energy is implicit in our assumption of a characteristic time scale of energy extraction, which, practically, is

determined by economic considerations of return on investment; we do not attempt any economic analyses here.

We first determine a characteristic width[1] b_0 of a crack in EGS, defined as the typical width of the cracks that draw heat approximately uniformly from the entire volume penetrated by cracks. We note that the actual crack widths in the reservoir need not be equal, or even comparable, to b_0 (though we later show they must not exceed b_0 for efficient generation of geothermal power); b_0 only defines a physical scale characterizing the coupled fluid flow and heat transfer. This characteristic width is a function of the parameters of the resource. We consider cracks of width b, length (between injection and production wells) ℓ, and transverse (spanwise) dimension h (that does not enter); typically we take $h = \ell$.

When making estimates below we will use the thermal diffusion coefficient $\kappa_r = 10^{-6}$ m^2/s ≈ 30 m^2/yr for rock, volumetric specific heats of rock $C_r = 2.5 \times 10^6$ J/m^{3}K and of water $C_w = 4.2 \times 10^6$ J/m^{3}K, pressure drop $\Delta p = 100$ bar, viscosity of water at a mean temperature of 100°C is $\eta = 3 \times 10^{-4}$ kg/m-s, and a crack length $\ell = 10^3$ m. Also, we will typically assume a system age $t_r = 10$ years.

To heat the water efficiently in a crack of width b we equate the thermal energy (per unit area) carried by the water as it is heated by an amount ΔT_w over a length ℓ

$$\frac{\Delta T_w C_w v b}{\ell}, \tag{4-1}$$

where v is the mean flow speed, to the conductive heat flux out of the rock,

$$\frac{2 k_r \Delta T_r}{\ell_T}, \tag{4-2}$$

where k_r is the thermal conductivity of rock, ΔT_r is the temperature drop between the deep hot rock and the water and thermal conduction sets the minimum length scale, $\ell_T = \sqrt{\kappa_r t_r} \approx 18$ m, of temperature gradients in the rock assuming a 10 year time scale. The factor of 2 accounts for the two

---

[1]By "width" of a crack we mean the distance separating its two, nearly planar, surfaces, which is generally quite small compared to other length scales in the system.

surfaces of a planar crack. Cracks spaced closer than $\mathcal{O}(2\ell_T)$ effectively draw on the same thermal resource, although their hydrodynamic admittances add, reducing the pressure drop and mechanical work required to extract the same amount of heat.

For efficient operation of such a geothermal system we desire $\Delta T_r \ll \Delta T_w$, which is equivalent to requiring that the water be heated to a temperature close to the rock temperature far from the cooling flow. For viscous flow in a duct, the mean speed is

$$v = \frac{\Delta p}{\ell} \frac{b^2}{12\eta}. \tag{4-3}$$

This law is generally written in terms of the two-dimensional flow rate $q = vb$, in which case $q \propto b^3 \Delta p$, which is sometimes known as the b^3 law. The use of this simple channel flow formula for cracked materials relevant to the solid Earth has been verified (Witherspoon, 1980) [54]. One simple consequence of the b^3 law is that for any system characterized by cracks in parallel the flow predominantly goes through the widest paths of lowest fluid resistance, which is the simplest form of bypassing the hot rock. Not surprisingly, such channeling has been suggested as one reason for low heat recovery factors (e.g. [1, 22]).

Combining equations (4-1 to 4-3), we find

$$b < b_0 \equiv \left(\frac{C_r}{C_w} \sqrt{\frac{\kappa_r}{t_r}} \frac{24\ell^2\eta}{\Delta p} \right)^{1/3}. \tag{4-4}$$

Inserting the typical numbers above, $b_0 = 0.027$ cm and the corresponding $v_0 = 22$ cm/s. Water flowing in a wider crack has faster speeds for the same pressure drop and well spacing ℓ, is heated less and does not approach the distant rock temperature. Although it is capable of removing thermal energy effectively from the rock, the lower water temperature reduces the thermodynamic efficiency of electric power generation.

The characteristic Reynolds number for such a typical crack is

$$\mathrm{Re}_0 = \frac{3\rho v_0 b_0}{4\eta} = \frac{\rho b_0^3 \Delta p}{16\eta^2 \ell} \approx 160, \tag{4-5}$$

41

where the factor of 3/4 comes from using the central (peak) velocity $3v_0/2$ and $b_0/2$ as the length scale, in analogy to the use of the radius to define the Reynolds number of a circular pipe flow. The flow in a crack thin enough for efficient heat transfer to the fluid is laminar, but if it is wide enough to be an efficient heat sink (turning the inequalities into approximate equalities) then it is likely that Re $\gg 1$.

If parametrized in terms of volumetric flow rate Q, taking the span of the crack to be $h \approx \ell$, the same as its length, the crack width drops out. The result is a condition on the flow rate Q in a single "characteristic" crack:

$$Q < Q_0 \equiv \frac{2C_r}{C_w}\sqrt{\frac{\kappa_r}{t_r}}\ell^2 \approx 60 \ \left(\frac{\ell}{1\,\text{km}}\right)^2 \text{l/s}, \tag{4-6}$$

where again we have made numerical estimates based on the typical parameters above. This value of Q_0 is comparable to the flow rates of entire EGS systems. If cracks have widths $b \approx b_0$ only one or a few may be contributing significantly to the fluid flow. A total flow rate $\lesssim Q_0$ implies that the temperature of the (initially) produced hot water is close to T_r, as observed. Were there only one contributing crack, it would be predicted that increasing the flow rate above Q_0 would immediately reduce the temperature of the produced water. Were there many contributing cracks, the temperature would not immediately be reduced, and the condition (4-4) for efficient use of thermal energy need not be violated. One conclusion from this kind of interpretation is that the dependence of produced water temperature on forced flow rate is a possible test for the number of significantly contributing cracks.

We return to discuss more about the thermal characteristics for heat transfer in the reservoir in our discussion of EGS energy production in Section 5.

4.5   Tracer Experiments and Models

It is important to use all possible tools to characterize the reservoir. Two kinds of tracers have been investigated, chemical tracers and thermal

tracers. The traditional means for studying transport processes in porous media are breakthrough studies where a tracer is injected at one well and extracted at another well; such studies are well described in the literature (e.g. [55, 56, 57]). These experiments are typically several days to a week in length and give at best an average characterization of a heterogenous medium, so it is important to consider faster methods as well as methods with more spatial resolution for characterizing the reservoir. Alternatively, injection for some time followed by withdrawal from the same injection well, so-called injection/withdrawal tests, are described also, but less frequently (e.g. [58, 59]).

Two characteristics that can possibly be estimated by tracer experiments are a measure of the permeability of the reservoir and some features of the local heat transfer from the reservoir to the water (these are obviously linked). Possible advances to achieve higher spatial resolution of the permeability variation may be feasible with electromagnetic monitoring of electrically conducting fluids likely in combination with injection/withdrawal tests (see Section 4.6).

4.5.1 Breakthrough curves from tracer studies

It is useful to first analyze the traditional characterization study where a tracer is injected at one location (the injection well) and the time history of a concentration profile is then measured at the production well. There is a large classic literature on this topic, including detailed studies on the broad topic of transport in porous media (e.g., [60]), and here we summarize the simplest one-dimensional model, which may give some insight into transport in systems. For simplicity we consider a one-dimensional situation where the average concentration $c(x,t)$ evolves according to (think of this as the average concentration over the dominant flow paths from injection to production wells)

$$\frac{\partial c}{\partial t} + v\frac{\partial c}{\partial x} = \mathcal{D}\frac{\partial^2 c}{\partial x^2} \tag{4-7}$$

where v is the average speed in the channel (here v is assumed constant) and $\mathcal{D}$ is the longitudinal dispersion coefficient, which here is assumed constant. In the spirit of the single-channel analysis summarized in Section 4.4.1 we note that for the conditions typical of laminar flows in a single long narrow channel the dispersion coefficient is given by the Taylor-Aris result [61]:

$$\mathcal{D} = D_m + \frac{1}{210}\frac{v^2 b^2}{D_m} \quad \text{or} \quad \mathcal{D} = D_m\left(1 + \frac{1}{210}\mathcal{P}_b^2\right), \tag{4-8}$$

where D_m is the molecular diffusion coefficient and the Peclet number is $\mathcal{P}_b = \frac{vb}{D_m}$. When $\mathcal{P}_b \gg 10$, the longitudinal dispersion is dominated by the flow with $\mathcal{D} \propto v^2 b^2/D_m \gg D_m$. This one-dimensional interpretation based on a single uniform channel is obviously an idealization and does not rationalize field data we describe below. Instead, the dispersion coefficient $\mathcal{D}$ in equation (4-7) should be interpreted as an empirical parameter characterizing the flow in the crack network.

Consider the case where an injection of a tracer is localized in space at some time $t = 0$, i.e. a delta function release of a fixed amount, $A = \int_{-\infty}^{\infty} c(x,t)\ \mathrm{d}x$, with $c(x,0) = A\delta(x)$. Then the classical solution to the convective-diffusion equation is

$$c(x,t) = \frac{A}{\sqrt{4\pi\mathcal{D}t}}e^{-(x-vt)^2/(4\mathcal{D}t)}. \tag{4-9}$$

One way this result can be used is to record a measurement at the production well, a distance ℓ away. Then the recorded signal, or breakthrough curve, is a function of time given by

$$c(\ell,t) = \frac{A}{\sqrt{4\pi\mathcal{D}t}}e^{-(\ell-vt)^2/(4\mathcal{D}t)}. \tag{4-10}$$

It is convenient to rewrite this equation in dimensionless form as

$$\frac{c(\ell,t)}{A/\left(\ell\sqrt{4\pi}\right)} = \frac{\sqrt{\mathcal{P}_\ell}}{\sqrt{\tau}}e^{-\mathcal{P}_\ell(1-\tau)^2/(4\tau)} \equiv C(\tau), \tag{4-11}$$

where

$$\tau = \frac{tv}{\ell} \quad \text{and} \quad \mathcal{P}_\ell = \frac{v\ell}{\mathcal{D}}. \tag{4-12}$$
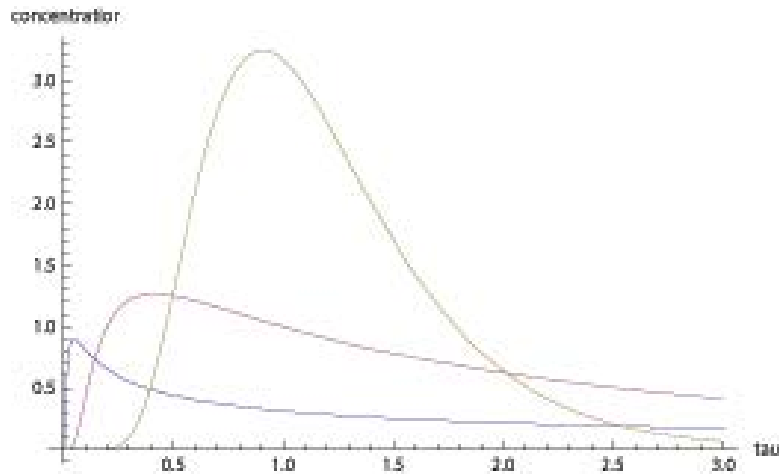
Figure 4-10: A plot of model breakthrough curves based on a one-dimensional convective-diffusion equation. Peclet numbers 0.1 (lowest magnitude), 1 (middle) and 10 (highest magnitude) are shown.

Typical theoretical breakthrough curves for different $\mathcal{P}_\ell$ are shown in Figure 4-10.

We have examined several breakthrough curves reported in the literature. For example, in Figure 4-11(a) we show the results of a typical field experiment from the Soda Lake geothermal site [62]; the red curve shows the results for a conserved, non-sorbing tracer. We note that the shape is qualitatively similar to the one-dimensional model. In addition, in Figure 4-11(b) we show data reported for breakthrough curves at the Steamboat geothermal reservoir and again the shape is qualitatively similar to the one-dimensional model. Next we investigate these results more quantitatively. Note that it is tempting to simply estimate the mean speed v by identifying the maximum in the breakthrough curve, which occurs at the time t_m, and then calculate the mean speed $v \approx \ell/t_m$. This estimate becomes increasingly inaccurate as the breakthrough curves show increasing degrees of longitudinal dispersion, as we quantify below. Next we take a closer look at this field data.

45
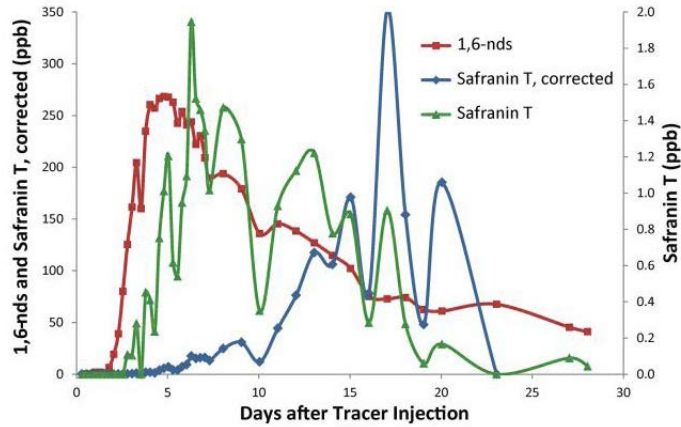
(a)
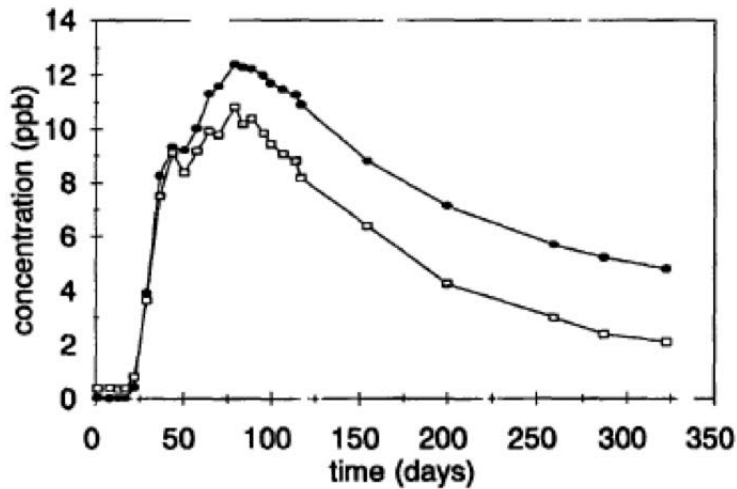
(b)

Figure 4-11: (a) Breakthough curves from field experiments at Soda Lake, Nevada [62]. The red curve is the response of a conserved, non-sorbing tracer, which is analyzed in the text. (b) Breakthrough curves from field experiments at the Steamboat geothermal site [63]. The upper curve is for a non-sorbing tracer, while the lower curve uses a chemical that degrades in time owing to thermal effects.

4.5.2 Order-of-magnitude estimates for the breakthrough curves

We can obtain some numerical estimates of the properties of an actual dry rock geothermal resource from a tracer experiment at Soda Lake [64, 62]. In this experiment the injection and production wells were 550 m apart and the pressure differential, provided by a 1360′ pressure head and an additional 110 psi on the injection well, was 48 bars, for a pressure gradient $\frac{\Delta p}{\ell} \approx 9 \times 10^3$ Pa/m [65].

A conservative (non-degrading, non-sorbing) tracer (1,6-naphthalene disulfonate according to [64]; 1,5-naphthalene disulfonate according to [62]) was injected. Injection continued over five hours [66], which is a short enough time that it may be considered instantaneous. The rate of fluid injection was 800 gpm (50 l/s), corresponding to a hydrodynamic admittance $A = 10$ l/s-bar $= 10$ l/s-MPa.

Tracer was first observed at the production well about 15 hours after injection, and its concentration rose to about $1/e$ of its maximum value about 50 hours after injection. Using this latter value to estimate the fluid velocity in a nominal crack, we find $v \approx 3 \times 10^{-3}$ m/sec (diffusion is expected to rapidly homogenize the tracer across the width of a crack). This value is much less than the characteristic v_0 defined in Section 4.4.1, and for the given pressure gradient, if this were a single crack, then $b = 0.0034\,\mathrm{cm} \ll b_0$. The corresponding Reynolds number Re ≈ 0.3.

The flow rate in such a crack $Q = 0.06$ l/s. This result is only 10^{-3} of the injected flow rate (50 l/s), which is consistent with $\mathcal{O}(1000)$ comparable cracks contributing to the flow. The fact that tracer is first detected after about 15 hours implies that there are some cracks in which v is about three times greater, and b about twice as large, but the fact that at this early time the tracer concentration is only about 10^{-3} of its peak value implies that very little mass flows through these larger cracks.

If there are $\mathcal{O}(1000)$ cracks in a resource of size $\mathcal{O}(0.5)$ km, the typical

distance between cracks is $\mathcal{O}(0.5)\,\text{m} \ll \ell_T$ for $t_r \gg 1$ week. On any time scale relevant to extracting energy (but not necessarily in a brief experiment) if the cracks are identical and distributed uniformly the rock temperature will vary little in directions perpendicular to the fluid flow and (provided $b \ll b_0$, as inferred) the produced water temperature T_w would be very close to T_r.

4.5.3 Analyzing tracer breakthrough curves with a one-dimensional model

We next consider a more quantitative assessment of a breakthrough curve by trying to eliminate trial-and-error fitting, while offering a rapid, easy-to-use approach suitable for someone working in the field. We can expect that we do not know three important parameters in the field test: the mean speed v, the dispersion coefficient $\mathcal{D}$, and the fracture opening b; only the first two parameters enter directly the breakthrough analysis above. Of course, we are assuming that the one-dimensional analysis is applicable; such analyses are occasionally described in similar terms in the literature (e.g. [55, 56]).

We use the dimensionless form of the one-dimensional analysis described above, equations (4-11 to 4-12). Let us define the time τ_m of the peak normalized concentration C_m (see Figure 4-10), the time $\tau_{1/2} = \frac{1}{2}\tau_m$ corresponding to the concentration $C_{1/2}$, and the time $\tau_4 = 4\tau_m$ corresponding to the concentration C_4. Manipulation of equation (4-11) then leads to

$$\frac{3\left(4\tau_m^2 - 1\right)}{2\left(2 + 3\tau_m - \tau_m^2\right)} = \frac{\ln\left(2C_4/C_m\right)}{\ln\left(C_{1/2}/\left(C_m\sqrt{2}\right)\right)}. \tag{4-13}$$

The right-hand side is simply evaluated based on the 3 concentrations C_m, $C_{1/2}$ and C_4 and the units used for concentration do not matter as this formulation only involves ratios of concentrations. Then τ is evaluated by inspection of Figure 4-12. Alternative, a simple root-finding algorithm on a laptop (e.g. using Mathematica) readily yields a unique value of τ_m.

With τ_m in hand we determine v according to

$$v = \frac{\tau_m \ell}{t_m}, \tag{4-14}$$
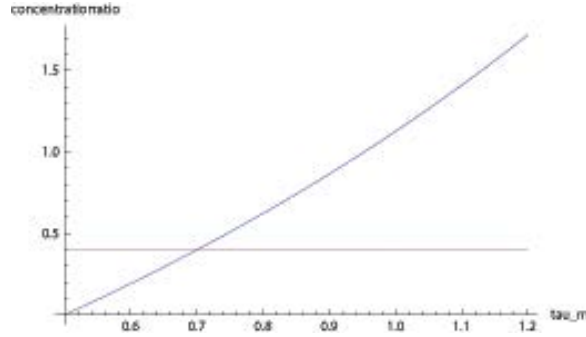
Figure 4-12: A plot of equation 4-13 where the right-hand side, is the vertical axis, here denoted "concentration ratio", is the input and then τ_m is read off the horizontal axis. The horizontal line is the value of the concentration ratio, here about 0.4, as determined from the data of Rose et al. [62] (Figure 4-11(a)).

where t_m is the time of the maximum concentration from the actual break-through curve. The Peclet number $\mathcal{P}_\ell$ for the tracer experiment is then determined rearranging equation (4-11) for two of the measured concentrations, e.g. C_m and C_4 according to

$$\mathcal{P}_\ell = -\frac{16\tau_m}{3\left(4\tau_m^2 - 1\right)} \ln\left(2C_4/C_m\right). \qquad (4\text{-}15)$$

With $\mathcal{P}_\ell$ determined the longitudinal dispersivity for the data follows from

$$\mathcal{D} = \frac{v\ell}{\mathcal{P}_\ell}. \qquad (4\text{-}16)$$

In this way, no trial-and-error fitting is required and, moreover, so long as the one-dimensional analysis is believed appropriate, the few steps above suffice to determine v and $\mathcal{D}$ from only 3 data points on a measured breakthrough curve.

Example: Using the Soda Lake data of Rose et al. [62], we find the right-hand side of equation (4-13) is ≈ 0.4 so that $\tau_m \approx 0.7$. Thus, we then determine $v \approx 9 \times 10^{-4}$ m/s, $\mathcal{P}_\ell \approx 3.1$ and $\mathcal{D} \approx 0.16$ m^2/s.

Moreover, with the values of v and $\mathcal{P}_\ell$ determined, we can show the quality of the fit to the data. In particular, we make time dimensionless and normalize the concentrations by the peak value (at t_m). The comparison is

49

shown in Figure 4-13(a) and captures the major features of the experimental curve.

(a)

(b)
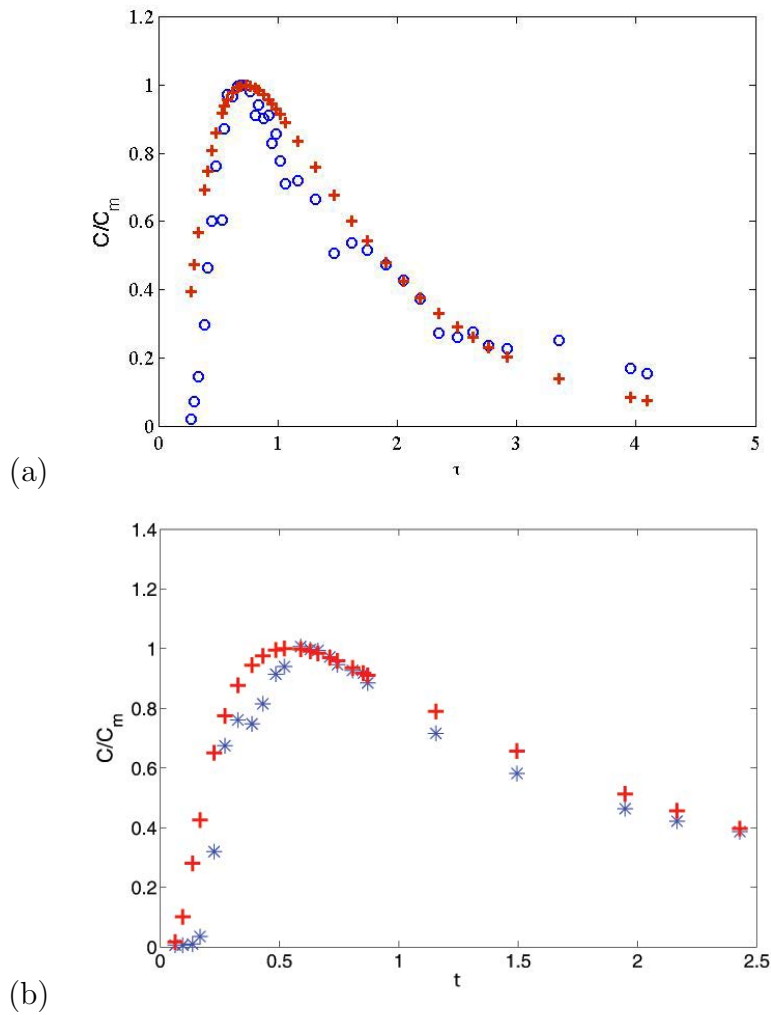
Figure 4-13: Comparison of the breakthrough data from Rose et al. (conserved, non-sorbing tracer), shown by the $*$ symbols, with the time-dependence, shown by the $+$ symbols, predicted by the one-dimensional analytical model, equation (4-11). (a) Soda Lake data [62]. (b) Steamboat data [63]. As described in the text, three data points are selected, v and $\mathcal{P}_\ell$ are calculated and the comparison is made.

50

We have performed a similar calculation for the non-sorbing tracer data available for the Steamboat geothermal site [63]. Here we estimate $\ell = 650$ m (based on Figures 2 and 3 in [63]) and find $\tau_m = 0.63$, which leads to $v = 6 \times 10^{-5}$ m/s and $\mathcal{D} = 0.027$ m^2/s. Again, as shown in Figure 4-13(b) we find that the one-dimensional analysis captures the major features of the experimental curve. Nevertheless, we are aware that this simplified analysis is not always so successful, as we found when analyzing data from the Soultz field [67] (though it may be possible to fit that data with a similar model involving two distinct values of τ_m, hence v and $\mathcal{D}$).

4.5.4 The dispersion produced by a network of cracks

There is a rich literature on dispersion in porous media, for which standard models consider packed beds of spheres, e.g. [60]. In addition, at the laboratory scale there are some studies of flow and dispersion in models characterized by "cracks" [68]; see Figure 4-14. Such models offer opportunities to better correlate spatial characteristics of a heterogeneous crack network with the resulting features, including the dispersivity, of tracer breakthrough curves. This kind of combination of laboratory-scale experiments and modeling, in conjunction with field-scale studies described above, offer one route for improved subsurface characterization.

4.6 Electromagnetic Imaging of Permeability

JASON proposes coupling tracer tests with electrically conducting fluids as one potential route to get more information about the spatial variations of the permeability in the neighborhood of injection and production wells. The idea is sketched in Figure 4-15. Since igneous rocks have electrical conductivities of about $10^{-6} - 10^{-3}$ S/m and sea water has electrical conductivities larger by at least 10^3, there are inexpensive options to inject a fluid, which can be identified relative to the rock, as the fluid migrates. In this way, injection tests, or injection-backflow tests, can yield valuable information on
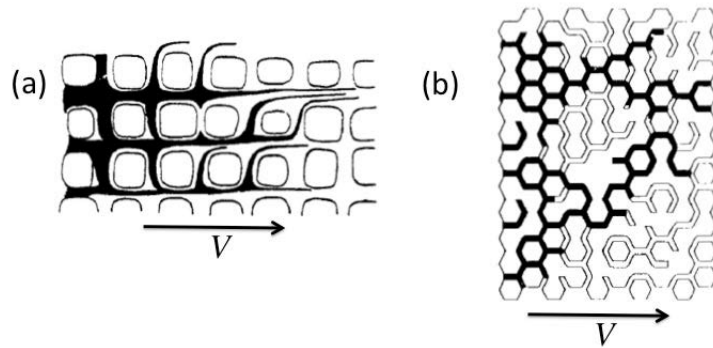
Figure 4-14: Schematics of two different two-dimensional network models for studying the dispersion of a tracer [68]. (a) A connected square lattice, where the channel width is random and the mean flow is parallel to one axis of the lattice. (b) Partly connected hexagonal lattice with uniform channel width where the network is above the percolation threshold; here the percolation parameter $p = 0.72$.

the permeability. For example, in the spirit of the one-dimensional tracer calculation shown above, it is straightforward to analyze a similar injection-backflow scenario to correspond with the kind of test sketched in Figure 4-15.

Magnetotelluric (MT) and other electromagnetic (EM) techniques are well established as means of characterizing the 3-D spatial distribution of fluids at depth, including in geothermal regions (e.g., [69]). Controlled-source MT is applicable to EGS-relevant depths [70], and short-range high-resolution methods such as GPR (Figure 4-1) can be applied to initial field experiments before one moves up to the spatial scales of production well-pairs [71]. Current state of the art applies joint inversion of multiple imaging methods, including seismic and gravity as well as EM (e.g., [72]–[75]). More controversially, imaging is improved if one can assume relationships between independently measured properties (e.g., seismic-wave velocity and electrical resistivity [75]–[77]), which may be reasonable for permeable zones of interest in geothermal applications.
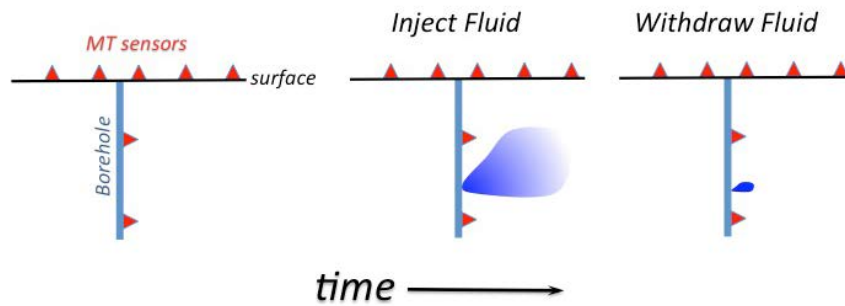
Figure 4-15: Schematic of an injection-backflow tracer test with an electrically conducting fluid, coupled with surface (and possibly borehole-emplaced) electromagnetic imaging to monitor spatial-temporal dynamics. Continuous temperature logging (e.g., by a fiber-optic probe) is also proven as an important tool for monitoring flow out of boreholes.

The specific approach we advocate is to monitor time-dependent changes in EM response through a combination of surface- and, to the degree possible, borehole-based measurements of electrical resistivity at depth (Figure 4-15). MT has been successfully applied to monitor EGS fluid injection, for example [78, 79], and time-dependent cross-well imaging is used for near-surface applications that may be relevant to initial (short-range) field experiments [80, 81].

4.7 Enhanced Subsurface Validation Made Possible by Micro Drilling

Micro drilling offers opportunities for enhanced subsurface characterization. Here we indicate possible ways that the use of micro drilling could be used to validate and improve models related to permeability of the reservoir, the fracture/flow network, and the interpretation of tracer (or other) tests.

All field-scale studies are based on spacings between injection and production wells, which typically are hundred of meters, if not actually several times more. It appears to JASON that using micro drilling to produce field tests with more closely spaced wells, e.g. tens of meters, can be used to test

various assumptions. For example, in all models (even ad hoc models) of flow and heat transfer in the subsurface the distance between the injection and production wells is a variable. Thus, micro drilling two wells at a spacing of tens of meters offers opportunities to more rapidly do various tests, e.g. tracer breakthrough experiments and heat transfer studies as a function of the applied pressure difference (or flow rate). In this way, the influence of the well spacing ℓ, the pressure drop Δp, the flow rate Q, the mean breakthrough time, the dispersion representative of a tracer experiment, etc. can all be tested and correlated (there would also be opportunity to use EM methods as described in the preceding section). Moreover, the variations of measured properties with time can also be performed in more controlled settings. In addition, when fracturing operations are performed, it is likely that the opportunities that micro drilling offers for getting improved spatial characterization of the flow field will be helpful in understanding better the creation of fracture networks in these subsurface environments.

Other kinds of tests can be envisioned. For example, with the kind of micro drilling approach above, perhaps combined with electromagnetic or seismic imaging, one can produce from multiple production wells, either in a line (so they are all on the same path) or on widely separated azimuths, simultaneously, i.e. pump whatever fluid is in the production well by reducing its pressure to zero. This approach might answer questions such as whether there is only one crack (or permeable zone) that might miss some of the wells, or if all rock out to some distance from the injection well is permeable. In addition, such a pumping test might answer a question such as "Does pumping from one well starve downstream wells, as it would in directed flow, or starve wells in all directions, as it would in diffusive flow?" Obviously, a new kind of field-site testing facility would raise other useful questions to address.

These types of operations can, in principle, offer ways to assess the spatial variation of the permeability in subsurface environments. For example, drilling one injection well and a series of production wells positioned at in-

creasing distances from the injection well allows for a systematic study by sequentially producing from only one well at a time. Then, flow experiments with first the closest production well opened, and then the next production well opened (with the first and all others closed), etc. should allow for improved understanding of spatial heterogeneities possible in subsurface environments.

5 EGS CREATION AND PRODUCTION

5.1 Heat Transfer Features of EGS

Two primary determinants of the possible success of a geothermal system, from conventional hydrothermal to hot dry rock (HDR), are the recovery factors for thermal energy and the possible lifetime of a given producing region. Both features require understanding the coupling of heat transfer to the water and the change of the thermal energy in the rock. These require knowledge of, or models of, the distribution of cracks and associated fluid flow at depth; the latter are poorly constrained, and all models make assumptions about the crack network or the average permeability of the reservoir.

An important characteristic of geothermal energy extraction is that where energy is extracted from a hot rock by contacting the rock with flowing (colder) water, the temperature of the rock is gradually reduced to approach the temperature of the injected water. In the absence of significant permeability of the rock, the thermal recovery of the rock can occur only by heat conduction, which is relatively slow. Hence, heat transfer considerations mean that within $t = 5$ years of contact with cool water the rock has been locally cooled over a distance of $\approx (4\kappa_r t)^{1/2} = (4 \times 5 \text{ yr} \times 30 \text{ m}^2/\text{yr})^{1/2} \approx 25$ m (where κ_r is the thermal diffusivity of the rock). One implication is that if an EGS system is to produce significant useable energy for more than a year or two, it must employ flow strategies that are tailored to the fracture network. In a network of closely spaced fractures, the "cooling waves" from neighboring fractures will quickly meet in the center of the rock that separates them and this rock will no longer push much energy into the water. However, if the flow is sufficiently slow, this will happen first at the injection end of the channels and propagate slowly toward the exit. In a network of widely spaced fractures higher flow speed may be useful, at least until the cooling wave becomes significant at the channel exit. We discuss these considerations, and illustrate them with example calculations, in this section.

There appear to be practical limits to how much energy can be usefully extracted from heat mining efforts once a thermal front has propagated from the injection point to the exit of the heat-transfer region. For example, if a thermal cycle is used to produce electricity, the temperature of the water is just as important as the rate at which energy is extracted from the rock. Below, we describe one strategy for reducing the rate of decay of the produced energy by reducing the water flow rate, which keeps the thermal efficiency reasonably high.

Thermal bypass: In terms of the order of magnitude characterization discussed above (based on thinking about a model set of uniform cracks), we can remark that the temperature of water within cracks wider than b_0 does not approach the far-field rock temperature T_{r0} because it flows too fast for sufficient heat to be conducted through the rock to the flowing water. (The water itself is taken to be isothermal across a narrow crack). Such wide cracks are a source of thermal bypass, mixing their cooler water with hot water from narrower cracks at the production well. Because the typical crack opening b_0 depends on both the pressure gradient and on the time t_r over which geothermal energy has been pumped, this kind of thermal bypass will develop gradually, and may (at the price of reducing the fluid and heat flow rate) be controlled by reducing the pressure gradient (see below). A second class of thermal bypass, resulting from heterogeneous depletion of rock thermal energy (i.e. cooling of the rock), can occur even for cracks narrower than b_0.

5.1.1   Description of the heat transfer problem

To assess and illustrate the fundamental heat transfer characteristics of an EGS system in HDR, we consider coupled one-dimensional models for temperature evolution in such a system. These models have a long history in geothermal engineering (e.g [82, 83, 84]), and JASON performed similar calculations to make independent assessments of the thermal evolution in the subsurface and to explore tradeoffs available to maximize useful energy
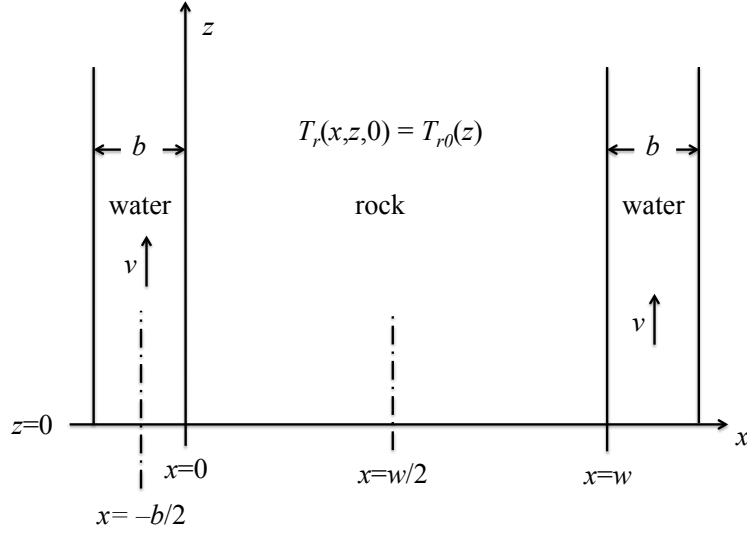
Figure 5-1: A vertical channel of width b and length ℓ (in z) in underground rock, with water injected at temperature T_{w0} flowing upward with speed v. In this section z is vertically upward, consistent with the direction of flow and standard use in heat transfer calculations, but opposite the standard geophysical notation where z is downwards from the Earth's surface.

production. We study first the simple case in which the rock temperature far from the channel remains constant, and we provide quantitative estimates of the time scale on which this is a good approximation. Then we consider later times, for which the rock temperature between flow channels decreases.

The heat transfer from the subsurface is characterized in a straightforward manner *assuming* a crack or simple crack network is present in the rock, e.g. Figure 5-1. Since cracks open up vertically due to the background lithostatic stress we assume for the summary presented here that the fluid flows vertically from an injection well to a production well. The crack opening is expected to be the smallest dimension so a one-dimensional model for the temperature of the water T_w has the form

$$\frac{\partial T_w}{\partial t} + v\frac{\partial T_w}{\partial z} = \kappa_w \frac{\partial^2 T_w}{\partial z^2} + \frac{2j_r}{C_w b}, \tag{5-1}$$

where j_r denotes the heat flux (energy/area/time) transferred from the rock to the water and the factor of 2 accounts for the two surfaces of the crack

(κ_w and C_w are the thermal diffusivity and volumetric specific heat of water, respectively). Typically we expect convective effects to dominate the heat transfer so the conductive term in equation (5-1) is neglected. The thermal evolution in the rock is determined by solving pure heat conduction in the rock:

$$\frac{\partial T_r}{\partial t} = \kappa_r \nabla^2 T_r \quad \Rightarrow \quad \frac{\partial T_r}{\partial t} = \kappa_r \frac{\partial^2 T_r}{\partial x^2}, \tag{5-2}$$

where x is directed into the rock and transverse to the flow direction (see Figure 5-1), with the latter approximation valid since transverse heat conduction occurs on a length scale $(4\kappa_r t)^{1/2} \ll \ell$. The heat flux $j = k_r \frac{\partial T_r}{\partial x}|_{x=0}$ from the rock to the water couples the water and the rock at their common interface, at which it is a good approximation that $T_w = T_r$. This boundary-value problem is well studied in the literature using analytical and numerical methods, e.g. [82], which is the model on which USGS estimates are based [1].

The analysis (see Appendix B) shows that after a time $t_{c1} \propto b^2/\kappa_r$, where b is the channel width, the water temperature in the channel equilibrates with the local rock-surface temperature. This takes only a few minutes for $b \approx 1$ cm. After this brief initial phase and once the first injected water has made its way to the exit of the heat-transfer zone , the equation for the water temperature becomes quasi-steady, i.e. $v\frac{\partial T_w}{\partial z} = \frac{2j_r}{C_w b}$. A "diffusion" front grows into the rock as the water progressively cools the rock, and a "cooling front" propagates from the injection point towards the channel exit. As a result, there is a distinct front between the region in which water has cooled the rock to its injection temperature, a narrow transition region, and a region in which the water has been heated to the initial rock temperature. Most of the heat transfer from rock to water occurs in this transition region.

As mentioned above and discussed in Appendix B, there is a second critical time t_{c2} when the transverse conduction front ("cooling wave") in the rock has propagated a transverse distance ℓ_T to the mid-point between two parallel cracks. This time is about $t_{c2} \approx \ell_T^2/(4\kappa_r)$. For example, if two parallel cracks are separated by $2\ell_T = 30$ m, the central rock temperature

will decrease on a time scale $t_{c2} \approx 2$ years. Even before this happens, the heat flow to the water has dropped from its initial transfer rate because it is driven by the temperature gradient in the rock, which falls approximately in proportion to $1/t^{1/2}$ if the cooling water temperature at a given position remains constant. Once the cooling waves collide the gradient falls even more quickly.

Finally, there is a third characteristic time scale t_{c3}, which is when the propagating "cooling front" reaches the exit of the heat-transfer zone (on its way to the production well). A balance of terms in the governing equations shows that it should be expected that the water can no longer be heated close to the ambient rock temperature after a time t_{c3}, where

$$t_{c3} \approx \left(\frac{C_r}{C_w} \frac{\ell}{vb} \right)^2 \kappa_r, \tag{5-3}$$

and where C_r and C_w are the volumetric specific heats of rock and water, respectively.

The time scale t_{c1} is short and not important for the performance of the EGS. However, the competition between t_{c2} and t_{c3} has significant implications for the useful energy that can be extracted from an EGS system and for it longevity. We illustrate this with a series of results below, following the discussion of energy production.

5.1.2 Illustrative examples

We illustrate with a series of results, which we obtained by solving our coupled 1D models as detailed in Appendix B. We consider the following geometry:

1. water injection at $z = 0$ at $T_{w0} = 320$ K;

2. heat-exchange distance, ℓ, of 1 km;

3. rock temperature of 550 K at $z = 0$, falling linearly to 525 K at $z = \ell = 1$ km;

61

4. b = crack/channel width = 1 mm;

5. Δy of channel = 10 m.

We take typical rock and water material parameters, detailed in Appendix B. We solve for the temperature distribution in the rock and water as a function of time and also compute the electrical power generation as a function of time (see the next section for a description of the calculation of the electrical power generation). We repeat this for different mass flow rates (meaning different flow speeds in this case, since we hold other parameters fixed).

The first example is designed to illustrate how poorly an EGS system can perform if water flows too quickly, which is a concern if there are a few large "bypass" flow channels. A high flow rate extracts the maximum thermal power but does not achieve high water temperatures and thus does not provide much *useful* energy. With the parameters above and a flow speed of 10 m/s, we obtain the results depicted in Figure 5-2. In this and subsequent figures, the color plot on the left illustrates the temperature distribution, with the water channel on the left (shown wider than its real size, for visibility), and the electrical power output is plotted as a function of time on the right. The time of the color plot is the last time at which an electrical power is plotted in the figure. In this first example, the color plot is at 5 years. This example illustrates several points. One is that the cooling wave does indeed propagate ≈ 25 m into the rock in a time of 5 years. Another is that power output starts low and drops quickly—approximately as $1/t$. We can see from how much the rock has cooled that substantial thermal energy has been mined. However, it has not been very useful, because the water temperature was low, because the flow rate was much faster than optimal. In terms of the critical times t_{c2} and t_{c3}, in this example t_{c3} (the time for the cooling wave to reach the top) is much shorter than t_{c2} (the time for horizontal propagation over a significant distance). This leads to nearly vertical temperature contours in the rock, in contrast to what we will see later.
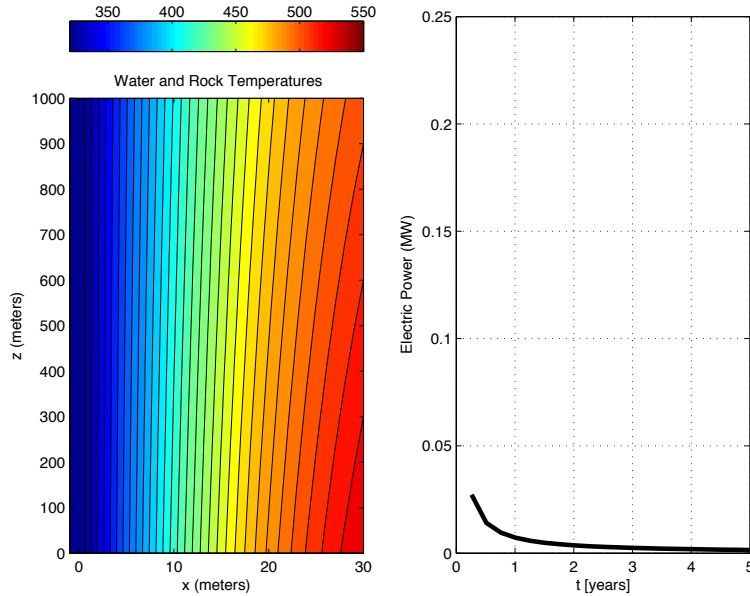
Figure 5-2: Results from example calculation with $v = 10$ m/s, shown at t = 5 years. On the left is a color contour plot of temperature in the water and rock system, with the water channel on the left made artificially wide for visibility. On the right is electrical power generation as a function of time. Flow speed is much too fast for useful power generation.

In our second example we reduce the flow by a factor of 10, so that $v = 1$ m/s. Results are shown in Figure 5-3. The rock temperature profile at $t = 5$ years is almost the same as in the $v = 10$ m/s case, which shows that the same amount of energy was mined. Nevertheless, electrical power generation is higher by approximately a factor of 8. This is a significant improvement. However, this is still suboptimal, and power still drops almost as fast as $1/t$.

For the third example we reduce the flow by another factor of 10, so that $v = 0.1$ m/s $= 10$ cm/s. The state at $t = 5$ years is shown in Figure 5-4. We see qualitative differences between this and the previous cases. Temperature contours in the rock are not vertical, and the water exiting temperature is significantly higher than its entering temperature. Electrical energy generation is substantially higher than in previous cases, and it is not dropping as steeply. The power at early times is only $\approx 20\%$ higher than in the $v = 1$

63
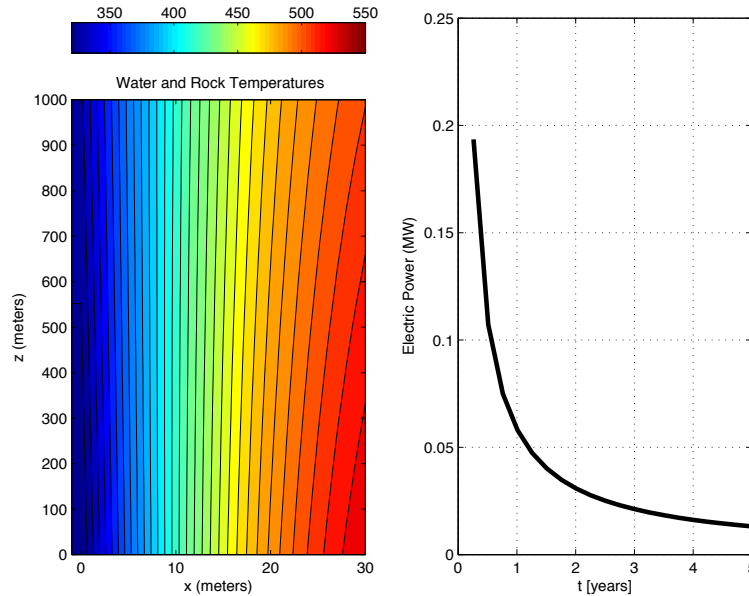
Figure 5-3: Results from example calculation with $v = 1$ m/s, shown at $t = 5$ years. Flow speed is still too fast for optimum power generation, although it is much improved over the $v=10$ m/s case.

m/s case, but at $t = 5$ years it is higher by a factor of ≈ 4. Comparison of the rock temperature contours at $t = 5$ years shows that with the slower flow speed the system has not mined as much thermal energy, even though it has generated much more electrical energy.

Figure 5-5 shows the temperature field for the same flow speed at an earlier time of $t \approx t_{c3}$, when the rock at the top of the heat-exchange zone has just begun to cool. This illustrates that a flow speed of ≈ 0.1 m/s for this crack geometry makes t_{c2} and t_{c3} approximately the same. We suggest that this is a good guiding principle for maximizing useful energy output, at least until $t \approx t_{c3}$.

The final example illustrates the results of a very slow flow speed. The state at $t = 5$ years is shown in Figure 5-6. Slow flow maximizes water outlet temperature and thus maximizes efficiency of conversion to electricity, but it produces a slow rate of energy extraction. This system would continue

64
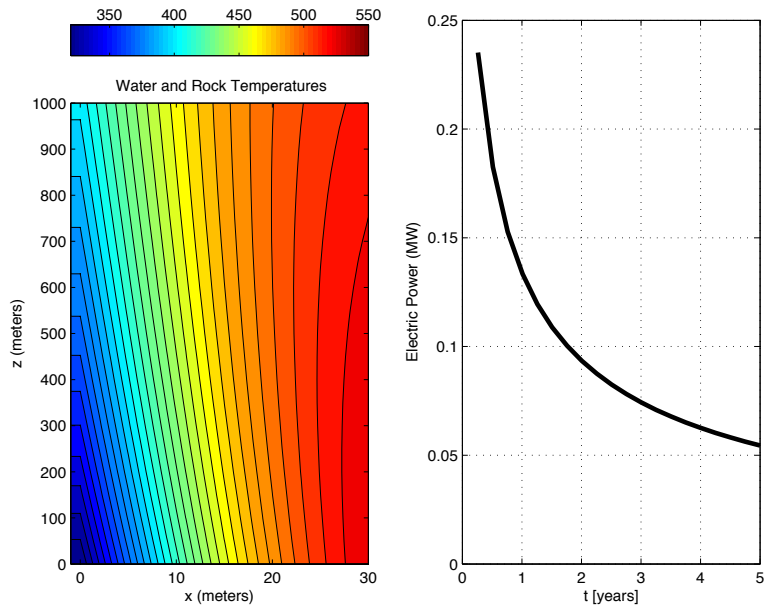
Figure 5-4: Results from example with $v = 0.1$ m/s, shown at $t = 5$ years. This system's performance is substantially improved over the faster-flow systems.
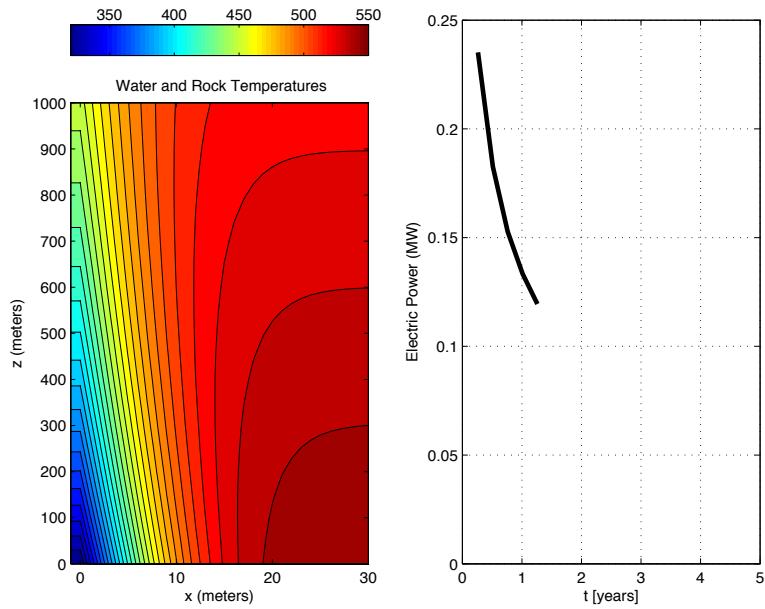
Figure 5-5: Results from example with $v = 0.1$ m/s, shown at $t \approx t_{c3}$.
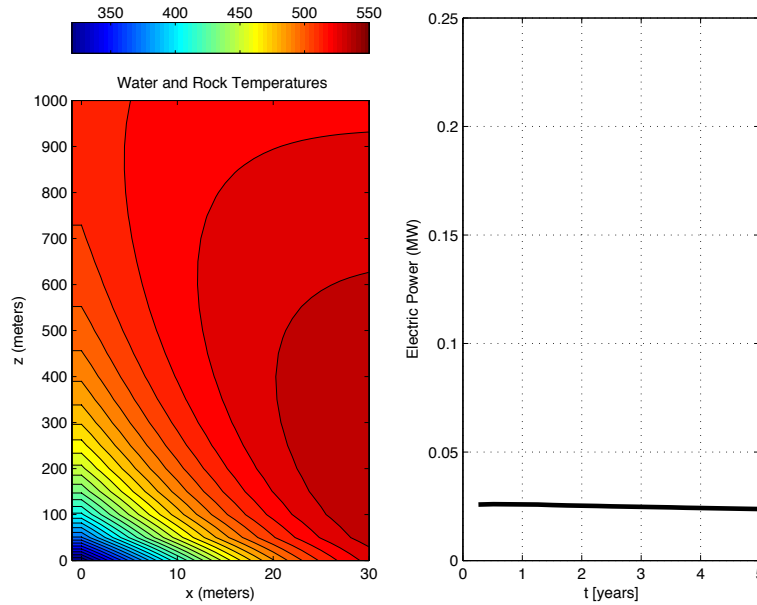
Figure 5-6: Results from example with $v = 0.01$ m/s, shown at $t = 5$ years. Slow flow maximizes water outlet temperature and thus maximizes efficiency of conversion to electricity. It also maximizes the time over which power does not drop substantially from its initial value. The trade-off is that the almost-steady power level is relatively low.

to produce electricity for many years without the substantial drop in output that accompany faster flow systems.

These examples illustrate the crucial role of water flow rate in EGS systems. A network of fractures that has many narrow cracks but a few wider ones will be in danger of performing much like the high-flow examples shown above, with low water outlet temperature and correspondingly low utility of the extracted energy (e.g., abysmal efficiency for electrical generation).

5.1.3 Energy produced as a function of flow rate

An important quantity is the energy transferred to a water channel per unit time (the "thermal" channel power, P_{th}^{ch}). As above, we denote the channel opening b, the mean water speed v, and the injected water temperature

T_{w0}. We can determine the time evolution of the exit temperature $T_{w,ex}$ from a channel of width Δy. We find

$$P_{th}^{ch} = (400 \text{ kW}) \left(\frac{\dot{m}}{1 \text{ kg/s}}\right) \frac{T_w(z_{\text{ex}}) - T_{w0}}{100 \text{ K}} , \tag{5-4}$$

where

$$\dot{m} \equiv b \, \Delta y \, v \, \rho_w = \text{mass flow rate.} \tag{5-5}$$

For example, given a 1 mm crack with $\Delta y = 10$ m, a flow speed of 10 cm/s corresponds to 1 kg/s of flow. In this case, if the water gains 100 K from the rock during its journey, the 1 mm $\times$ 10 m channel will yield 400 kW of thermal power.

Thermal power is important, but it is not the whole story. We illustrate the importance of exit temperature by considering electricity production. We assume near-maximum thermodynamic efficiency of electricity generation P_e^{ch} in which case the electrical power produced from the heated water is estimated as

$$P_e^{ch} = P_{th}^{ch} \left(\frac{T_{w,ex} - T_{w0}}{T_{w,ex}}\right). \tag{5-6}$$

Combining the previous two equations yields

$$P_e^{ch} = (400 \text{ kW}) \left(\frac{\dot{m}}{1 \text{ kg/s}}\right) \frac{(T_w(z_{\text{ex}}) - T_{w0})^2}{(100 \text{ K}) T_{w,ex}}. \tag{5-7}$$

This equation highlights the importance of maintaining a high water temperature at the outlet of the heat-exchange zone. EGS flow strategies should be designed with this in mind.

5.1.4   Flow strategies

The examples above considered a variety of flow rates but in each example the flow rate was held constant for the entire five-year period. With some simplifying assumptions we can generalize the behavior of a flow channel under constant flow conditions. We have done this for the channel electrical power as a function of time, and the results are in Figure 5-7.

Given constant flow, we can identify three phases in electrical power production from a given channel: a short phase in which water temperature achieves equilibrium with the rock surface temperature, an intermediate phase as the thermal wave in the rock develops in the z direction, and a final stage in which the electrical power output drops more quickly than it did before t_{c3}. In the final stage, power will eventually drop like $1/t$ even if channels are spaced far apart, and it will drop more quickly if channels are close enough for their cooling waves to interact.
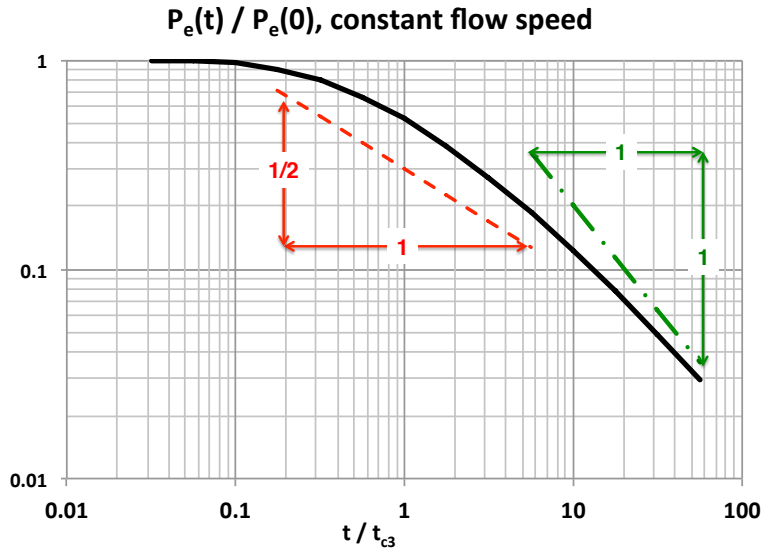
Figure 5-7: Electrical power as a function of time for constant flow conditions during the "intermediate time period. With constant flow conditions there are three phases: an early phase of approximately constant power, a second stage when power drops roughly as $t^{-1/2}$, and a later stage when power drops roughly as t^{-1}.

Figure 5-7 shows a strong decay of power production for times past t_{c3}. We can slow the decay of the power production by altering the flow through the channel. Consider the following flow strategy: begin with constant flow rate until the thermal front in the rock reaches the production well at about t_{c3}, then decrease the water speed in proportion to $t^{-1/2}$. This approach transfers roughly the same amount of energy to the water but keeps the exit temperature constant, and so maintains reasonably high thermal efficiency.

68
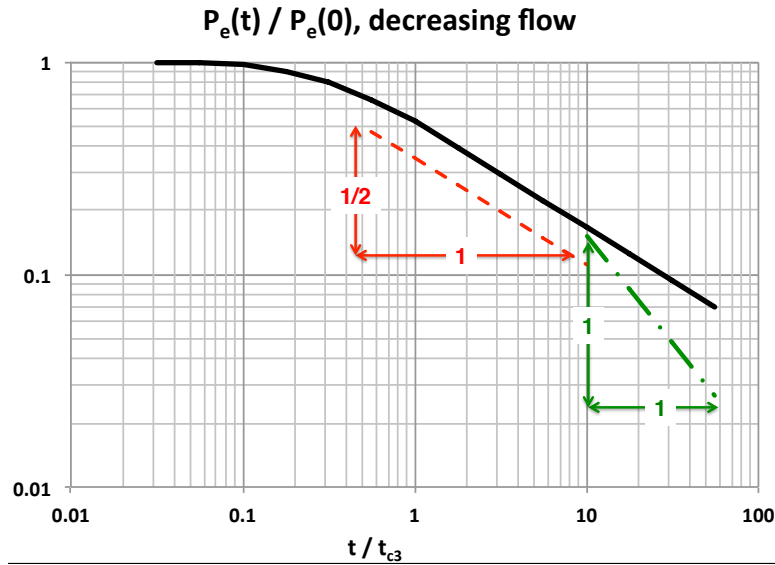
Figure 5-8: Electrical power as a function of time for flow that is constant until the thermal front reaches the production well, after which flow speed drops as $t^{-1/2}$. With this flow strategy, electrical power generated never drops faster than $t^{-1/2}$.

The resulting electrical power production is shown in Figure 5-8. The price for this decrease in flow rate is that the channel thermal power decreases proportional to $t^{-1/2}$. This decrease is not as steep as that of the constant-flow case (Figure 5-7), so this appears to be a superior flow control/heat transfer strategy. Again, for times late enough that the deep-rock temperature decreases because of communication between channels, the power decreases will be steeper than these results indicate. However, this may happen after the power has already dropped enough to end the practical life of the well.

5.1.5 Remarks

The various JASON analyses are consistent with the kinds of hydrodynamic and transport (thermal and chemical) modeling that has been developed in the geothermal field over the past 30+ years, which forms the basis for the quantitative assessments of identified geothermal fields made by the USGS in 2008 [1]. Nevertheless, these assessments assume a fracture field

exists for the flow and heat exchange, and highlight that the spatial features and heterogeneities of the fractures, i.e. the reservoir permeability, is the primary uncertainty in being able to provide rational assessments of the short- and long-term features of geothermal sites. This viewpoint further emphasizes the need for subsurface characterization. It also provides motivation for the JASON suggestion to consider engineering subsurface heat-exchange systems as one route to eliminating uncertainty in the subsurface heat transfer necessary for power production.

5.2 Wholly Drilled Heat Exchanger

Advances in drilling technology and in particular advances in micro drilling suggest that it is worthwhile to consider engineering permeability in otherwise dry rock by drilling properly spaced holes directly between injection and production wells. Various detailed calculations are possible but here we simply estimate the mean power possible if the water can be heated to approximately the mean temperature between the rock and the injected water.

An upper bound on the energy to be produced is to assume that thermal energy is extracted in time t_r from the hot rock over a radial distance $\sqrt{\kappa_r t_r}$. Then, per unit length of such a drilled circular hole we extract energy from the surrounding rock on a volume $\pi \left(\sqrt{\kappa_r t_r} \right)^2 \ell$, or

$$\text{energy/length in time } t_r = (C_r \Delta T) \, \pi \kappa_r t_r \tag{5-8}$$

which corresponds to a maximum power (per length of pipe)

$$\text{average power/length } = (C_r \Delta T) \, \pi \kappa_r. \tag{5-9}$$

Using typical values for rock (granite), and assuming a temperature change $\Delta T = 100\,°\text{C}$ we find

$$\text{average power/length } \approx 0.75 \text{ MW/km.} \tag{5-10}$$

Since a plausible efficiency of power generation in these modest temperature geothermal systems is about 15% then we estimate the average electrical power production per unit length of drilled heat exchange pipe to be $\approx$ 0.1 MW_e/km. Obviously, a lower value for the change in temperature ΔT of the rock will proportionately decrease this power estimate.

Maximum energy extraction over a period 10 years would require drilling such pipes spaced apart $2\sqrt{\kappa_r t_r} \approx 30$ m. Heat mining from 1 cubic kilometer of rock then requires about 1000 drilled pipes. Better estimates are possible by more detailed calculations.

The required pressure drop is not expected to be an issue for such a system since even a narrow diameter borehole may have a large fluid admittance. For example, for a 1 km pipe, the previously discussed 0.75 MW_t and $\Delta T = 100\,°C$, the flow rate is 1.7 l/s. In a $1''$ diameter borehole the mean velocity is 3.4 m/s, the Reynolds number is about 3.1×10^5, the friction factor $f = 0.038$ for an assumed surface roughness of $0.01''$ and the pressure drop is 90 bar/km or 9 MPa/km. The fluid admittance for a single 1 km long borehole $A = .024$ l/s-bar or 0.24 l/s-MPa. If indeed an array of 1000 boreholes in parallel was drilled (with a total thermal power of 750 MW_t and electrical power 100 MW_e) the admittance would be $A = 24$ l/s-bar or 240 l/s-MPa. These parameters are consistent with those usually discussed for EGS.

In order to understand possible design features of an engineered heat exchanger, e.g. how long such a heat exchanger should be in order to still produce a significant change in water temperature after 10 years, we give an approximate heat transfer calculation for a circular pipe of radius b. We assume the pipe has been drilled and that there is an appropriate liner to eliminate any leakage of the heat exchange fluid.

As discussed in the sections on heat transfer a one-dimensional description of the temperature change in the water is

$$v\frac{\partial T}{\partial z} = \frac{2j_r}{bC_w},$$

(5-11)

71

where C_w is the volumetric specific heat of water and j_r is the time varying heat flux from the rock to the water. We expect that for individual pipes large enough to transport sufficient hot water for power generation the flows will be turbulent and so well mixed in the cross section, which supports this one-dimensional approximation.

Since the only mechanism of heat transfer in the rock is heat conduction we can determine the radial heat flux j_r by analyzing the heat conduction outside a cylinder of radius b. Here we just give an approximate scaling argument. We expect that on time scales such that $(\kappa_r t)^{1/2} < b$ this heat flux is controlled by the short length scale $(\kappa_r t)^{1/2}$, but as time progresses $(\kappa_r t)^{1/2} > b$ in which case the heat flux is controlled by b with (time-dependent) logarithmic corrections as a consequence of the radial geometry, i.e. approximately

$$j_r \approx \frac{k_r \left(T_r - T \right)}{b \ln \left(\frac{(\kappa_r t)^{1/2}}{b} \right)}, \tag{5-12}$$

where k_r is the thermal conductivity of the rock.

Using (5-12) we can solve the differential equation (5-11) with the boundary condition that $T(0,t) = T_w$ is the initial water temperature to obtain an estimate for the evolution of the water temperature $T(z,t)$ along the pipe:

$$\frac{T_r - T(z,t)}{T_r - T_w} = \exp \left\{ -\frac{2 C_r \kappa_r z}{C_w b^2 v \ln \left(\frac{(\kappa_r t)^{1/2}}{b} \right)} \right\}. \tag{5-13}$$

Note that this expression involves the volumetric specific heat of the heat-exchange fluid and is only weakly dependent on time, which only appears explicitly in a logarithmic factor.

An engineered system will need to have drilled a length ℓ of a hole sufficient that the heat exchange remains economically viable for many years. The corresponding length of the heat exchanger is then

$$\ell \approx \frac{C_w b^2 v}{2 C_r \kappa_r} \ln \left(\frac{(\kappa_r t)^{1/2}}{b} \right) \ln \left(\frac{T_r - T_w}{T_r - T(\ell,t)} \right). \tag{5-14}$$

In terms of the available thermal power P associated with the high temperature water $P \approx QC_w\Delta T$, then the length of pipe needed for the desired power is

$$\frac{\ell}{P} \approx \frac{1}{2\pi C_r \kappa_r \left(T(\ell, t) - T_w\right)} \ln\left(\frac{(\kappa_r t)^{1/2}}{b}\right) \ln\left(\frac{T_r - T_w}{T_r - T(\ell, t)}\right). \qquad \text{(5-15)}$$

Again, it is important to note that this expression is only weakly dependent on time. However, this result is independent of the properties of the heat exchange fluid.

For example, suppose a reservoir has a temperature of 250° C and after 10 years of operation we still desire water temperature 150° C (where the inlet temperature is 50° C) to be produced from micro drilling a hole of diameter 1 inch or $b = 1.3 \times 10^{-2}$ m. Then, after the 10 years, in order to produce thermal power of 1 MW we would need to have drilled a pipe of length $\ell \approx 2.5$ km. This length is the order of magnitude suggested for advances in micro drilling. Furthermore, after 40 years of operation the thermal power produced would only have decreased by 10 % (or would be 0.9 MW). Based on these estimates JASON concludes that the engineered heat exchanger is a plausible idea worth further consideration.

5.3 Water

Fresh water withdrawal and consumption is an important and sensitive issue for geothermal plants operating in water-stressed areas. In addition to uses common to construction projects, geothermal systems use water when drilling wells, and to create hydraulic pressure to fracture the rock. The major water consumption, however, arises during routine operations, when water is used to cool surface heat exchangers and as feed water to replace losses from the hydrothermal reservoir. For hot dry rock or where natural hydrothermal waters become depleted, enhanced geothermal systems (EGS) also require a water supply to charge the reservoir initially. Moreover, experience has shown that natural hydrothermal systems gradually lose water

after years of operation, and even ones in "hard" rock often have channels that bleed water from the system.

Some geothermal systems, e.g. The Geysers in northern California, produce hot steam with low water content (dry steam) directly from the ground, which directly drives a turbine. The exhaust is vented to the atmosphere, although in such systems the steam can also be condensed and returned to the reservoir. When hot water comes to the surface, one approach feeds it into a tank at lower pressure, causing it to flash into steam which then can drive a turbine or heat exchanger. In one version of flash systems, the geothermal fluid heats an organic fluid in a closed loop that vaporizes at a lower temperature, drives the turbine, and returns through a condenser (Figure 5-9). Cooling water is needed for the condenser for these systems, as well as to make up water lost underground. In addition, some systems are cooled by air, known as dry cooling. This works well during cold weather but loses efficiency, sometimes by factors of two or more, in summer, when electrical demand is greatest in much of the U.S. (see also [86] and [24]).
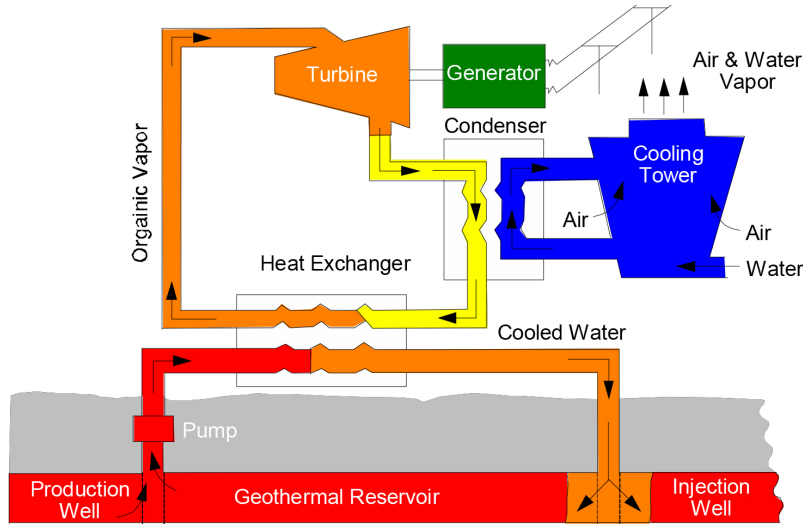
Figure 5-9: Geothermal system with binary cooling [85]. Water pumped to the surface in a production well passes through a heat exchanger and is returned to the geothermal reservoir. An organic compound that vaporizes at a temperature lower than the hydrothermal water drives a turbine and is recycled through a condenser which is cooled with water.

Estimates of water consumption demonstrate that geothermal power systems configured with a water cooling tower generally consume more water per unit of electrical energy than other power sources (Table 5.1)[2]. This high water usage per unit energy produced is primarily due to the lower Carnot efficiency resulting from the water temperature available from the reservoir, along with subsurface losses. Nevertheless, geothermal plants are expected to implement air cooling wherever possible, which, in principle, substantially reduces water usage, perhaps to near zero. We discuss this important point next.

Not indicated above is the wide variance of water estimates that can be found for geothermal power. For example, Harto, et al. (2013) [24] take a value of 40 m^3/TJ for above-ground water consumption, assuming that air cooling is used with EGS systems. Yet, as we note below, they also estimate subsurface water losses to amount to about 10^3 m^3/TJ for EGS, so the overall concern regarding water use – above and below-ground – is whether it amounts to 1000 or 2000 m^3/TJ for EGS (see also Macknick, et al., 2011) [87].

As another example of disparate estimates, in their 2006 Geothermal Task Force report [88], the Western Governor's Association states that a new geothermal flash plant would consume 5 gallons of fresh water per MWh compared to 361 gal/MWh for a new gas plant. The geothermal estimate is equivalent to 0.0053 m^3s^{-1}/TW, compared to 10 m^3s^{-1}/TW in Table 5.1 for a similar situation. The low estimate presumably assumes steam release to the atmosphere rather than cooling by air alone, and no need for reservoir recharge.

To assess the water consumption that could occur if some recharge of the geothermal recirculating fluid is needed, we consider the electrical power

---

[2]For water consumption associated with energy production, many different units are used in the literature. We convert among units according to the following: 1 gal/kWh = 10^3 gal/MWh = 3.8 l/kWh = 3.8 m^3/MWh = 1.05 l/MJ = 1.05×10^3 l/GJ = 1.05 m^3/GJ = 1.05×10^3 m^3/TJ

Table 5.1: Volumes of cooling water consumed per unit production of electrical energy, in units of m^3/TJ_e. The values are from engineering calculations [89], [90] except for the geothermal value which is from [91, 24]. The geothermal value applies to wet or hybrid system above-ground losses plus approximate estimates of subsurface losses.

Process	Water Consumption
Gas (CCGT)	220
Coal (steam turbine)	540
Nuclear (steam turbine)	660
Solar thermal	780
Geothermal	800-1800

for a geothermal system

$$P = \rho C_p \Delta T Q \eta \qquad (5\text{-}16)$$

where ρ is the density of the water, C_p is the specific heat of the fluid at constant pressure, ΔT is the temperature drop across the heat exchanger, Q is the volume flow rate, and η is the efficiency.

We can evaluate the geothermal flow rate Q as a function of power for $\Delta T = 100$ K and 200 K, using C_p=4200 J kg^{-1} for the specific heat of water at constant pressure. In practice, C_p may be smaller because of its dependence on temperature and salt concentration. Geothermal water flow for a hot system, 200 K, is about 5000 m^3 s^{-1} per GW and the estimate for a 100 K system is about twice that.

In an ideal case, once charged, all reservoir water would be re-used without losses. If there are losses in the system that require recharge of the recirculating fluid, the water consumption would increase, although it is possible that non-fresh water could be used. EPRI [92] estimated that with about 10% losses, consumption would increase by about 1000 m$^3/TJ_e$ above consumption for cooling. As noted above, Harto et al. (2013) [24] give similar numbers for potential below-ground losses in the life-cycle assessments of EGS; such estimates are uncertain at the present time, however.

Water usage is of particular concern for geothermal systems because the western states of the U.S. have the highest geothermal potential, but most of the western state locations also have the lowest rainfall (Figure 5-10). Among the states, Nevada has both the highest potential and the lowest rainfall. It also has low recharge rates for its aquifers.

As a case study, in June 2013 several JASON members toured the Coso geothermal plant outside Ridgecrest, CA. A well-established natural system lying along a fault, Coso produces about 260 MW. In addition, presently about 40% of water from production wells is lost to steam. After a four-year legal fight, the plant won the right to add up to 3,000 gallons per minute ($0.19 \text{ m}^3\text{s}^{-1}$) from a well on land owned by their parent company (Andrew Sabin, personal communication). In addition, flow is watched by local Indians who are concerned about the health of their sacred fumaroles nearby.

An upper bound for water consumption at the Coso geothermal plant assumes current power production using all of the 3,000 gallons per minute ($0.19 \text{ m}^3/\text{s}$) allowed from the Hay Ranch property, yielding a value of 730 $\frac{\text{m}^3}{\text{TJ}}$.

Recovering only $\approx 20\%$ of their natural steam, the Geysers found a creative solution to their water needs by using recycled (waste) water from Lakes County (9×10^6 gallons per day) and the city of Santa Rosa (12×10^6 gallons per day). The Santa Rosa project began in 1993 after the city was facing problems from discharging treated recycled water in the Russian River, and was completed in 2004, requiring 40 miles of pipes some 48 inches in diameter. The Geysers web site states that the combined recycled water consumption rate is $\approx 1 \text{ m}^3\text{s}^{-1}$. The water consumption for recharge for the ~ 700 MW facility is therefore about 1460 m^3/TJ. However, the use of recycled water allows this to be met without withdrawing fresh water from the local watershed.

U.S. Geothermal Provinces

- 🔴 Temperatures Above 100°C (212°F)
- 🟠 Temperatures Below 100°C
- 🟡 Area Suitable for Geothermal Heat Pumps (Entire U.S.)

EXPLANATION

Mean annual precipitation, in inches
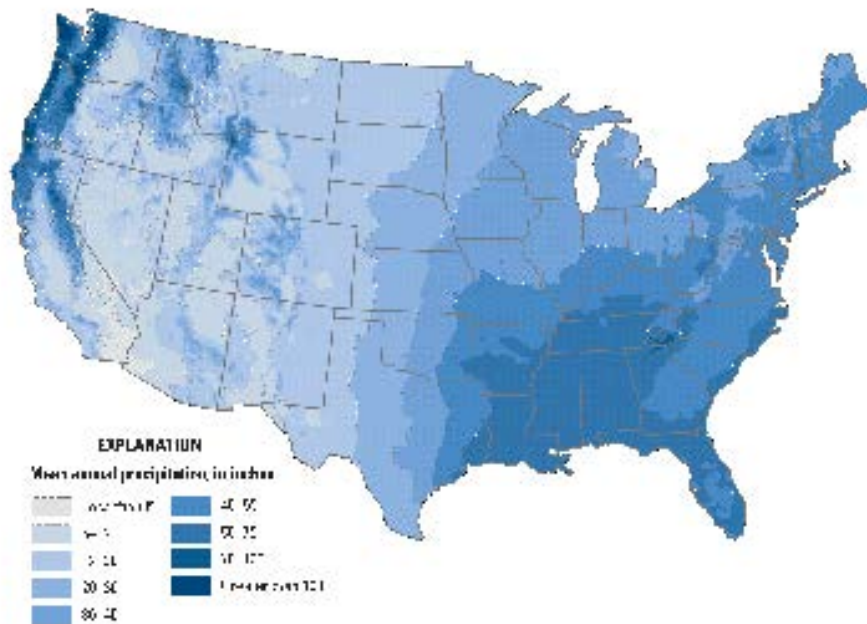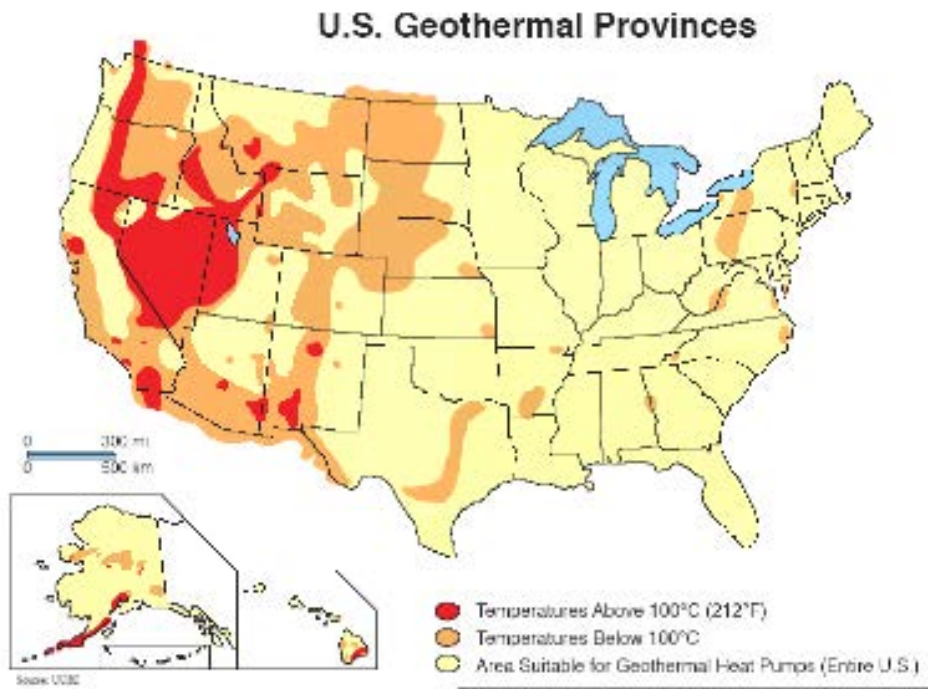
Figure 5-10: Map of U.S. Geothermal Provinces [93] (top) and annual precipitation [94] (bottom). Nevada has both the highest geothermal potential and the lowest precipitation in the U.S.

In summary, water availability can be a significant factor in operating geothermal plants in areas of water scarcity, and could become a limiting constraint for EGS at scale (see also Harto, et al., 2013 [24]).

5.4   Corrosion and Scaling

Conventional geothermal systems have significant problems with corrosion or scaling of transfer piping, and this will be an issue for EGS systems as well.

Although there is a discussion in the literature of novel possibilities using CO_2 as a heat-transfer medium, essentially all geothermal systems in operation today extract underground heat with some combination of steam and salty hot water (brine). In California, the Geysers geothermal plants in California represent one extreme, where steam carries most of the heat to the surface. The geothermal plants at the Salton Sea represent the other extreme, where much of the heat is carried by brine, which flashes to steam near the surface. High-temperature heat sources tend to be dominated by steam and lower-temperature sources by brine.

Corrosion and scaling can be caused both by gases mixed with the steam and by various substances dissolved in the brine. Much of the corrosion at the Geysers fields is caused by hydrogen chloride and hydrogen sulfide gases mixed with the steam. Brines are a mixture of dissolved substances, including dissolved CO_2, bicarbonate and carbonate ions, with relative amounts fixed by the pH of the brine, orthosilicate ions, chloride ions, sulfates or sulfides (depending on the redox state of the brine), cations of calcium, magnesium, sodium, iron, and many other metals.

Particularly troublesome is the carbonate chemistry of the brine, which can lead to intolerable scale formation, especially at high pH where bicarbonates ions which combine with ubiquitous Ca^{++} ions are converted to form deposits of solid calcium carbonate, $CaCO_3$, usually in the form of calcite.

Precipitation conditions are hard to predict because the solubility of $CaCO_3$ has substantial dependence on temperature and pressure. Precipitation rates also depend on the concentration of other ions, for example Mg^{++}, which can suppress the formation of calcite in favor of aragonite, as it does in the oceans today. The use of supercritical CO_2 as a heat transfer medium is likely to exacerbate the problems of carbonate chemistry, and to introduce unanticipated new problems.

None of the chemical problems mentioned here need to be show-stoppers for EGS, but solving them will require time, funds, talent and research.

5.5   Induced Seismicity

One consequence of geothermal production is the generation of earthquakes. Induced seismicity is a relatively well-documented phenomenon associated with changing fluid pressures at depth, for instance due to impounding water behind a dam or injecting fluids into the crust, and it has on more than one occasion caused significant public concern with EGS and other geothermal projects (National Research Council, 2012; Ellsworth, 2013) [95, 96]. Small earthquakes are also caused by hydro-fracturing, as may be used for EGS stimulation, e.g., Julian et al., 2010 [97]; in fact, micro-earthquakes provide important information about the spatial distribution of stimulated zones at depth, so could have been discussed above as part of subsurface characterization (see Flewelling, et al., 2013 [98], for a recent example from the oil and gas industry).

We start, however, by noting that seismicity can be directly attributable to geothermal production, specifically to the net volume of fluid (extracted – injected volumes) in the subsurface [95, 99]. More work is needed to characterize all factors controlling seismicity associated with production, but the important point is that there is a basis for controlling the induced seismicity

and therefore for minimizing this potential hazard attributable to EGS (see also Mena, et al., 2013) [100]. Independent review has lauded DOE planning on this issue [95].

In addition, there are promising advances in understanding the stress changes associated with EGS-induced seismicity, suggesting that detailed monitoring can be used to provide quantitative monitoring at depth (e.g., Catalli, et al., 2013) [101]. This is of interest not only for reducing the hazard during production, but also as a means of characterizing subsurface volumes undergoing hydro-fracturing or other stimulation for EGS development.

Such stress measurements are complementary to the electromagnetic imaging and tracer-measurement schemes described in §4 in defining the spatial-temporal evolution of flow paths (permeability) at depth. We note the emerging sense that both the mechanical state and flow paths in the crust may typically be in a critical state, with highly nonlinear response to external forcing. For instance, small stresses (e.g., from distant earthquakes) can significantly alter flow paths or even induce rupture on critically loaded cracks (e.g., Manga, et al., 2012; Ellsworth, 2013; van der Elst, et al., 2013; Wang, et al., 2013) [96], [102] – [105].

Microseismicity (numbers and locations of events) can be monitored over thousands of meters, but we advocate more detailed measurements coupling estimates of spatio-temporally varying permeability and stress-state based on coupling tracer and electromagnetic with seismic methods. In order to further develop and validate these approaches at field-scale, initial studies could be applied across short distances (e.g, tens of meters), possibly using the micro drilling ideas discussed in Section 4.7 before moving to the more practical scales relevant to EGS stimulation and production monitoring (hundreds of meters or more).

6 POTENTIAL GAME-CHANGING TECH-NOLOGIES

6.1 Overview

The purpose of this section is to summarize material from the foregoing discussion, prioritizing the technologies in terms of those we consider most likely to impact EGS development most immediately. EGS offers important opportunities for increasing the contribution of geothermal energy to U.S. power production: by a few-fold over the next few years, according to our estimation, and much more so if this initial success is appropriately leveraged over subsequent years (§3).

Key technical choke points are well identified at present, including characterization of subsurface flow so as to be able to predict and control heat recovery factors and well-pair lifetimes. There have been relevant technological breakthroughs, both for subsurface characterization (§4) and for production (§5), and in many cases the next essential step is to develop and validate these capabilities at field scale.

Synergies with other applications

Many of the technical challenges addressed by EGS research are of broad interest to industry, academia and government. Notably, imaging and characterization of the subsurface and of subsurface flow – including through rapid access as potentially made feasible by micro drilling and related technologies – is important for many parts of the U.S. Government. Within the DOE, underground isolation of radioactive waste, carbon sequestration and mitigation of subsurface fluid contamination (hence monitoring it as a function of space and time) are particularly relevant, with similar responsibilities in other agencies (e.g., EPA).

Artificial structures at depth are of special interest to the DoD and DHS, whether tunnels, storage facilities, or centers for command and control

(e.g., hard and deeply buried facilities [106, 107]). To be sure, many of these structures are only at tens or hundreds of meters depth, rather than the thousands of meters relevant to EGS. However, some are at depths comparable to the shallower ranges considered here for EGS, and there is no doubt that improved characterization and more rapid access to such depths (e.g., by micro drilling) would be of great practical utility.

We also note the potential significance of rapid drilling to multi-km depth for measuring temperature changes across the epicentral region of a fault shortly after it has experienced an earthquake. Such measurements have great importance for quantifying frictional dissipation associated with seismic rupture, a key issue in current academic and government (e.g., USGS) research on earthquake source mechanics.

6.2 Technologies

6.2.1 Drilling

Advances in drilling can significantly impact EGS. On the one hand, drilling remains one of the major expenses in exploration, development and production of EGS. On the other hand, there are major opportunities for advances in drilling to facilitate EGS, not necessarily requiring new technologies but even with field-scale applications of existing technologies.

In particular, micro drilling holds great promise because of the rapidity and reduced costs with which boreholes can be emplaced. This is especially important for subsurface imaging and characterization, for example with deployed seismic and electromagnetic sensors at depth, and for injection and sampling of tracer fluids (including electrically conducting fluids that might be imaged electromagnetically). Current capabilities in altering fluid flow (e.g., with temperature-sensitive packers) and in continuously monitoring temperature using downhole fiber-optics is impressive, and would be far more widely applicable to optimizing production if probe wells could be drilled

more quickly and inexpensively than at present.

More speculatively, we note that micro drilling may supplement hydraulic fracturing (and perhaps even explosive fracturing) in creating engineered heat exchangers at depth. We acknowledge that the primary production wells typically need to be larger for effective production of geothermal resources than is the case for oil and gas, but micro drilling could be useful for direct heat-exchange as well as for monitoring permeability at depth.

We are concerned that the underlying drilling technologies have been available for years, and in some cases for more than a decade; despite calls for applications to deep drilling (1000 m or more), there is as yet little field experience with micro drilling that is directly relevant to EGS. The hurdles do not appear to be technical, at this stage, so it is important to work at field scale in order to identify currently unanticipated technical problems that may arise.

At the same time, we recognize that advances in drilling technology could prove useful for oil and gas, so might not result in as significant a differential (economic) advantage for EGS than might at first be assumed. We do not see this as a disadvantage, however, and consider EGS-motivated advances in drilling technologies to offer promising opportunities for many elements of the U.S. Government.

6.2.2 Subsurface flow

Two aspects of subsurface flow that need to be characterized are the spatial heterogeneity of the flow paths, and how the flow at depth changes with time. The first is crucial to understanding recovery factors, which at present are thought to be largely determined by the presence of a few bypass paths dominating the flow (e.g., Grant and Garg, 2012) [22]. This is not a unique interpretation of available data, however, so it needs to be validated, and other effects potentially influencing recovery factors need further investigation.

Time-dependent monitoring is likewise essential for determining the phenomena controlling well-pair lifetimes, with possibly competing effects of new flow paths being formed while existing paths become clogged. The rates and patterns of clogging at depth relative to that occurring in pipes near and at the surface also need better documentation.

We have identified several technologies that show promise in addressing these issues. Downhole fiber-optic temperature measurement (along with remote observation by televiewing) can characterize flow paths near a borehole. Seismic, electromagnetic and chemical-tracer experiments can be used to image zones of permeability and fracture paths at greater distances: in principle, up to ranges spanning the separation between well-pairs.

These approaches are, in a few cases, proven in geothermal applications. In other cases, they are proven in other field applications, or else at laboratory scale. Overall, they need development and validation for EGS through application at field scale, with appropriate modeling that includes quantitative predictions that are then tested against measurements. Iteratively confronting simulation with observation can help in rapidly improving the thermal-hydrological-stress models of the subsurface.

6.3   Strategies: Scaling Up and Leveraging Success

The repeated theme in our consideration of technical advances is to develop and validate promising methods at field scale. Scaling up from laboratory experiments, or to prove methods in a different field application than has been the case to date, implies significant effort.

It is important to recognize, however, that initial experiments can be fruitfully pursued over relatively short distances – tens of meters rather than the hundreds or thousands of meters necessary for EGS production – for most if not all the technologies and procedures we have described. There is likely to be more control and better resolution at shorter scales, thereby increasing the

chances of really controlling the experiments and understanding the results. Because the cooling wave around a flow path extends less than 20-30 m, as we have emphasized, much can be learned across the shorter distances advocated here. As experience is gained, and flow paths are more predictably controlled (implying that they are adequately imaged and characterized as functions of space and time), the distances can be extended to production-scale.

These considerations suggest that it may not be so fruitful to conduct the necessary field-scale research at a production site. That is, the initial studies required for scaling would require additional drilling and infrastructure, beyond that used for production, due to being performed across smaller distances. There is clearly a tradeoff between benefitting from existing infrastructure versus being constrained in the research that can be effectively carried out at a production site.

To the degree that stand-alone field experiments are pursed, it may be beneficial to consider existing subsurface laboratories already established in the U.S. and elsewhere around the world, as some of these are at depths directly relevant to EGS (Figure 6-1). We note the value of conducting field-scale experiments at several different sites in order to quantify the influences of different geological materials (rock types, structures), stress and temperature regimes, and local hydrologic properties on the measurements.

Figure 1: Underground laboratories worldwide. Physics laboratories (blue) are listed with their depths in meters water equivalent. Laboratories for research into the long-term (~million-year) isolation of high-level nuclear waste, shown in red, are listed with actual depth. The NELSAM laboratory (black) is for earthquake research.

1 Homestake
Depth, m.w.e.: 4160

2 Soudan
Depth, m.w.e.: 2040

3 WIPP
Depth, m.w.e.: 1580

4 SNOLAB
Depth, m.w.e.: 5990

5 Baksan
Depth, m.w.e.: 4700

6 Gran Sasso
Depth, m.w.e.: 3030

7 Canfranc
Depth, m.w.e.: 2450

8 Fréjus/Modane
Depth, m.w.e.: 4150

9 Boulby
Depth, m.w.e.: 2805

10 Kamioka
Depth, m.w.e.: 2050

11 Mol
Rock Type: Clay
Depth: 230 m

12 Bure
Rock Type: Clay
Depth: 450 m

13 Tournemire
Rock Type: Clay
Depth: 300 m

14 Horonobe
Rock Type: Sedimentary
Depth: 1,000 m

15 Tono (Mizunami)
Rock Type: Granite
Depth: 1,000 m

16 Äspö.
Rock Type: Granite
Depth: 450 m

17 Mont Terri
Rock Type: Clay
Depth: 300 m

18 Grimsel
Rock Type: Granite
Depth: 450 m

19 Yucca Mountian
Rock Type: Volcanic tuff
Depth: 300 m

20 Pinawa
Rock Type: Granite
Depth: 450 m

21 NELSAM
Rock Type: Quartzite
Depth: 3,800 m

Figure 6-1: Locations of laboratories for subsurface research, many at depths relevant to EGS [from D. Elsworth briefing, 2013].

References

[1] C. F. Williams, M. J. Reed and R. H. Mariner, *A review of methods applied by the U.S. Geological Survey in the assessment of identified geothermal resources.* Open-file report 2008-1296 (2008).

[2] R. Emmermann and J. Lauterjung, *The German Continental Deep Drilling Program KTB: Overview and major results,* J. Geophys. Res., **102**, 18179-18201 (1997).

[3] H. J. Frost and M. F. Ashby, *Deformation Mechanism Maps,* Pergamon, New York, 166 pp. (1982).

[4] C. Augustine, *Updated U.S. Geothermal Supply Characterization and Representation for Market Penetration Model Input,* NREL/TP-6A20-47459, 89 pp. (2011).

[5] C. F. Williams, M. J. Reed, R. H. Mariner, J. DeAngelo, S. P. Galanis, Jr., *Assessment of Moderate- and High-Temperature Geothermal Resources of the United States,* U.S. Geological Survey Fact Sheet 2008-3082 (2008).

[6] AEO2013, *Annual Energy Outlook 2013 with Projections to 2040,* DOE/EIA-0383, U.S. Department of Energy, Washington, DC, 233 pp. (2013).

[7] J. W. Tester, B. J. Anderson, D. D. Blackwell, R. DiPippo, E. M. Drake, J. Garnish, B. Livesay, M. C. Moore, K. Nichols, S. Petty, M. N. Toksoz and R. W. Veatch, Jr., *The Future of Geothermal Energy, Impact of Enhanced Geothermal Systems (EGS) on the United States in the 21st Century,* INEL/EXT-06-11746, MIT/DOE (2006).

[8] J. Ziagos, B. R. Phillips, L. Boyd, A. Jelacic, G. Stillman and E. Hass, *A technology roadmap for strategic development of enhanced geothermal systems,* Proc. 38th Workshop on Geothermal Reservoir Engineering, SGP-TR-198, Stanford, CA (2013).

[9] D. L. Turcotte and G. Schubert, *Geodynamics*, Wiley, New York, 450 pp. (1982).

[10] K. P. Furlong and D. S. Chapman, *Heat flow, heat generation and the thermal state of the lithosphere*, Ann. Rev. Earth Planet. Sci., **41**, in press (2013).

[11] E. Stolper, D. Walker, B. H. Hager and J. F. Hays, *Melt segregation from partially molten source regions: The importance of melt density and source region sice*, J. Geophys. Res., **86**, 6261-6271 (1981).

[12] R. Jeanloz and S. Morris, *Temperature distribution in the crust and mantle*, Ann. Rev. Earth Planet. Sci., **14**, 377-415 (1986).

[13] T. Atwater, *Implications of plate tectonics for the Cenozoic tectonic evolution of Western North America*, Geol. Soc. Am. Bull., **81**, 3513-3536 (1970).

[14] C. Lithgow-Bertelloni and M. A. Richards, *The dynamics of Cenozoic and Mesozoic plate motions*, Rev. Geophys., **36**, 27-78 (1998).

[15] A. Banerjee, M. Person, A. Hofstra, D. Sweetkind, D. Cohen, A. Sabin, J. Unruh, G. Zyvoloski, C. W. Gable, L. Crossey and K. Karlstrom, *Deep permeable fault-controlled helium transport and limited mantle flux in two extensional geothermal systems in the Great Basin*, United States, Geology, **39**, 195-198 (2011).

[16] C. Augustine, K. R. Young and A. Anderson, *Updated U.S. geothermal supply curve*, Stanford Geothermal Workshop, Conference Paper NREL/CP-6A2-47458, http://www.osti/gov/bridge, 16 pp. (2010).

[17] K. F. Beckers, M. Z. Lukawski, T. J. Reber, B. J. Anderson, M. C. Moore and J. W. Tester, *Introducing GEOPHIRES VI.0: Software package; for estimating levelized cost of electricity and/or heat from enhanced; geothermal systems*, Proc. 38th Workshop on Geothermal Reservoir Engineering, SGP-TR-198, Stanford, CA (2013).

[18] E. C. Robertson, *Thermal Properties of Rocks*, U.S. Department of the Interior, Geological Survey (1988).

[19] T. J. Ahrens, ed., *A Handbook of Physical Properties*, AGU Reference Shelf, vols. 1-3, Am. Geophys. Union, Washington, DC; http://www.agu.org/books/rf/ ((1995)).

[20] C. Clauser, *Thermal storage and transport properties of rocks, I: Heat capacity and latent heat*, in Encyclopedia of Solid Earth Geophysics (H. K. Gupta, ed.), Springer, New York, 1423-1431 (2011a).

[21] C. Clauser, *Thermal storage and transport properties of rocks, II: Thermal conductivity and diffusivity*, in Encyclopedia of Solid Earth Geophysics (H. K. Gupta, ed.), Springer, New York, 1431-1448 (2011b).

[22] M. A. Grant and S. K. Garg, *Recovery factor for EGS* Thirty-Seventh Workshop on Geothermal Reservoir Engineering (Stanford U., Stanford, Cal. 2012) SGP-TR-194 (2012).

[23] U.S. Department of Energy (DOE), *Federal Interagency Geothermal Activities* updated 2011, Office of Energy Efficiency and Renewable Energy, Geothermal Technologies Program, http://www1.eere.energy.gov/geothermal/pdfs/ngap.pdf, 38 pp. (2010).

[24] C. Harto, J. Schroeder, L. Martino, R. Horner and C. Clark, *Geothermal energy: The energy-water nexus*, Proc. 38th Workshop on Geothermal Reservoir Engineering, SGP-TR-198, Stanford, CA (2013).

[25] R. Snieder, S. Hubbard, M. Haney, G. Bawden, P. Hatchell, A. Revil and DOE Geophysical *Monitoring Working Group, Advanced noninvasive geophysical monitoring techniques*, Ann. Rev. Earth. Planet. Sci., 35, 653-683 (2007).

[26] R. Snieder and K. Wapenaar, *Imaging with ambient noise*, Phys. Today, 63, 44-49 (2010).

[27] R. Snieder and E. Larose, *Extracting Earth's elastic wave response from noise measurements*, Ann. Rev. Earth Planet. Sci., **41**, 183-206 (2013).

[28] D. Draganov, K. Wapenaar, W. Mulder, J. Singer and A. Verdel, *Retrieval of reflections from seismic background-noise measurements*, Geophys. Res. Lett., **34**, L04305 (2007).

[29] D. Draganov, X. Campman, J. Thorbecke, A. Verdel and K. Wapenaar, *Reflection images from ambient seismic noise*, Geophysics, 74, A63-A67 (2009).

[30] I. M. Tibuleac and M. Eneva, *Seismic signature of the geothermal field at Soda Lake, Nevada, from ambient noise analysis*, Geothermal Resources Council Trans., **35**, 1767-1771 (2011).

[31] I. Vasconcelos, R. Snieder and P. Sava, *Drill bit noise illuminates San Andreas Fault*, EOS, Trans. AGU, **89**, 349 (2008).

[32] S. A. L. deRidder and B. L. Biondi, *Daily reservoir-scale subsurface monitoring using ambient seismic noise*, Geophys. Res. Lett., in press (2013).

[33] P. A. Johnson, T. J. Shankland, R. J. O'Connell and J. N. Albright, *Nonlinear generation of elastic waves in crystalline rock*, J. Geophys. Res., **92**, 3597-3602 (1987).

[34] P. A. Johnson and T. J. Shankland, *Nonlinear generation of elastic waves in granite and sandstone: Continuous wave and travel time observations*, J. Geophys. Res., **94**, 17729-17733 (1989).

[35] R. A. Guyer and P. A. Johnson, *Nonlinear mesoscopic elasticity: Evidence for a new class of materials*, Phys. Today, **52**, 30-36 (1999).

[36] D. Pasqualini, K. Heitmann, J. A. TenCate, S. Habib, D. Higdon and P. A. Johnson, *Nonequilibrium and nonlinear dynamics in Berea and Fontainebleau sandstones: Low-strain regime*, J. Geophys. Res., **112**, 10.1029/2006JB004264 (2007).

[37] V. V. Kazakov, A. Sutin and P. A. Johnson, *Sensitive imaging of an elastic nonlinear wave-scattering source in a solid*, Appl. Phys. Lett., **81**, 646-648 (2002).

[38] T. J. Ulrich, A. M. Sutin, R. A. Guyer and P. A. Johnson, *Time reversal and non-linear elastic wave spectroscopy (TR NEWS) techniques*, Int. J. Non-Linear Mech., **43**, 209-216 (2008).

[39] Y. Ohara, K. Takahahsi, S. Murai and K. Yamanaka, *High-selectivity imaging of closed cracks using elastic waves with thermal stress induced by global preheating and local cooling*, App. Phys. Lett., **103**, 031917 (2013).

[40] T. U. Clausthal, *A comprehensive review of past and present drilling methods with application to deep geothermal environment*, Thirty-Sixth Workshop on Geothermal Reservoir Engineering Stanford University, Stanford, California, January 31 - February 2, 2011 SGP-TR-191

[41] W. C. Maurer, *Advanced Drilling Techniques* (Petroleum Publishing, Tulsa) (1980).

[42] Schlumberger, *New HTHP technology for geothermal application significantly increases on-bottom drilling hours*; http://www.slb.com/resources/technical_papers/smith/drill_bits/150030.aspx (2013).

[43] Sandia, *Polycrystalline diamond drill bits open up options for geothermal energy*; https://share.sandia.gov /news/resources/news_releases /pdcs_geothermal/#.Ue1yaKWKzww (2012).

[44] Y. Nakamoto et al., *High-pressure generation using nano-poycrystaline diamonds as anvil materials*, Rev. Sci. Instrum., *82*, 066104 (2011).

[45] Q. Liang et al., *Enhancing the mechanical properties of CVD single-crystal diamond*, J. Phys. Cond. Matt., **21**, 364215 (2009).

[46] Y. Lu, J. Tang, Z. Ge, B. Xia and Y. Liu, *Hard rock drilling technique with abrasive water jet assistance*, Int. J. Rock Mech. Min. Sci., *60*, 47-56 (2013).

[47] E. Majer, private communication (2013).

[48] R. Long, *DOE's Microhole Technologies Program overview*, May 2-5 (2005).

[49] R. Long, *Microhole technologies and deep slimhole drilling*, paper presented at ARMA Drilling Technology Forum, September 14 (2007).

[50] P. A. Lucon, *Resonance: The Science Behind the Art of Sonic Drilling*, Ph.D. Thesis, Montana State University (2013).

[51] J. J. Kolle, *A comparison of water jet, abrasive jet and rotary diamond drilling in hard rock*, Tempress Technologies Inc. (1999).

[52] J. J. Kolle, *The effects of pressure and rotary speed on the drag bit drilling strength of deep formations*, paper presented at SPE Annual Technical Conference and Exhibition, Denver, CO, October 6-9 (1996).

[53] C. Able, private communication (2013).

[54] P. A. Witherspoon, J. S. Y. Wang, K. Iwai and J. E. Gale, *Validity of cubic law for fluid flow in a deformable rock fracture.* Water Resources Research, **16**, 1016-1024 (1980).

[55] G. Axelsson, G. Bjornsson, O. G. Flóvenz, H. Kristmannsddttir, H., and G. Sverrisdóttir, *Injection experiments in low-temperature geothermal areas in Iceland*, Proc. World Geothermal Congress Florence, Italy 1991-1996 (1995).

[56] G. Axelsson, G. Björnsson and F. Montalvo, *Quantitative interpretation of tracer test data*, Proc. World Geothermal Congress (2005).

[57] M. D. Williams P. W. Reimus, V. R. Vermeul, P. E. Rose, C. A. Dean, T. B. Watson, D. L. Newell, K. B. Leecaster and E. M. Brauser, *Development of models to simulate tracer tests for characterization of enhanced geothermal systems.* Pacific Northwest National Laboratory, PNNL-22486 (2013).

[58] I. Kocabas and R. N. Horne, *Analysis of injection-backflow tracer tests in fractured geothermal reservoirs.* Twelfth Workshop on Geothermal Reservoir Engineering (Stanford U., Stanford, Cal. 1987) (1987).

[59] I. Kocabas, *Geothermal reservoir characterization via thermal injection backflow and interwell tracer testing.* Geothermics, **34**, 27-46 (2005).

[60] M. Sahimi, Rev. Mod. Phys. **65**, 1393-1534 (1993).

[61] R. F. Probstein, *Physicochemical Hydrodynamics* (John Wiley & Sons, Inc., New York, 1994).

[62] P. Rose, *et al. A tracer test at the Soda Lake, Nevada geothermal field using a sorbing tracer.* Thirty-Seventh Workshop on Geothermal Reservoir Engineering (Stanford U., Stanford, Cal. 2012) SGP-TR-194.

[63] P. E. Rose and M. C. Adams, *The application of rhodamine WT as a geothermal tracer.* Geothermal Resources Council TRANSACTIONS **18**, 237–240 (1994).

[64] P. Reimus, *et al. Use of tracers to interrogate fracture surface area in single-well tracer tests in EGS systems.* Thirty-Seventh Workshop on Geothermal Reservoir Engineering (Stanford U., Stanford, Cal. 2012) SGP-TR-194.

[65] P. Reimus, email to J. Katz July 24, 2013.

[66] P. Rose, email to J. Katz July 25, 2013.

[67] R. Jung, *EGS — Goodbye or Back to the Future*, Chap. 5 pp. 95–121 `http://dx.doi.org/10.5772/56458` (2013).

[68] E. Charlaix, J. P. Hulin, C. Leroy and C. Zarcone, *Experimental study of tracer dispersion in flow through two-dimensional networks of etched capillaries*, J. Phys. D: Appl. Phys. **21**, 1727-1732 (1988).

[69] J. Geiermann and E. Schill, *2-D magnetotellurics at the geothermal site at Soultz-sous-Forets: Resistivity distribution to about 3000 m depth*, C. R. Geoscience, **342**, 587-599 (2010).

[70] R. Streich, M. Becken and O. Ritter, *Imaging of CO2 storage sites, geothermal reservoirs, and gas shales using controlled-source magnetotellurics: Modeling studies*, Chem. Erde, **70**, 63-75 (2010).

[71] C. Dorn, N. Linde, J. Doetsch, T. Le Borgne and O. Bour, *Fracture imaging within a granitic rock aquifer using multiple-offset single-hole and cross-hole GPR reflection data*, J. Appl. Geophys., **78**, 123-132 (2012).

[72] S. Onacha, D. Kahn, P. Malin and E. Shalev, *Resistivity and microearthquake imaging of Krafla Geothermal Field*, NE Iceland, Geotherm. Resources Council, **29**, 497-502 (2005).

[73] G. Munoz, O. Ritter and I. Moeck, *A target-oriented magnetotelluric inversion approach for characterizing the low enthalpy Gross Schnebeck geothermal reservoir*, Geophys. J. Int., **183**, 1199-1215 (2010).

[74] P. Jousset, C. Haberland, K. Bauer and K. Arnason, *Hengill geothermal volcanic complex (Iceland) characterized by integrated geophysical observations*, Geothermics, **40**, 1-24 (2011).

[75] A. M. Wamala, K. L. Mickus, L. F. Serpa and D. I. Doser, *A joint geophysical analysis of the Coso geothermal field, south-eastern California*, Phys. Earth Planet Int., **214**, 25-34 (2013).

[76] M. Moorkamp, B. Heincke, M. Jegen, A. W. Roberts and R. W. Hobbs, *A framework for 3-D joint inversion of MT, gravity and seismic refraction data*, Geophys. J. Int., **184**, 477-493 (2011).

[77] M. Moorkamp, A. W. Roberts, M. Jegen, B. Heincke and R. W. Hobbs, *Verification of velocity-resistivity relationships derived from structural joint inversion with borehole data*, Geophys. Res. Lett., **40**, 3596-3601 (2013).

[78] J. R. Peacock, S. Thiel, P. Reid and G. Heinson, *Magnetotelluric monitoring of an enhanced geothermal system fluid injection: Example from an enhanced geothermal system*, Geophys. Res. Lett., **39**, L18403 (2012).

[79] J. R. Peacock, S. Thiel, G. S. Heinson and P. Reid, *Time-lapse magnetoitelluric monitoring of an enhanced geothermal system*, Geophysics, **78**, B120-B130 (2013).

[80] M. Karaoulis, A. Revil, J. Zhang and D. Werkema, *Time-lapse joint inversion of cross-well DC resistivity and seismic data: A numerical investigation, preprint* (2013).
http://cfpub.epa.gov/si/si_public_record_report.cfm?dirEntryId=250575

[81] J. Doetsch, N. Linde and A. Binley, *Structural joint inversion of time-lapse crosshole ERT and GPR traveltime data*, Geophys. Res. Lett., **37**, L24404 (2010).

[82] G. S. Bodvarsson and C. F. Tsang, *Injection and thermal breakthrough in fractured geothermal reservoirs.* J. Geophys. Res. **87**, 1031-1048 (1982).

[83] A. C. Gringarten, P. A. Witherspoon and Y. Ohnishi, *Theory of heat extraction from fractured hot dry rock.* J. Geophys. Res. **80**, 1120-1124 (1975).

[84] H. A. Lauwerier, *The transport of heat in an oil layer caused by the injection of hot fluid.* Appl. Sci. Res. **5**, 145 (1955).

[85] T. Reilly, K. Dennehy, W. Alley and W. Cunningham, *Ground-water availability in the United States*, Circular 123, Dept. of the Interior, U.S. Geological Survey (2008).

[86] A. Y. Ku and A. P. Shapiro, *The energy-water nexus: Water use trends in sustainable energy and opportunities for materials research and development*, MRS Bull., **37**, 439-

[87] J. Macknick, R. Newmark, G. Heath and K. C. Hallett, *A Review of Operational Water Consumption and Withdrawal Factors for Electricity Generating Technologies*, NREL/TP-6A20-50500, 22 pp. (2011).

[88] *Geothermal task force report*, Tech. rep., Western Governor's Association (2006).

[89] M. J. Rutberg, *Modeling water use at thermoelectric power plants* Master of Science dissertation, Massachusetts Institute of Technology, Retrieved July 2013 from http://dspace.mit.edu/bitstream/handle/1721.1/74674 /815966188.pdf?sequence=1, (2012).

[90] M. J. Rutberg, A. Delgado, H. Herzog and F. F. Ghoniem, *A system-level generic model of water use at power plants and its application to regional water use estimation and technology evaluation*, IMECE2011-63786, ASME 2011 IMECE, Nov 11-17, 2011, Denver, CO.

[91] R. Pate, M. Hightower, C. Cameron, & W. Einfeld, *Overview of energy-water interdependencies and the emerging energy demands on water resources*. SANDIA 2007-1349C, (2007).

[92] E. A. DeMeo, *Renewal Energy Technology Characterizations*, EPRI Report # TR-109496 (1997).

[93] A. Kagel, D. Bates, and K. Gawell (2007), A guide to geothermal energy and the environment, Tech. rep., Geothermal Energy Assoc., 209 Pennsylvania Ave. SE, Washington, D.C., (2003).

[94] T. Reilly, K. Dennehy, W. Alley, and W. Cunningham, *Ground-water availability in the United States*, Circular 123, Dept. of the Interior, U.S. Geological Survey (2008).

[95] National Research Council (NRC), *Induced Seismicity Potential in Energy Technologies*, National Academies Press, Washington, DC, 300 pp. (2012).

[96] W. L. Ellsworth, *Injection-induced earthquakes*, Science, 341, 1225942 (2013).

[97] B. R. Julian, G. R. Foulger, F. C. Monastero and S. Bjornstad, *Imaging hydraulic fractures in a geothermal reservoir*, Geophys. Res. Lett., **37**, L07305 (2010).

[98] S. A. Flewelling, M. P. Tymchak and N. Warpinsky, *Hydraulic fracture height limits and fault interactions in tight oil and gas formations*, Geophys. Res. Lett., **40**, 3602-3606 (2013).

[99] E. E. Brodsky and L. J. Lajoie, *Anthropogenic seismicity rates and operational parameters at the Salton Sea Geothermal Field*, Science, **341**, 1239213 (2013).

[100] B. Mena, S. Wiemer and C. Bachmann, *Building robust models to forecast induced seismicity related to geothermal reservoir enhamcement*, Bull. Seismol. Soc. Am., **103**, 383-393 (2013).

[101] F. Catalli, M.-A. Meier and S. Wiemer, *The role of Coulomb stress changes for injection-induced seismicity: The Basel enhanced geothermal system*, Geophys. Res. Lett., **40**, 72-77 (2013).

[102] M. Manga, I. Beresnev, E. E. Brodsky, J. E. Elkhoury, D. Elsworth, S. E. Ingebritsen, D. C. Mays and C.-Y. Wang, *Changes in permeability caused by transient stresses: Field observations, experiments, and mechanisms*, Rev. Geophys., **50**, 2011RG000382 (2012).

[103] N. J. van der Elst, H. M. Savage, K. M. Keranen and G. A. Abers, *Enhanced remote earthquake triggering at fluid-injection sites in the Mid-Western United States*, Science, **341**, 164-167.

[104] C. Y. Wang, L. P. Wang, M. Manga, C. H. *Wang and C. H. Chen, Basin-scale transport of heat and fluid induced by earthquakes*, Geophys. Res. Lett., **40**, 10.1002/grl.50738 (2013).

[105] P. G. Meredith, I. G. Main, O. C. Clint and L. Li, *On the threshold of flow in a tight natural rock*, Geophys. Res. Lett., **39**, L04307 (2012).

[106] JASON, *Characterization of Underground Facilities*, JSR-97-155, MITRE Corp., McLean, VA, 67 pp. (1999).

[107] National Research Council, *Effects of Nuclear Earth-Penetrator and Other Weapons*, National Academies Press, Washington, DC, 146 pp. (2005).

A APPENDIX: CRACKS AND TRACERS

A.1 Some Characteristic Crack Parameters

If crack openings are too wide fluid flows rapidly through them without being heated close to the rock temperature. Even if energy is extracted, the Carnot efficiency is low. If the apertures are too narrow, their low hydrodynamic admittance (high viscous resistance) requires more hydrodynamic work and a higher pressure drop between injection and production wells in order to extract the desired power (implicit in our assumption of a characteristic time scale of energy extraction, which in turn is determined by economic considerations of return on investment).

We first determine a characteristic width[3] b_0 of a crack in EGS, defined as the width of cracks (there must be many of them) that draw heat (approximately) uniformly from the entire volume penetrated by cracks. We note that the actual crack widths need not be equal, or even comparable, to b_0 (though we later show they must not exceed b_0 for efficient generation of geothermal power); b_0 only defines a physical scale. This characteristic width is a function of the parameters of the resource. We consider cracks of width b, length (between injection and production wells) ℓ, and transverse (spanwise) dimension h (that does not enter); typically we take $h = \ell$.

Assume a system age $t_r = 10$ y, thermal diffusion coefficient $D_r = 0.008$ cm^2/s in granite (the lower end of a range of two found on the Web, to allow for microcracks, *etc.*), volumetric specific heats of granite $C_r = 2.5$ J/cm^{3}K and of water $C_w = 4.2$ J/cm^{3}K, pressure drop $\Delta P = 100$ bar, viscosity of water at a mean temperature of $100\,°$C $\eta = 0.0028$ g/cm-s, and a crack length $\ell = 10^5$ cm. To heat the water efficiently in a crack of width b we equate the heat (per unit area) carried by the water as it is heated by an amount ΔT_w

---

[3]By "width" of a crack we mean the distance separating its two surfaces, generally quite small.

over a length ℓ

$$\frac{\Delta T_w C_w v b}{\ell},\tag{A-1}$$

where v is the mean flow speed, to the conductive heat flow out of the rock, allowing for two surfaces of a planar crack,

$$2\frac{\kappa_r \Delta T_r}{\ell_T},\tag{A-2}$$

where ΔT_r is the temperature drop between the deep rock and the water and thermal conduction sets the minimum scale $\ell_T = \sqrt{D_r t_r} \approx 16$ m of temperature gradients in the rock. Cracks spaced closer than $\mathcal{O}(2\ell_T)$ effectively draw on the same thermal resource, although their hydrodynamic admittances add, reducing the pressure drop and mechanical work required to extract the same amount of heat.

For efficient operation we desire $\Delta T_r \ll \Delta T_w$, equivalent to requiring that the water be heated to a temperature close to the temperature of the rock far from the cooling flow. Writing, for viscous flow in a duct, the mean speed

$$v = \frac{\Delta P}{\ell}\frac{b^2}{12\eta},\tag{A-3}$$

we find

$$b < b_0 \equiv \left(\frac{C_r}{C_w}\sqrt{\frac{D_r}{t_r}}\frac{24\ell^2\eta}{\Delta P}\right)^{1/3}.\tag{A-4}$$

Inserting the numbers above, $b_0 = 0.027$ cm and the corresponding $v_0 = 22$ cm/s. Water flowing in a wider crack heats but does not approach the distant rock temperature. Although it removes thermal energy effectively from the rock, its lower temperature reduces the thermodynamic efficiency of electric power generation.

The characteristic Reynolds number

$$\mathrm{Re}_0 = \frac{3\rho v_0 b_0}{4\eta} = \frac{\rho b_0^3 \Delta P}{16\eta^2\ell} \approx 160,\tag{A-5}$$

where the factor of 3/4 comes from using the central (peak) velocity $3v_0/2$ and $b_0/2$ as the length scale, in analogy to the use of the radius to define

the Reynolds number in circular pipe flow. The flow in a crack thin enough for the fluid to approach the distant rock temperature is laminar, but Re may be $\gg 1$. The parameters b_0, v_0 and Re_0 depend on ΔP, which is under our control. However, reducing ΔP in order to maintain $\Delta T_r \ll \Delta T_w$ may reduce the flow rate to uneconomic levels as it increases the temperature of the produced hot water, decreasing the power produced; it is no panacea for a poorly fractured resource.

If parametrized in terms of volumetric flow rate Q, taking the span of the crack $h \approx \ell$, the same as its length, the crack width drops out. The result is a condition on the flow rate Q in a single crack:

$$Q < Q_0 \equiv 2\frac{C_r}{C_w}\sqrt{\frac{D_r}{t_r}}\ell^2 \approx 60 \left(\frac{\ell}{1\,\mathrm{km}}\right)^2 \mathrm{l/s}. \tag{A-6}$$

This is comparable to the flow rates of entire EGS systems. If cracks have widths $b \approx b_0$ only one or a few may be contributing significantly to the fluid flow. A total flow rate $\lesssim Q_0$ implies that the temperature of the (initially) produced hot water is close to T_r, as observed. Were there only one contributing crack, it would be predicted that increasing the flow rate above Q_0 would immediately reduce the temperature of the produced water (Section A.1.1). Were there many contributing cracks, the temperature would not immediately be reduced, and the condition (A-4) for efficient use of thermal energy need not be violated. The dependence of produced water temperature on forced flow rate is a possible test for the number of significantly contributing cracks.

A.1.1 Thermal bypass type I

For efficient generation of electricity from geothermal energy we require $b < b_0$ and $v < v_0$. A single wide crack ($b > b_0$) through which a large quantity of water flows ($Q > Q_0$) without being adequately heated is sufficient to reduce the efficiency of an entire EGS system when the cooler water mixes with hot water in the production well. Narrower cracks with $b \ll b_0$ and $v \ll v_0$ may tap the geothermal energy efficiently, producing water at nearly

the temperature of the rock at the crack, but require more pumping power and pressure drop to overcome viscous drag (hydrodynamic impedance), as discussed in Section A.8. We are likely to have only the crudest control, if any, over the parameters of stimulated fractures.

The temperature of water within cracks wider than b_0 does not approach T_r because it flows too fast for sufficient heat to be conducted through the rock to the flowing water (the water itself is isothermal across the narrow crack). Such wide cracks are a source of thermal bypass, mixing their cooler water with hot water from narrower cracks at the production well. This is the first, and most lethal, class of thermal bypass. Because b_0 depends on both the pressure gradient and on the time t_r over which geothermal energy has been pumped, bypass will develop gradually, and may (at the price of reducing the fluid and heat flow rate) be controlled by reducing the pressure gradient. A second class of thermal bypass, resulting from heterogeneous depletion of rock thermal energy, can occur even for cracks narrower than b_0, and is discussed in Section A.5.1.

A.1.2 Stenoses and aneurisms

Suppose b varies along the length of a crack, so that there are constrictions (stenoses) and enlargements (aneurisms). Conservation of mass implies that bv is constant along a two-dimensional (parameters are independent of the direction transverse to the flow) crack. Hence if the condition (A-4) for $\Delta T_r \ll \Delta T_w$ is met at one place along the crack it will be met everywhere; enlargements do not lead to thermal bypass type I. Their effect is to make the pressure gradient vary along the flow direction, larger in constrictions and smaller in enlargements. Similarly, the Reynolds number is constant along the crack.

Constrictions and enlargements redistribute the pressure drop between injection and production wells. In cracks that are not two-dimensional pressure relaxation transverse to the flow redistributes streamlines away from

104

constrictions whose width varies in the transverse (spanwise) dimension. The mass flow (areal density of streamlines) then varies $\propto b^3$. Stenoses and aneurisms affect the paths of streamlines, their admittances and the distribution of flow times. These are also affected by other factors (such as the distribution of crack widths), and it is not possible to infer anything about stenoses and aneurisms from flow time data.

A.2 Data from Soda Lake

We can obtain some numerical estimates of the properties of an actual dry rock geothermal resource from a tracer experiment at Soda Lake [2, 3]. In this experiment the injection and production wells were 550 m apart and the pressure differential, provided by a 1360$'$ pressure head and an additional 110 psi on the injection well, was 48 bars, for a pressure gradient of 880 dyne/cm^3 [4].

A conservative (non-degrading, non-sorbing) tracer (1,6-naphthalene disulfonate according to [2]; 1,5-naphthalene disulfonate according to [3]) was injected. Injection continued over five hours [5], a short enough time that it may be considered instantaneous. The rate of fluid injection was 800 gpm (50 l/s), corresponding to a hydrodynamic admittance $A = 1.0$ l/s-bar $= 10$ l/s-MPa.

Tracer was first observed at the production well about 15 hours after injection, and its concentration rose to about $1/e$ of its maximum value after about 50 hours after injection. Using this latter value to estimate the fluid velocity in a nominal crack, we find $v = 0.3$ cm/sec (diffusion rapidly homogenizes the fluid across the width of a crack). This is much less than the characteristic v_0 defined in Section A.1, and $b = 0.0034\,\mathrm{cm} \ll b_0$. The Reynolds number Re ≈ 0.3.

The flow rate in such a crack $Q = 0.06$ l/s. This is only 10^{-3} of the injected flow rate (50 l/s), which is consistent with $\mathcal{O}(1000)$ comparable

105

cracks contributing to the flow. The fact that tracer is first detected after about 15 hours implies that there are some cracks in which v is about three times greater, and b about twice as large, but the fact that at this early time the tracer concentration is only about 10^{-3} of its peak value implies that very little mass flows through these larger cracks. Even their widths are still much less than b_0, and they do not contribute to thermal bypass of Type I.

If there are $\mathcal{O}(1000)$ cracks in a resource of size $\mathcal{O}(0.5\,\mathrm{km})$, the typical distance between cracks is $\mathcal{O}(0.5\,\mathrm{m}) \ll \ell_T$ for $t_r \gg 1$ week. On any time scale relevant to extracting energy (but not necessarily in a brief experiment), if the cracks are identical and distributed uniformly the rock temperature will vary little in directions perpendicular to the fluid flow and (provided $b \ll b_0$, as inferred) the produced water temperature T_w will be very close to T_r.

A.2.1   Tracer diffusion

The Schmidt number $\mathrm{Sc} \equiv \eta/(\rho D_m)$, where D_m is the diffusivity of some solute. For solutes of low molecular weight (simple ions or small molecules) in water $\mathrm{Sc} \approx 300$ at room temperature but probably $\mathrm{Sc} \approx 30$ at $100\,^{\circ}\mathrm{C}$[4]. Solutes diffuse much more slowly than momentum.

Diffusion homogenizes the composition across a crack in a distance along the crack

$$L_D \approx \frac{vb^2}{D_m} = \frac{b^4 \Delta P}{24 \eta D_m \ell} \approx 200 \left(\frac{b}{b_0}\right)^4 \mathrm{cm}. \qquad \text{(A-7)}$$

This homogenization distance may be related to the corresponding viscous coupling distance

$$L_\eta \approx \frac{\rho v b^2}{\eta} \approx \frac{L_D}{\mathrm{Sc}} \approx b\,\mathrm{Re} \approx 7 \left(\frac{b}{b_0}\right)^4 \mathrm{cm}. \qquad \text{(A-8)}$$

The Taylor effective longitudinal diffusivity that results from the variation of velocity across the width of the crack as long-range longitudinal

---

[4]Values of D_m are generally only available at room temperature, but it is expected that their temperature dependence is reciprocal to that of η because intermolecular forces increase viscosity but reduce diffusivity.

heterogeneity becomes short-range transverse heterogeneity that is rapidly mixed by molecular diffusivity

$$D_{long} = C_{long} \frac{v^2 b^2}{D_m} = C_{long} \frac{b^6}{576\eta^2} \left(\frac{\Delta P}{\ell} \right)^2 \approx 4 \times 10^4 C_{long} \left(\frac{b}{b_0} \right)^6 \text{ cm}^2/\text{s,}$$

$$\text{(A-9)}$$

where C_{long} is a dimensionless constant $\approx 1/210$. This effective diffusivity is only meaningful over the distances $\gtrsim L_D$ over which transverse diffusion is effective, and has the peculiar property of being meaningful only when combined with advection, in that it describes diffusion about a mean advective motion.

For the flow parameters estimated for the Soda Lake experiment, $D_{long} \approx 10^{-4} \text{ cm}^2/\text{s}$, much larger than the nominal molecular $D_m = 10^{-5} \text{ cm}^2/\text{s}$, but too small to give significant diffusion. The measured time scale $\approx 10^6$ s for the decay of the tracer concentration at the production well after its peak corresponds to an effective diffusivity $\mathcal{O}(3 \times 10^3 \text{ cm}^2/\text{s})$.

A.3   Streamlines

The flow in the resource, though not in the injection and production wells, is laminar (Eq. A-5 shows that were the Reynolds number high enough to be turbulent, bypass would reduce the production temperature to nearly the injection temperature). It is useful to think about its streamlines. Fluid elements follow constant streamlines once they enter the laminar flow region near the injection well, and remain on them until they reach the turbulent flow region at the production well. Because viscosity is important, Bernoulli's equation is not applicable. The flow need not be stationary, and will not be stationary if ΔP varies, but the streamlines will not change as all velocities vary in proportion (the necessary condition for this is only that the flow not vary on the viscous diffusion time $\rho b^2/\eta$ or length $\rho b^2 v/\eta = \rho b^4 \Delta P \eta^2 \ell$, conditions that may be met even if Re $\gg$ 1).

In contrast to the more familiar case of two-dimensional flow, in which

mass conservation is described by $\vec{\nabla}_{x,y} \cdot \vec{v} = 0$, in a narrow crack in the x-y plane whose thickness $b(x,y)$ is a slowly varying function of (so that $\vec{v}$ is, to good approximation, in the x-y plane)

$$\vec{\nabla}_{x,y} \cdot (b\vec{v}) = 0. \tag{A-10}$$

Conventional velocity streamlines may have a non-zero divergence but cannot intersect unless b and v are zero.

The velocity is related to the pressure gradient by

$$\vec{v} = \frac{b^2}{12\eta} \vec{\nabla}_{x,y} P. \tag{A-11}$$

If b is constant, this reduces to the familiar Laplace equation $\nabla^2 P = 0$, with P taking the place of the velocity potential and $\vec{\nabla}_{x,y} \times \vec{v} = 0$, but for more general $b(x,y)$ the corresponding equation for P is

$$\vec{\nabla} \cdot \left(b^3 \vec{\nabla}_{x,y} P(x,y) \right) = 0. \tag{A-12}$$

The condition $\vec{\nabla} \times \vec{v} = 0$ implies that $\vec{\nabla}P$ is parallel (but not generally proportional) to $\vec{\nabla}b$.

The velocity is determined by the pressure gradient and the local crack width. Streamlines of $b\vec{v}$ separate in constrictions, where the crack narrows and the flow slows, and concentrate in wider regions, where the flow speeds. They bend around the asperities that hold the crack open. We expect these wide and long cracks to be highly multiply connected, with a very large number of asperities (possibly $\mathcal{O}(\ell^2/b^2)$).

Flow on each streamline is dynamically independent of that on other streamlines that are separated by a distance $\gtrsim b$. On these scales the dominant forces on the fluid are those of viscous interaction with the walls of the crack, not of more (than the very small distance b) distant streamlines. It is therefore useful to think of the flow, even through a crack that may have a span as great as its length, or that has a complex and highly multiply connected spatial structure, as composed of a large number of independent streamlines.

We define a flow admittance of a streamline per unit span of crack

$$\mathcal{A} \equiv \left(\int \frac{12\eta}{b^3} \, d\ell \right)^{-1}. \tag{A-13}$$

The admittance of an entire crack or system of cracks

$$A \equiv \frac{dV_f/dt}{dP/d\ell} = \int \mathcal{A}(y) \, dy, \tag{A-14}$$

where dV_f/dt is the volumetric fluid flow rate and the integral runs over the spanwise direction in the crack plane, adding the admittances of the individual streamlines. Along a streamline impedances add in series, but the various streamlines admit flow in parallel.

Two other scales should be considered. The advection of tracers (and any dissolved or suspended material) on a streamline is independent of that on other streamlines separated by more than the diffusion distance $\ell_D = \sqrt{D_m \ell / v} \approx \sqrt{12 D_m \eta \ell^2 / (\Delta P b^2)} \approx 20$ cm, where we have used the Soda Lake parameters from Section A.2 to obtain a numerical value, taking the molecular diffusivity $D_m = 10^{-5}$ cm^2/s. On transverse distance scales $\Delta y \lesssim \ell_D$ composition is homogenized. The problem becomes more complex if streamlines are braided, as may be the case if cracks are not topologically two-dimensional. Finally, the advection of heat (and the fluid temperature) are determined by conduction in the rock that homogenizes temperature over distances $\lesssim \ell_T$.

The flow impedance on a streamline

$$\mathcal{I} = 12\eta \int \frac{d\ell}{b^3} \tag{A-15}$$

and the fluid flow rate (per unit span of crack) $q = \Delta P / \mathcal{I}$. The transit time of a fluid element, or the arrival time of a tracer injected at $t = 0$ on that streamline, is

$$t_{transit} = \int \frac{d\ell}{v(\ell)} = 12\eta \int \frac{d\ell}{b^2 dP/d\ell}. \tag{A-16}$$

If b is constant along a stream line then $\mathcal{I} = 12\eta\ell/b^3$ and we recover the trivial result

$$t_{transit} = \frac{12\eta\ell^2}{b^2 \Delta P} = \frac{\ell b h}{Q}. \tag{A-17}$$

109

For a two-dimensional crack (a crack whose parameters are independent of the spanwise coordinate and whose flow is in the longitudinal direction, orthogonal to the spanwise direction) bv is conserved and $dP/d\ell = 12\eta Q/(hb^3)$. Then

$$t_{transit} = \frac{h}{Q} \int b \, d\ell;\tag{A-18}$$

the transit time is dominated by the widest regions of the crack. Eliminating Q, we find

$$t_{transit} = \frac{12\eta}{\Delta P} \int b \, d\ell \times \int b^{-3} \, d\ell.\tag{A-19}$$

Both expansions and constrictions increase the transit time, the former by reducing the velocity within them, and the latter by reducing the fluid flow rate. If the crack is not two-dimensional, $t_{transit}$ is still given by Eq. A-19, but the integrals must be taken over the actual path, which requires solution of Eq. A-12 for the pressure field.

If $dP/d\ell$ is constant along a streamline it can be moved outside the integral in Eq. A-16. The validity of this assumption is unproven, and it is possible to think of counterexamples. However, if pressure is communicated effectively transverse to the fluid flow it may be valid. This is likely to be a fair approximation in a wide crack, and a good approximation if the fluid flow region has small aspect ratio (small extent transverse to the flow direction in comparison to the length of the flow path).

A.4 Tracers

The motion of tracers is governed by the equation

$$\frac{\partial n}{\partial t} - D\nabla^2 n + \vec{\nabla} \cdot (\vec{v}n) = 0,\tag{A-20}$$

where $n(x,t)$ is the tracer density. The Green's function, describing the evolution of an instantaneous point injection of tracer, is the usual solution of the diffusion equation for an instantaneous point injection with x replaced by $x - vt$:

$$G(x,t) = \frac{1}{\sqrt{4\pi D_m t}} \exp - \left(\frac{(x - vt)^2}{4D_m t}\right).\tag{A-21}$$

H. Stone has pointed out that the distribution of arrival times of conservative tracer in the Soda Hill experiment [2, 3] is well fit by

$$f(t) \propto \frac{1}{\sqrt{4\pi t}} \exp - \left(\frac{(\ell - vt)^2}{4Dt} \right), \tag{A-22}$$

where the phenomenological diffusivity $D = 0.16$ m^2/sec $= 0.23 D_0$, $D_0 \equiv \ell v = 0.70$ m^2/s, $v = 1.26$ mm/s and $t_0 \equiv \ell/v = 5.0$ days characterizes (but is not equal to) the arrival time of the peak tracer concentration. This distribution is essentially identical to the Green's function Eq. A-21 for diffusing conservative passive tracers. It is shown in Figure A-1 for several values of D/D_0. The corresponding numbers for the Steamboat Hills experiment [6] are $\ell = 650$ m, $D = 0.027$ m^2/s, $D/D_0 = 0.41$ and $v = 0.06$ mm/s; peak breakthrough occurred after about 80 days, in comparison to four days at Rose Hill.

As discussed in Section A.2.1, the diffusivity of the tracers, even when enhanced by shear in the flow (Taylor's effective diffusivity of pipe or duct flow), is insufficient to explain the dispersion of tracer arrival times. The diffusivity D fitted to the data should not be regarded as a physical diffusivity, but rather as an empirical parameter describing the dispersion in the streamline flow times.

A.5 Cooling Fronts

If $\Delta T_r \ll \Delta T_w$ the water temperature approaches the distant rock temperature in a time short compared to that required to flow through the length of the crack. As a result, there is a distinct front between the region in which water has cooled the rock to its injection temperature, a narrow transition region, and a region in which the water has been heated to the initial rock temperature. Most of the heat transfer from rock to water occurs in this transition region.

Fluid in cracks with width $b \ll b_0$, such as we infer from the tracer data from the Soda Lake experiment, will always be close to the temperature of

111
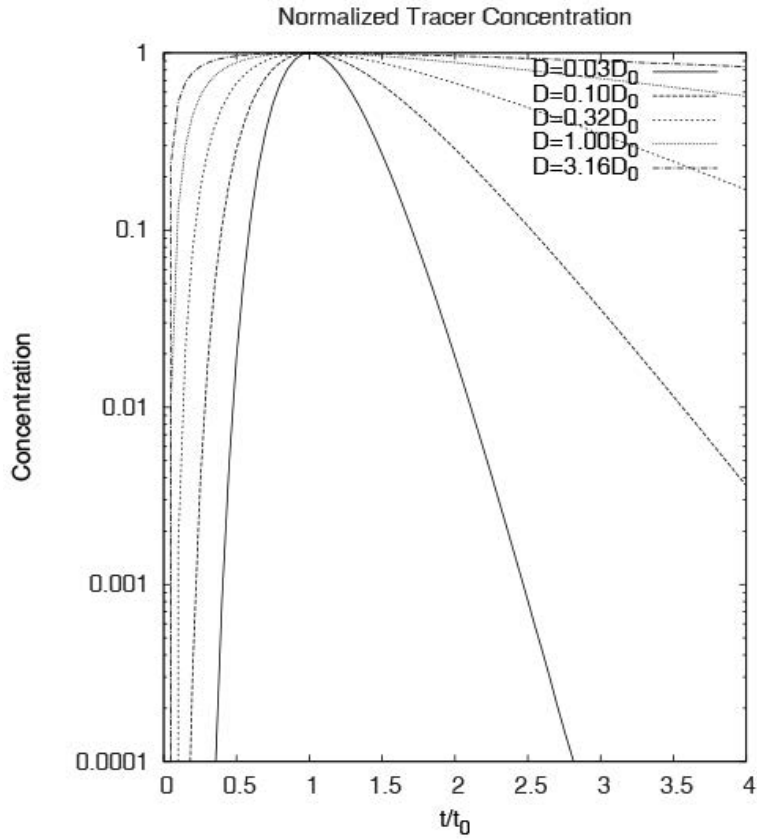
Figure A-1: Functional fits to arrival times of conservative tracers. Soda Lake data [2, 3] are well fit by $D = 0.35 D_0$, where the characteristic $D_0 \equiv \ell v \equiv v^2 t_0$, where t_0 is the time between tracer injection and its peak concentration at the production well at a distance ℓ and $v = \ell/t_0$. D/D_0 is a fitting parameter that describes the shape of $f(t)$; D is not a physical diffusivity. A similar value of D/D_0 fits the tracer data from the Soultz II experiment [8].

the surrounding rock. If the porosity $\phi \ll 1$, so the thermal energy content of the water is negligible, the temperature T_r of the rock satisfies the equation, almost identical to that (Eq. A-20) describing the transport of tracers,

$$\frac{\partial T_r}{\partial t} - D_r \nabla^2 T_r + \phi \frac{C_w}{C_r} \vec{\nabla} \cdot (\vec{v} T_r) = 0. \qquad \text{(A-23)}$$

From the derivation of Section A.1, replacing the flow length scale ℓ by the thermal diffusion scale ℓ_T, we find that the assumption that the water temperature is close to the local rock temperature ($\Delta T_w \gg \Delta T_r$) is valid if

$$2\frac{C_r}{C_w}\frac{D_r}{vb} \gg 1. \qquad \text{(A-24)}$$

For the parameters found for Soda Lake in Section A.2, this inequality is satisfied by a factor of about 10. With these assumptions it is not necessary to consider a separate equation for the water temperature, because it is always close to the rock temperature, and the rock temperature can be used in the advective term in Eq. A-23.

We are interested in solutions of Eq. A-23 for injection of "cool" water at $x = 0$. This corresponds, in a nominal plane crack geometry, to the conditions

$$T(0, t) = T_c, \qquad \text{(A-25)}$$

$$T(x, 0) = T_h. \qquad \text{(A-26)}$$

The solution is a thermal wave (a cold front) advancing with the speed

$$v_{front} = \phi(C_w/C_r)v \qquad \text{(A-27)}$$

and broadened to a width

$$\ell_f \approx \min\left(\frac{D_r}{v_{front}}, \sqrt{D_r t_{front}}\right), \qquad \text{(A-28)}$$

where $t_{front} = x_{front}/v_{front}$ is the time since the thermal wave was initiated. The first term, representing advective narrowing of the diffusion front, is controlling (is smaller than the second term) after the front has advanced a

113

distance $D_r/(\phi v C_w/C_r) = \mathcal{O}(1\,\mathrm{m})$, using the estimates of ϕ in Section A.7. As a result, a constant temperature boundary condition at $x = 0$ drives a thermal wave that continually overtakes the diffusion front after a time $\mathcal{O}(D_r/v_{front})$.

A.5.1 Thermal bypass type II

The effect of different mean flow speeds on different sheets or bundles of streamlines is that the cooling front advances at different rates on these sheets or bundles. Once the fastest advancing portion of the front reaches the production well those streamlines begin to deliver water at the injection temperature, and Type II thermal bypass begins (tracer data from Soda Lake indicate that, at least at that site, on no significant fraction of the streamlines is flow fast enough for there to be Type I thermal bypass). This is the explanation of the low thermal recovery factors estimated for many EGS systems [9].

The function $f(t)$ measures the rate of arrival of fluid as well as of tracer. Normalizing $f(t)$ by $\int_0^\infty f(t)\,dt = 1$, mixing of hot (uncooled rock) and "cold" (injection temperature) fluid leads to a temperature in the production well as a function of time:

$$T_{prod}(\zeta t) = T_r \int_t^\infty f(t')\,dt' + T_i \int_0^t f(t')\,dt', \qquad \text{(A-29)}$$

where T_r is the initial rock temperature, T_i the injection temperature and $\zeta \equiv v/v_{front} = C_r/(\phi C_w)$. Because $\zeta \gg 1$ the flow of tracers on short time scales predicts the flow of heat on much longer (by a factor of $1/\zeta \approx 1/\phi$) time scales. These functional forms are shown in Figure A-2.

Eq. A-29 gives a quantitative prediction, within the validity of its assumptions, of Type II thermal bypass resulting from early cooling of rock that is close to streamlines of high admittance and high flow rate. This prediction is based directly on empirical data. Thermal bypass will begin after

114
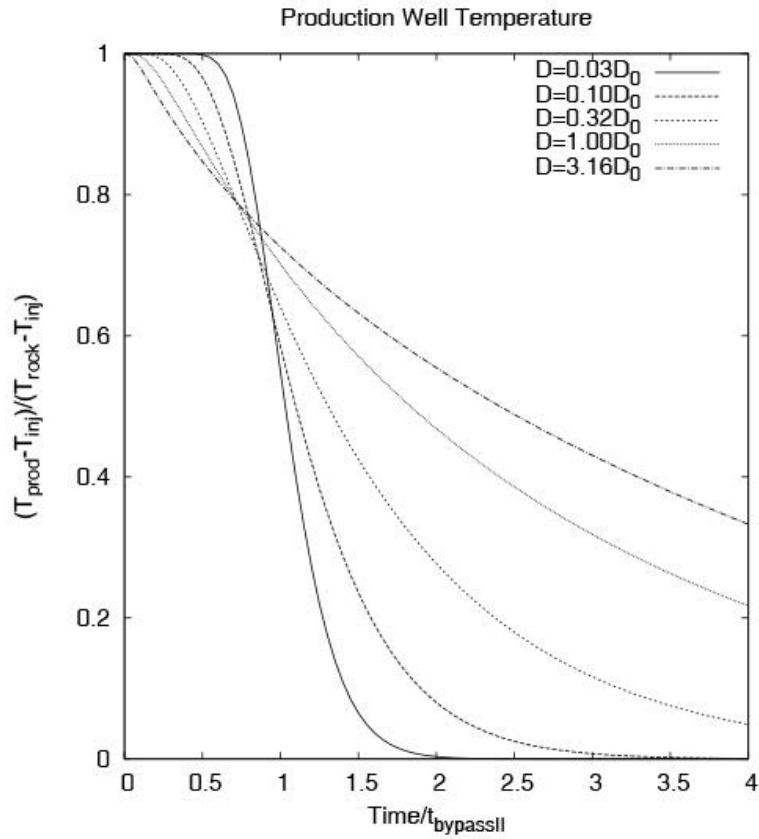
Figure A-2: Decay of produced water temperature predicted on the basis of distribution of tracer arrival times. The characteristic time $t_{bypassII} = t_0/(\phi C_w/C_r) \gg t_0$, where t_0 is the arrival time of the peak concentration in a conservative tracer experiment, ϕ is the porosity and C_w and C_r are the volumetric specific heats of water and rock. Bypass Type II refers to the early cooling of rock along streamlines of higher admittance and flow velocity.

a time

$$t_{bypassII} \sim \frac{\ell}{3v_{front}} = \frac{\ell}{3} \frac{C_r}{C_w} \frac{1}{\phi v} \sim 1 - 10 \, \text{yr}, \qquad \text{(A-30)}$$

where the range of numerical estimates corresponds to the uncertainty range 10^{-4}–10^{-3} of ϕ at Soda Lake (taking the same ΔP as in the tracer experiment), and the factor of 3 comes from the finding in the tracer experiment that the fastest measured fluid moves three times faster than the peak tracer concentration. Porosities of $\approx 10^{-4}$ were found at Habanero #1 and Soultz [9].

These predictions depend on the porosity ϕ because fluid and tracer are contained in the pores, while heat is extracted from the bulk rock. We have estimated ϕ as the volume of fluid injected in a tracer experiment at the time of tracer breakthrough to the production well divided by an estimated volume of the fractured (and available) resource that we have taken to be ℓ^3, the distance between injection and production wells (this should be their three-dimensional distance in the resource, not the distance between the wells at the surface, an important distinction if the cracks are near-vertical).

In practice, the volume effectively penetrated by flowing fluid may be much less than ℓ^3, so that the effective ϕ is larger and the thermal drawdown time (Thermal Bypass Type II) shorter. This only reflects the fact that heat in rock not penetrated by fluid is not available for extraction. Evaluation of ϕ is critical to determining the economic feasiblity of EGS on the basis of tracer experiments, making independent determination of the penetrated volume important. One possible estimate of the thermally accessible volume might be the volume of fractured rock inferred from microseismic mapping during stimulation.

A.6 What Determines the Width of Cracks?

We inferred from the Soda Lake tracer experiment that cracks have widths of roughly $30 \, \mu$. Further, it is evident from the arrival time distribution of tracers in that experiment that almost none ($\lesssim 10^{-3}$) of the stream

lines have arrival times less than three times that of the most abundant (in other words, mean velocities more than three times the mean, or crack widths more than twice the mean).

Casual examination of granite, the rock making up most hot dry rock resources, shows crystallites of mm–cm dimension, much larger than the inferred crack widths. There are two possible interpretations of this:

- The cracks are held open by fine crack gouge, whose grain sizes are much less than crystallite sized, perhaps because it is comminuted as the crack faces rub on each other. The production of finely comminuted rock is well known, and the cause of miners' silicosis.

- The flow impedance of the streamlines is dominated by very narrow constrictions, and everywhere but at those constrictions cracks are much wider than their nominal widths inferred from the flow speed. This is implausible because the distribution of such constrictions must be random and uncorrelated on longer length scales, and flow would be dominated by a "tail" of streamlines without narrow constrictions (recall that the volume flow rate is proportional to the -3 power of the crack width). No such early arrival tail is present in the Soda Lake tracer data, which indicate a remarkably monodisperse distribution of streamline impedances $\mathcal{A}$.

A.7   Rock Elasticity

The pore volume in the Soda Lake test has been estimated [2] as 38,000–46,000 m^3. Comparing to the nominal volume ℓ^3 suggests a porosity $\phi = 10^{-4}$–10^{-3}, where our ignorance of the effective rock volume of the resource does not justify more than an order-of-magnitude estimate.

The compressibility of water at S.T.P. is $C_w = 4.4 \times 10^{-11}$ cm^3/erg. Readily available data [7] only extend to 100 °C and 1 kbar, and must be

extrapolated in temperature (but not in pressure) to hot dry rock conditions; extrapolation indicates that even at $200\,°C$ C_w is within 20% of its value at S.T.P. The compressibility of granite $C_g = 2 \times 10^{-12}$ cm^3/erg. The compressibility of the fractured hot rock is

$$C_r = (1 - \phi)C_g + \phi C_w \approx C_g \qquad \text{(A-31)}$$

to high accuracy because ϕ is so small.

When a pressure P is applied at an injection well the pressurized volume V expands by approximately $\Delta V = VP/C_r$. For $\phi \ll C_w/C_r$ this is larger than the initial crack volume (as may be seen by considering the limit $\phi \to 0$). For a numerical estimate, consider $P = 100$ bars and $V = 0.1$ km^3; then $\Delta V \approx 2 \times 10^4$ m^3, the linear strain $u = \Delta V/(3V) = PC_r/3 \approx 7 \times 10^{-5}$ and the displacement $\Delta \ell \approx u\ell \approx 3$ cm. This is in the pressurized rock; surface displacements are less by a factor $\mathcal{O}(\ell^2/d^2)$ where d is the depth of the volume of fluid injection (in fact, the stress field extends to the surface).

We assume that the crack volume also expands by $\mathcal{O}(\Delta V)$ (this is not a trivial assumption because pressurizing uncracked competent rock will not open voids). If the injection pressure is removed, the rock pressure, relaxing to its value with empty cracks, will tend to expel the fluid. This will not occur instantaneously. The fluid flow rate

$$\frac{dV_f}{dt} = -AP \qquad \text{(A-32)}$$

and the volume created by dilation of the rock matrix for fluid is

$$V_f = VPC_r. \qquad \text{(A-33)}$$

The solution is

$$V_f = V_{v0} \exp\left(-t/t_{drain}\right), \qquad \text{(A-34)}$$

with the drainage time

$$t_{drain} = \frac{V}{AC_r}. \qquad \text{(A-35)}$$

For the parameters ($V \approx 0.1$ km^3, $A = 10$ l/s-bar, $C_r = 2 \times 10^{-6}$/bar) appropriate to the Soda Lake site, t_{drain} is a few days.

A.8   Paying for the Pressure Drop

A pressure drop ΔP between injection and production wells is equivalent to a loss in produced temperature

$$\Delta T_{loss} = \frac{\Delta P - \Delta P_{ts}}{C_p}\left(\frac{1}{\epsilon} - 1\right) = 2.4\,°\mathrm{C}\left(\frac{1}{\epsilon} - 1\right)\frac{\Delta P - \Delta P_{ts}}{100\,\mathrm{bars}}, \qquad \text{(A-36)}$$

where C_p is the volumetric specific heat of water, ΔP_{ts} is the thermosyphon contribution to ΔP and ϵ is an efficiency that includes the inefficiencies both of the pump and of the generation of electricity from thermal energy. The subtracted unity allows for the recovery of the viscous work in the enthalpy of the produced fluid.

The loss is significant; for plausible $\epsilon = 0.1$–0.2 and $\Delta P - \Delta P_{ts} = 100$ bar $\Delta T_{loss} = 10$–$20\,°\mathrm{C}$. This must be compared to a representative temperature difference between production and injection wells of roughly $100\,°\mathrm{C}$ that is available to drive a heat engine. The pumps required to provide the pressure head ΔP also require a significant capital expense.

A.8.1   Thermosyphons

For thermosyphon-pumped CO_2 EGS $\Delta T_{loss} = 0$, and is less than the value in Eq. A-36 if the thermosyphon is a partial contribution to pumping. The thermosyphon effect is significant even for water. The thermal expansion coefficient of water in the range 50–$200\,°\mathrm{C}$ is roughly $0.001/°\mathrm{C}$ (the pressure is often not specified in tables, but is likely to be the vapor pressure at $T > 100\,°\mathrm{C}$ and 1 bar at lower pressures; even at $200\,°\mathrm{C}$ the vapor pressure is only 15.5 bars and the effect of compressibility only about 0.1%). From $60\,°\mathrm{C}$ to $180\,°\mathrm{C}$ the density drops by 0.10 g/cm^3, so that for wells 3 km deep $\Delta P_{ts} = 30$ bars, a significant reduction in the required driving pressure and mitigation of the pumping loss. In confirmation, in the Soda Lake test the injection rate was 800 gpm at $70\,°\mathrm{C}$ and the production rate 885 gpm at $190\,°\mathrm{C}$ [5], a flow rate difference consistent with the expected 10% dilation upon heating if no mass is lost (loss of conservative tracer may be explained

if some of the injected fluid remains in the formation, displacing produced fluid that was present before the test).

A.9 Wholly Drilled Heat Exchanger

We consider the possibility of drilling narrow pipes between the injection and production wells. In a heat extraction time $t_r = 10$ yr a pipe will extract heat from a region of rock extending a distance $\sqrt{D_r t_r} \approx 16$ m around the pipe. The extracted thermal energy is $\pi D_r t_r C_r \Delta T \approx 2 \times 10^9$ J/cm, where we have taken $\Delta T = 100\,°$C, at a mean power of 6 W/cm, or 0.6 MW/km. To exploit a cubic-km region of hot dry rock would require $\mathcal{O}(1000)$ boreholes in an array with approximately 30 m spacing.

The cost of drilling has been estimated to be \$5,000-10,000/m for larger wells in softer rock, possibly at shallower depths. For lack of better information, we adopt those numbers, and ignore other costs. The drilling cost is then \$2.5–5 $\times 10^{-8}$/J, or \$0.09–0.18/kWh$_t$. For a plausible efficiency of power generation of 15%, the cost of producing electric power attributable to drilling alone is \$0.60–1.20/kWh$_e$. This cannot be economic unless the drilling cost is reduced by more than an order of magnitude.

It is conceivable that the cost of drilling small diameter holes at depth could be much less. Coiled tubing drilling (`www.petrowiki.org/Coiled_tubing_drilling`) is an established method for drilling small diameter holes, either shallow (for construction, emplacement of sensors, *etc.*) or re-entering completed oil wells, and might be adapted to this problem. However, the feasibility and cost of doing so in hot hard rock at great depth remain to be demonstrated.

Even a narrow diameter borehole may have a large fluid admittance. For example, for the previously discussed 0.6 MW$_t$ and $\Delta T = 100\,°$C, the flow rate is 1.4 l/s. In a $1''$ diameter borehole the mean velocity is 2.8 m/s, the Reynolds number is about 2.6×10^5, the friction factor $f = 0.038$ for an

assumed surface roughness of $0.01''$ and the pressure drop is 60 bar/km or 6 MPa/km. The fluid admittance for a single 1 km long borehole $A = .024$ l/s-bar or 0.24 l/s-MPa. For the array of 1000 boreholes in parallel (with a total thermal power of 600 MW$_t$ and electrical power 100 MW$_e$) the admittance would be $A = 24$ l/s-bar or 240 l/s-MPa. These parameters are consistent with those usually discussed for EGS.

B   APPENDIX: Heat Transfer in EGS

B.1   Introduction

We consider coupled one-dimensional models for temperature evolution in geothermal energy conversion. We begin with a simple water-channel geometry: thin planar fractures of dimension $b \times \Delta y \times z_{\mathrm{ex}}$ in x, y, and z, respectively, with z taken to be positive upward (toward the surface) and with $b << \Delta y$. To gain insight into time scales that are important for EGS energy production, we analyze the relatively simple case of parallel planar channels separated by a distance w in dry rock. See Fig. B-1. We consider and quantify three time scales:

1. Initial phase: In the short initial phase, the rock temperature at the interface with the water has not yet dropped much and the heat transfer to the water is governed by the convective heat-transfer coefficient, h.

2. Intermediate phase: In this phase the water and the rock surface at a given height, z, are at approximately the same temperature, and the heat transfer to the water is limited by conduction of heat from within the rock to the rock surface. The water's exiting temperature is relatively close to the initial bulk-rock temperature, because rock near the exit of the heat-transfer zone has not yet cooled significantly. (The cooling of the rock happens faster at the bottom of the heat-transfer zone, where cold water is injected, than at the top, where the water has been heated.) We assume constant mass flow rate during the intermediate phase.

3. Late phase: During this phase the temperature gradient in the rock all along the channel, including at the top, drops with time, and thus the energy-transfer rate to the water must drop with time. If the flow rate were to remain constant, both the energy transfer rate and the water's

exit temperature would drop in proportion to $1/\sqrt{t}$. This would lead to an electrical power output that would drop in proportion to $1/t$. However, if the flow rate is decreased in proportion to $1/\sqrt{t}$, the water's exit temperature can remain constant and electrical power output could diminish more slowly, in proportional to $1/\sqrt{t}$.

In the simple planar case depicted in Fig. B-1, we assume a water channel (or crack) of width b, depth Δy, and height $z_{\text{ex}} >> b$, with water flowing upward at speed v. We assume a symmetry boundary at the center of the water channel, $x = -b/2$, and the center of the rock, $x = w/2$.
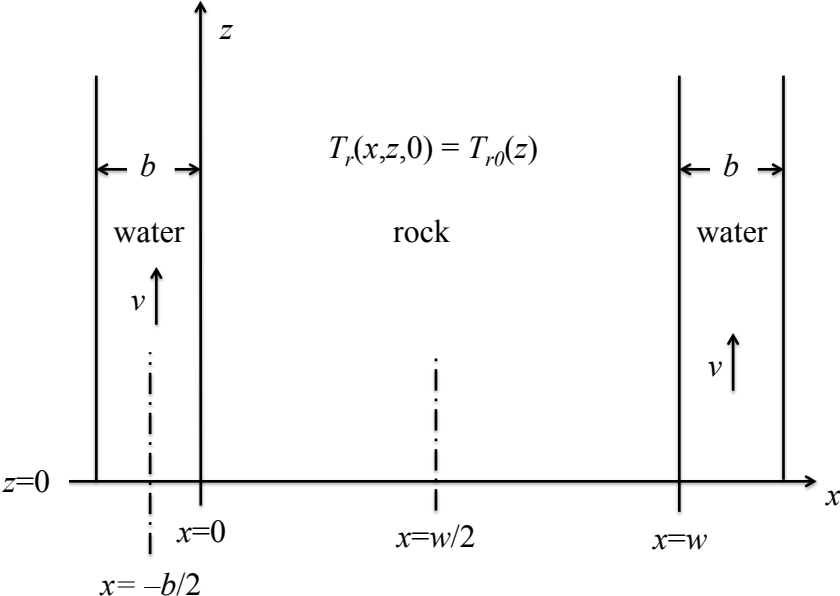

Figure B-1: Planar channels of width b separated by rock of width w. Length Δy is perpendicular to the plane of the figure, and the vertical extent of the channel is from the injection depth $(z = 0)$ to the exit of the heat-transfer zone $(z = z_{\text{ex}})$. Figure is not to scale; b is envisioned to be $<< w$ in an actual system.

B.2 Model Equations

We define the following notation to describe material parameters, temperatures, and flow parameters:

$$T_{r0}(z) = \text{initial rock temperature}$$

$$T_{w0} = \text{water injection temperature at } z = 0$$

To model heat conduction in the rock we assume that temperature gradients in x are much larger than those in y or z. The resulting model is then one-dimensional in x:

$$\rho_r c_r \frac{\partial T_r}{\partial t} = \vec{\nabla} \cdot k_r \nabla T_r \approx k_r \frac{\partial^2 T_r}{\partial x^2} \tag{B-1}$$

$$\Rightarrow \frac{\partial T_r}{\partial t} = \kappa_r \frac{\partial^2 T_r}{\partial x^2} \ , \tag{B-2}$$

where

$$T_r\,(x, y, z) = \text{rock temperature (see Fig. B-1 for coordinate system)} \ ,$$

$$\rho_r = \text{rock density,}$$

$$c_r = \text{rock specific heat,}$$

$$k_r = \text{rock thermal conductivity,}$$

$$\kappa_r = \text{rock thermal diffusivity.}$$

Our model equations for energy transfer to the water are

$$\frac{b}{2} \rho_w c_w v \frac{\partial T_w}{\partial z} = h \left(T_r(0, z, t) - T_w(z, t) \right) \ , \tag{B-3}$$

$$h \left(T_r(0, z, t) - T_w(z, t) \right) = k_r \left. \frac{\partial T_r}{\partial x} \right|_{x=0} . \tag{B-4}$$

where

$$T_w\,(z, t) = \text{water temperature}$$

$$\rho_w = \text{water density,}$$

$$c_w = \text{water specific heat,}$$

$$h = \text{convective heat-transfer coefficient,}$$

$$v = \text{water flow speed.}$$

Along with the model heat-transfer equations we impose initial and boundary conditions:

$$T_r(x, z, t)|_{t=0} = T_{r0}(z) = \text{known initial rock temperature,} \quad \text{(B-5)}$$

$$T_w(z, t)|_{z=0} = T_{w0} = \text{known injection temperature,} \quad \text{(B-6)}$$

$$k_r \frac{\partial T_r}{\partial x}\bigg|_{x=0} = h \left(T_r(0, z, t) - T_w(z, t) \right) , \quad \text{(B-7)}$$

$$\frac{\partial T_r}{\partial x}\bigg|_{x=w/2} = 0 . \quad \text{(B-8)}$$

We make the reasonable simplifying approximation that the initial rock temperature increases linearly with depth:

$$T_{r0}(z) \approx T_{r0}(0) + z \frac{dT_{r0}}{dz} = T_{r0}(0) - z \left| \frac{dT_{r0}}{dz} \right| . \quad \text{(B-9)}$$

It is convenient to describe new temperature variables, which are the *changes* in the rock and water temperatures relative to the initial rock temperature:

$$\theta_r(x, z, t) \equiv T_{r0}(z, t) - T_r(x, z, t) , \quad \text{(B-10)}$$

$$\theta_w(z, t) \equiv T_{r0}(z, t) - T_w(z, t) , \quad \text{(B-11)}$$

We write the model equations in terms of the new variables:

$$\frac{\partial \theta_r}{\partial t} = \kappa_r \frac{\partial^2 \theta_r}{\partial x^2} , \quad \text{(B-12)}$$

$$\frac{b}{2} \rho_w c_w v \left[\frac{\partial \theta_w}{\partial z} - \frac{\partial T_{r0}}{\partial z} \right] = h \left(\theta_{\text{int}}(z, t) - \theta_w(z, t) \right) , \quad \text{(B-13)}$$

and also the boundary and initial conditions:

$$\theta_r(x, z, t)|_{t=0} = 0 , \quad \text{(B-14)}$$

$$\theta_w(z, t)|_{z=0} = T_{r0}(z)|_{z=0} - T_{w0} \equiv \theta_{w0} , \quad \text{(B-15)}$$

$$k_r \frac{\partial \theta_r}{\partial x}\bigg|_{x=0} = h \left(\theta_{\text{int}}(z, t) - \theta_w(z, t) \right) , \quad \text{(B-16)}$$

$$\frac{\partial \theta_r}{\partial x}\bigg|_{x=w/2} = 0 . \quad \text{(B-17)}$$

126

We have also introduced a variable that describes the rock-surface temperature at the rock/water interface:

$$\theta_{\text{int}}(z, t) \equiv \theta_r(0, z, t) = T_r(0, z, t) - T_{r0}(z) \ . \tag{B-18}$$

The rock-temperature equation (B-12) is one-dimensional in x, while the water-temperature equation (B-13) is one-dimensional in z. The two are coupled through Eq. (B-16) and the right-hand side of Eq. (B-13). Although different z positions in the rock are not directly coupled in the rock-temperature equation, they are indirectly coupled through the water-temperature equation, so heat transfer from rock to water at a given z is affected by the transfer at all lower (deeper) values of z.

Similar equations hold for an array of cylindrical water channels.

B.3 Rock and Water Parameters

The analysis in this appendix is intended to provide quantitative insight into the temporal evolution of an EGS system in hot dry rock with water flowing through fractures. We take the following typical values of rock and water parameters for the calculations that follow.

$$\rho_w \approx 0.8 \text{g/cm}^3 \ ,$$
$$c_w \approx 4 \text{J/g-K} \ ,$$
$$k_r \approx 2 \text{W/m-K} \ ,$$
$$\kappa_r = k_r/(c_r\rho_r) \approx 10^{-6}\text{m}^2/\text{s} \ ,$$

We also define volumetric specific heats:

$$C_w \equiv c_w\rho_w \ , \tag{B-19}$$
$$C_r \equiv c_r\rho_r \ . \tag{B-20}$$

The convective heat-transfer coefficient is approximately

$$h = k_w Nu/D_H, \tag{B-21}$$

where Nu is the Nusselt number and D_H in our case is twice the width of the water channel, $2b$. If flow is laminar and the water channel is planar, then Nu takes a value of approximately 8 ([1], Table 10-6). The thermal conductivity of water at 275 C is around 0.6 W/m-K [same chapter of same reference]. This yields

$$h \approx \frac{2.4\text{W/m-K}}{b} \ .$$

If flow is turbulent, Nu and h will be larger than this. As we shall see below, even with the (smaller) laminar value, h is large enough in the EGS systems of interest that the water and rock-surface temperatures will quickly equilibrate.

B.4 Initial Phase

At very early times the "cooling wave" has not penetrated far into the rock, and the rock-temperature boundary condition at $x = w/2$ can be replaced by the following.

$$\theta_r(x, z, t)|_{x \to \infty} = 0 \ . \tag{B-22}$$

We can formally solve the rock-temperature equation in terms of the

(yet unknown) interface-temperature variable θ_{int}:

$$\theta_r(x, z, t) = \int_0^t dt' \, \theta_{\text{int}}(z, t') \frac{\partial}{\partial t'} \left[\text{erf}\left(\frac{x}{\sqrt{4\kappa_r(t - t')}} \right) \right]$$

$$= \left[\theta_{\text{int}}(z, t') \text{erf}\left(\frac{x}{\sqrt{4\kappa_r(t - t')}} \right) \right]_{t'=0}^{t'=t}$$

$$- \int_0^t dt' \, \frac{\partial \theta_{\text{int}}(z, t')}{\partial t'} \text{erf}\left(\frac{x}{\sqrt{4\kappa_r(t - t')}} \right)$$

$$= \theta_{\text{int}}(z, t) - \theta_{\text{int}}(z, 0) \text{erf}\left(\frac{x}{\sqrt{4\kappa_r(t)}} \right)$$

$$- \int_0^t dt' \, \frac{\partial \theta_{\text{int}}(z, t')}{\partial t'} \text{erf}\left(\frac{x}{\sqrt{4\kappa_r(t - t')}} \right)$$

$$= \theta_{\text{int}}(z, t) - \int_0^t dt' \, \frac{\partial \theta_{\text{int}}(z, t')}{\partial t'} \text{erf}\left(\frac{x}{\sqrt{4\kappa_r(t - t')}} \right) \quad . \qquad \text{(B-23)}$$

Here erf is the error function:

$$\text{erf}(\tau) \equiv \frac{2}{\sqrt{\pi}} \int_0^\tau du \, e^{-u^2} \quad . \qquad \text{(B-24)}$$

It follows that

$$
\begin{aligned}
k_r \left. \frac{\partial \theta_r(x,z,t)}{\partial x} \right|_{x=0} &= 0 - k_r \int_0^t dt' \, \frac{\partial \theta_{\text{int}}(z,t')}{\partial t'} \left[\frac{\partial}{\partial x} \text{erf}\left(\frac{x}{\sqrt{4\kappa_r(t-t')}} \right) \right]_{x=0} \\
&= -k_r \int_0^t dt' \, \frac{\partial \theta_{\text{int}}}{\partial t'} \left[\frac{\frac{2}{\sqrt{\pi}} \exp\left(-\frac{x^2}{4\kappa_r(t-t')} \right)}{\sqrt{4\kappa_r(t-t')}} \right]_{x=0} \\
&= -k_r \int_0^t dt' \, \frac{\partial \theta_{\text{int}}}{\partial t'} \left[\frac{1}{\sqrt{\pi \kappa_r(t-t')}} \right] \\
&= -\frac{k_r}{\sqrt{\pi \kappa_r t}} \int_0^t dt' \, \frac{\partial \theta_{\text{int}}}{\partial t'} \sqrt{\frac{t}{t-t'}} \\
&= -\frac{k_r}{\sqrt{\pi \kappa_r t}} \int_0^t dt' \, \frac{\partial \theta_{\text{int}}}{\partial t'} \left[1 - 1 + \left(\frac{t}{t-t'} \right)^{\frac{1}{2}} \right] \\
&= -\frac{k_r}{\sqrt{\pi \kappa_r t}} \left\{ \theta_{\text{int}}(z,t) - \theta_{\text{int}}(z,0) \right. \\
&\qquad \left. - \int_0^t dt' \, \frac{\partial \theta_{\text{int}}}{\partial t'} \left[1 - \left(\frac{t}{t-t'} \right)^{\frac{1}{2}} \right] \right\} \\
&= -\frac{k_r}{\sqrt{\pi \kappa_r t}} \left\{ \theta_{\text{int}}(z,t) + \int_0^t dt' \, \frac{\partial \theta_{\text{int}}}{\partial t'} \left[\left(\frac{t}{t-t'} \right)^{\frac{1}{2}} - 1 \right] \right\} .
\end{aligned}
$$

$$ \tag{B-25} $$

By Eq. (B-16) we have:

$$
\begin{aligned}
&\theta_{\text{int}}(z,t) - \theta_w(z,t) \\
&\qquad = -\frac{k_r/h}{\sqrt{\pi \kappa_r t}} \left\{ \theta_{\text{int}}(z,t) + \int_0^t dt' \, \frac{\partial \theta_{\text{int}}}{\partial t'} \left[\left(\frac{t}{t-t'} \right)^{\frac{1}{2}} - 1 \right] \right\}
\end{aligned}
$$

or

$$
\theta_{\text{int}}(z,t) = \frac{\theta_w(z,t) - \frac{k_r/h}{\sqrt{\pi \kappa_r t}} \int_0^t dt' \, \frac{\partial \theta_{\text{int}}}{\partial t'} \left[\left(\frac{t}{t-t'} \right)^{\frac{1}{2}} - 1 \right]}{1 + \frac{k_r/h}{\sqrt{\pi \kappa_r t}}} . \tag{B-26}
$$

It follows that the water and rock-surface temperatures equilibrate after a sufficiently long time:

$$
\theta_{\text{cl}}(z,t) \xrightarrow{t > t_{\text{init}}} \theta_w(z,t) , \tag{B-27}
$$

130

where t_{c1}, the first "critical time," is the transition time from the "initial" to the "intermediate" time phase. This is the time at which the governing dimensionless parameter in Eq. (B-26) becomes small:

$$\frac{k_r/h}{\sqrt{\pi \kappa_r t_{c1}}} << 1 \Rightarrow t_{c1} >> \frac{k_r^2}{h^2 \pi \kappa_r} \ . \tag{B-28}$$

We can solve for this initial-phase time scale using the numerical values of the material parameters listed previously:

$$t_{c1} >> \frac{(2\text{W/m-K})^2}{\left(\frac{2.4\text{W/m-K}}{b}\right)^2 \pi 10^{-6}\text{m}^2/\text{s}} \approx (2 \times 10^5 \text{s}) \left(\frac{b}{1\ \text{m}}\right)^2$$

$$\Rightarrow t_{c1} >> (20\text{s}) \left(\frac{b}{1\ \text{cm}}\right)^2 \ . \tag{B-29}$$

Thus, for crack widths of 1 cm or smaller, the water and rock-surface temperatures will equilibrate on a time scale of minutes to hours. Thus, for the time periods of interest to EGS we can assume that these temperatures are equilibrated.

B.5   Intermediate Time Period

Recall the water-temperature equation (B-13), taking into account Eq. (B-16)

$$\frac{b}{2}\rho_w c_w v \left[\frac{\partial \theta_w}{\partial z} - \frac{\partial T_{r0}}{\partial z}\right] = k_r \frac{\partial \theta_r}{\partial x} \ . \tag{B-30}$$

Now employ Eq. (B-25) with water and rock-surface temperatures equilibrated:

$$\frac{b}{2}\rho_w c_w v \left[\frac{\partial \theta_w}{\partial z} - \frac{\partial T_{r0}}{\partial z}\right]$$

$$= -\frac{k_r}{\sqrt{\pi \kappa_r t}} \left\{\theta_w(z,t) + \int_0^t dt' \frac{\partial \theta_{\text{int}}}{\partial t'}\left[\left(\frac{t}{t-t'}\right)^{\frac{1}{2}} - 1\right]\right\} \ ,$$

or

$$\frac{\partial \theta_w}{\partial z} = -\frac{1}{\lambda(t)}\left\{\theta_w(z,t) + F(z,t)\right\} + \frac{\partial T_{r0}}{\partial z} \ , \tag{B-31}$$

131

where

$$\lambda(t) \equiv \frac{bv\rho_w c_w \sqrt{\pi \kappa_r t}}{2k_r} ,$$ (B-32)

$$F(z,t) \equiv \int_0^t dt' \frac{\partial \theta_{\text{int}}}{\partial t'} \left[\left(\frac{t}{t-t'} \right)^{\frac{1}{2}} - 1 \right]$$ (B-33)

The solution is

$$\begin{aligned}
\theta_w(z,t) &= \theta_{w0} e^{-z/\lambda(t)} - \int_0^z dz' \left[\frac{F(z',t)}{\lambda(t)} + \left| \frac{dT_{r0}}{dz} \right| \right] e^{-(z-z')/\lambda(t)} \\
&= \theta_{w0} e^{-\frac{z}{\lambda(t)}} - \lambda(t) \left| \frac{dT_{r0}}{dz} \right| \left(1 - e^{-\frac{z}{\lambda(t)}} \right) - \int_0^z dz' \frac{F(z',t)}{\lambda(t)} e^{-\frac{z-z'}{\lambda(t)}} \\
&= \theta_{w0} e^{-\frac{z}{\lambda(t)}} - \lambda(t) \left| \frac{dT_{r0}}{dz} \right| \left(1 - e^{-\frac{z}{\lambda(t)}} \right) - \langle F(t) \rangle_0^z \left(1 - e^{-\frac{z}{\lambda(t)}} \right) .
\end{aligned}$$ (B-34)

Here $\langle F(t) \rangle_0^z$ is an appropriately weighted average of F over the interval $(0, z)$ at time t. We can rewrite the equation in terms of actual water temperature:

$$\begin{aligned}
T_w(z,t) = T_{r0}(z) - [T_{r0}(0) - T_{w0}] e^{-\frac{z}{\lambda(t)}} + \lambda(t) \left| \frac{dT_{r0}}{dz} \right| \left(1 - e^{-\frac{z}{\lambda(t)}} \right) \\
+ \langle F(t) \rangle_0^z \left(1 - e^{-\frac{z}{\lambda(t)}} \right) .
\end{aligned}$$ (B-35)

The length λ plays a central role in the water-temperature profile and thus in the performance of the EGS. The water exiting temperature is maximized when $\lambda \ll z_{\text{ex}}$, the height of the heat-transfer zone. If flow speed and crack geometry are constant during the intermediate time phase, then λ grows in proportion to $\sqrt{t}$, as is easily seen from Eq. (B-37). Thus, eventually λ will grow to exceed z_{ex} if flow conditions are constant.

Early in the intermediate time phase, for flow and crack parameters that make sense for energy production, we will have $\lambda \ll z_{\text{ex}}$. In this case, for z in the upper part of the heat-exchange zone (i.e., for $z > \lambda$) we will have:

$$T_w(z,t) \xrightarrow{z \gg \lambda} T_{r0}(z) + \lambda(t) \left| \frac{dT_{r0}}{dz} \right| + \langle F(t) \rangle_0^z .$$ (B-36)

132

The first two terms say that the water temperature at z, for $z \gg \lambda$, reaches the initial rock temperature at z with a correction for the vertical temperature gradient in the rock. The last term is a correction that is driven by the rate of change of the rock/water interface temperature. It is relatively small for $z \gg \lambda$ (see definition of F in Eq. (B-33) and the definition of the weighted average implied by Eq. (B-34)). Thus, for $z \gg \lambda$, water temperature at the exit of the heat-exchange zone is close to the initial temperature of the rock near the exit of the zone.

Under constant flow conditions, λ will grow until it equals the height of the heat-exchange zone, z_{ex}. By this time the exiting water temperature will be cooler than it was previously. We define the time of transition from the "intermediate" phase of EGS operation to the "final" phase, t_{c3}, to be the time at which $\lambda = z_{\mathrm{ex}}$:

$$\lambda(t_{c3}) = z_{\mathrm{ex}} = \frac{bvC_w\sqrt{\pi\kappa_r t_{c3}}}{2k_r} , \tag{B-37}$$

$$\Rightarrow t_{c3} = \frac{4k_r^2 z_{\mathrm{ex}}^2}{\pi\kappa_r b^2 v^2 C_w^2} = \frac{4C_r^2 \kappa_r^2 z_{\mathrm{ex}}^2}{\pi\kappa_r b^2 v^2 C_w^2} = \frac{4}{\pi}\left(\frac{C_r}{C_w}\frac{z_{\mathrm{ex}}}{bv}\right)^2 \kappa_r$$

$$= \frac{4(2 \text{ W/m-K})^2 z_{\mathrm{ex}}^2}{\pi(10^{-6} \text{ m}^2/\text{s})b^2 v^2(3.2 \text{ J/K-cm}^3)^2}$$

$$= 5 \times 10^5 \frac{z_{\mathrm{ex}}^2}{b^2 v^2}\frac{\text{cm}^6}{\text{m}^4\text{-s}}\frac{10^6 \text{ m}^2}{\text{km}^2}\frac{10^2 \text{ mm}^2}{\text{cm}^2}\frac{\text{m}^4}{10^8 \text{ cm}^4}$$

$$= \left[5 \times 10^5 \text{ s}\right]\left(\frac{z_{\mathrm{ex}}}{1 \text{ km}}\right)^2\left(\frac{1 \text{ mm}}{b}\right)^2\left(\frac{1 \text{ m/s}}{v}\right)^2$$

$$< [5.8 \text{ d}]\left(\frac{z_{\mathrm{ex}}}{1 \text{ km}}\right)^2\left(\frac{1 \text{ mm}}{b}\right)^2\left(\frac{1 \text{ m/s}}{v}\right)^2$$

$$< [1.6 \text{ y}]\left(\frac{z_{\mathrm{ex}}}{1 \text{ km}}\right)^2\left(\frac{1 \text{ mm}}{b}\right)^2\left(\frac{10 \text{ cm/s}}{v}\right)^2 . \tag{B-38}$$

We see that if the heat-exchange zone ≤ 1 km tall, the crack widths are ≥ 1 mm, and the flow speed is ≥ 1 m/s, then $\lambda = z_{\mathrm{ex}}$ after less than 6 days. If the heat-exchange zone is 1 km tall, and the product of crack width and flow speed is ≈ 10 (cm/s)(mm) $= 1$ cm^2/s, then the "intermediate" time phase will last approximately 1.6 years.

B.6 Power Generation

An important quantity is the energy transfer to a water channel per unit time—the "thermal" channel power, P_{th}^{ch}, which is proportional to the water flow rate and to the change in water temperature across the heat-exchange zone:

$$
\begin{aligned}
P_{th}^{ch} &= b\Delta y \; v \; c_w \rho_w \left[T_w(z_{\text{ex}}) - T_{w0} \right] \\
&= \dot{m}(4 \text{ J/g-K}) \left[T_w(z_{\text{ex}}) - T_{w0} \right] \\
&= (4 \text{ J/s}) \left(\frac{\dot{m}}{1 \text{ g/s}} \right) \frac{T_w(z_{\text{ex}}) - T_{w0}}{1 \text{ K}} \\
&= (4 \times 10^5 \text{ J/s}) \left(\frac{\dot{m}}{10^3 \text{ g/s}} \right) \frac{T_w(z_{\text{ex}}) - T_{w0}}{100 \text{ K}} \\
&= (400 \text{ kW}) \left(\frac{\dot{m}}{1 \text{ kg/s}} \right) \frac{T_w(z_{\text{ex}}) - T_{w0}}{100 \text{ K}} \;,
\end{aligned}
\tag{B-39}
$$

where

$$
\dot{m} \equiv b \, \Delta y \; v \; \rho_w = \text{mass flow rate.}
\tag{B-40}
$$

We see that if the water is heated by 100 Kelvin, a flow channel gains thermal energy at a rate of ≈ 400 kW for every kg/s of flow. Thermal energy gain rate is important, but the typical goal of an EGS station will be production of electrical power. We assume maximum efficiency of electricity generation such that the electrical power produced from the heated water satisfies:

$$
\begin{aligned}
P_e^{ch} &= P_{th}^{ch} \frac{T_{w,ex} - T_{w0}}{T_{w,ex}} \\
&\approx (400 \text{ kW}) \left(\frac{\dot{m}}{1 \text{ kg/s}} \right) \frac{(T_w(z_{\text{ex}}) - T_{w0})^2}{(100 \text{ K}) T_{w,ex}}.
\end{aligned}
\tag{B-41}
$$

This expression shows that water-temperature increase is doubly important in the sense that if it drops by a factor of f, electrical power output drops by a factor of f^2. From Eq. (B-35) we have the following expression for the water temperature increase:

$$
\begin{aligned}
\left[T_w(z_{\text{ex}}, t) - T_{w0} \right] &= \left[T_{r0}(z_{\text{ex}}) - T_{w0} \right] - \left[T_{r0}(0) - T_{w0} \right] e^{-\frac{z_{\text{ex}}}{\lambda(t)}} \\
&+ \lambda(t) \left| \frac{dT_{r0}}{dz} \right| \left(1 - e^{-\frac{z_{\text{ex}}}{\lambda(t)}} \right) + \langle F(t) \rangle_0^z \left(1 - e^{-\frac{z}{\lambda(t)}} \right) \; .
\end{aligned}
\tag{B-42}
$$

We discussed previously that the temperature increase is maximized when $\lambda << z_{\text{ex}}$, and that in this limit we have:

$$[T_w(z_{\text{ex}}, t) - T_{w0}] \xrightarrow{\lambda(t) << z_{\text{ex}}} \approx [T_{r0}(z_{\text{ex}}) - T_{w0}] + \lambda(t) \left| \frac{dT_{r0}}{dz} \right|$$

$$\approx T_{r0}(z_{\text{ex}} - \lambda) - T_{w0} . \qquad \text{(B-43)}$$

In the opposite limit, when $\lambda >> z_{\text{ex}}$, we find

$$[T_w(z_{\text{ex}}, t) - T_{w0}] \xrightarrow{\lambda(t) >> z_{\text{ex}}} \approx [T_{r0}(z_{\text{ex}}) - T_{w0}] - [T_{r0}(0) - T_{w0}] \left(1 - \frac{z_{\text{ex}}}{\lambda(t)} \right)$$

$$+ \lambda(t) \left| \frac{dT_{r0}}{dz} \right| \left(\frac{z_{\text{ex}}}{\lambda(t)} - \frac{1}{2} \left[\frac{z_{\text{ex}}}{\lambda(t)} \right]^2 \right) + \langle F(t) \rangle_0^{z_{\text{ex}}} \left(\frac{z_{\text{ex}}}{\lambda(t)} - \frac{1}{2} \left[\frac{z_{\text{ex}}}{\lambda(t)} \right]^2 \right)$$

$$\approx \left[T_{r0}(z_{\text{ex}}) + z_{\text{ex}} \left| \frac{dT_{r0}}{dz} \right| - T_{r0}(0) \right] - T_{w0} \frac{z_{\text{ex}}}{\lambda(t)}$$

$$+ \frac{z_{\text{ex}}}{\lambda(t)} \left[T_{r0}(0) - \frac{z_{\text{ex}}}{2} \left| \frac{dT_{r0}}{dz} \right| \right] + \langle F(t) \rangle_0^{z_{\text{ex}}} \left(\frac{z_{\text{ex}}}{\lambda(t)} \right)$$

$$\approx [T_{r0}(0) - T_{r0}(0)] - T_{w0} \frac{z_{\text{ex}}}{\lambda(t)}$$

$$+ \frac{z_{\text{ex}}}{\lambda(t)} [T_{r0}(z_{\text{ex}}/2)] + \langle F(t) \rangle_0^{z_{\text{ex}}} \left(\frac{z_{\text{ex}}}{\lambda(t)} \right)$$

$$\approx \frac{z_{\text{ex}}}{\lambda(t)} \left\{ T_{r0} \left(\frac{z_{\text{ex}}}{2} \right) - T_{w0} + \langle F(t) \rangle_0^{z_{\text{ex}}} \right\} . \qquad \text{(B-44)}$$

This shows that if the rock/water system ever reaches the condition $\lambda(t) >> z_{\text{ex}}$, the energy transfer rate to the water will be much smaller than it was during the intermediate phase, for the temperature increase of the water contains the multiplicative factor z_{ex}/λ, which is $<< 1$. This factor is squared in the equation for the electrical power output. It is likely that the EGS would become impractical to operate before this limit is reached.

We summarize the two limits we have established:

$$P_{th}^{ch} \approx \left(\frac{400 \text{ kW } \dot{m}}{1 \text{ kg/s}} \right) \begin{cases} \frac{T_{r0}(z_{ex} - \lambda(t)) - T_{w0}}{100 \text{ K}} , & \lambda(t) << z_{\text{ex}} , \\[3mm] \frac{z_{ex}}{\lambda(t)} \frac{T_{r0}\left(\frac{z_{ex}}{2} \right) - T_{w0} + \langle F(t) \rangle_0^{z_{ex}}}{100 \text{ K}}, & \lambda(t) >> z_{\text{ex}} . \end{cases} \qquad \text{(B-45)}$$

$$P_e^{ch} \approx \frac{400 \text{ kW } \dot{m}}{1 \text{ kg/s}} \begin{cases} \frac{(T_{r0}(z_{ex}-\lambda(t))-T_{w0})^2}{(100 \text{ K})T_{r0}(z_{ex}-\lambda(t))}, & \lambda(t) << z_{ex}, \\[3mm] \left(\frac{z_{ex}}{\lambda(t)}\right)^2 \frac{\left(T_{r0}\left(\frac{z_{ex}}{2}\right)-T_{w0}+\langle F(t)\rangle_0^{z_{ex}}\right)^2}{(100 \text{ K})\left[T_{w0}+\frac{z_{ex}}{\lambda(t)}\left(T_{r0}\left(\frac{z_{ex}}{2}\right)+\langle F(t)\rangle_0^{z_{ex}}\right)\right]}, & \lambda(t) >> z_{\text{ex}}. \end{cases}$$
(B-46)

For a concrete example, consider an initial bulk-rock temperature of 600 K at all depths, with water injected at 300 K. If we ignore the effects of the F term, we obtain

$$P_e^{ch} \xrightarrow{\text{example}} \frac{400 \text{ kW } \dot{m}}{1 \text{ kg/s}} \begin{cases} 1.5, & \lambda(t) << z_{\text{ex}}, \\[3mm] 0.74, & \lambda(t) = z_{\text{ex}}, \\[3mm] \left(\frac{z_{ex}}{\lambda(t)}\right)^2 \frac{1}{1+\frac{1}{3}\frac{z_{ex}}{\lambda(t)}}, & \lambda(t) >> z_{ex}. \end{cases}$$
(B-47)

Consider the case of constant mass flow rate, with t_{c3} defined such that $\lambda(t_{c3}) = z_{\text{ex}}$. We define the dimensionless time t/t_{if} and dimensionless electrical power $P_e^{ch}(t)/P_c^{ch}(t_{c1})$, where t_{c1} is the (very early) time at which the water temperature becomes in equilibrium with the rock-surface temperature (see previous section). We can plot the dimensionless power as a function of dimensionless time, at least if we ignore the effects of the F term (which is difficult to calculate and whose effects are not important for this discussion). The plot for constant flow conditions is shown in Fig. B-2. For this plot we have assumed that $T_{r0}(0) = 600$ K, $T_{r0}(z_{\text{ex}}) = 550$ K, and $T_{w0} = 300$ K.

We saw earlier that if the water exiting temperature decreases there is a dramatic effect on electrical power generation. We now suggest a flow strategy that can mitigate this effect. The strategy is to begin decreasing the water flow rate to keep $\lambda(t)$ constant once the power begins to drop significantly, for example at a time of approximately t_{c3}. λ will remain constant if flow rate decreases like $1/\sqrt{t}$. This flow strategy does not prevent a decrease in channel thermal power—this decrease is inevitable because the temperature gradient in the rock decreases—but it does prevent a loss of thermodynamic efficiency and thus keeps the electrical power higher than it
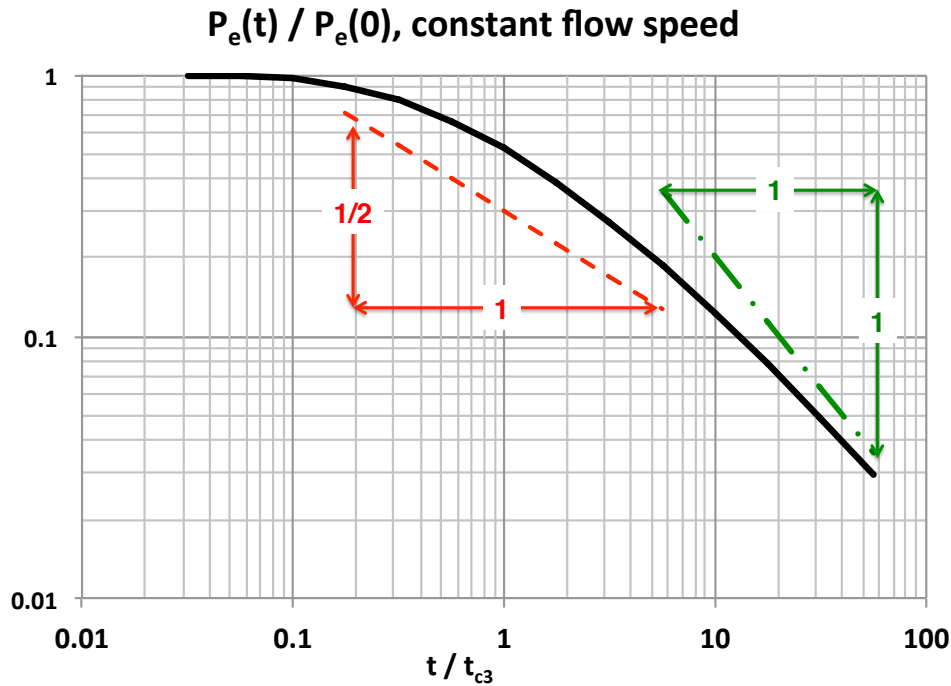
Figure B-2: Electrical power as a function of time for **constant flow** conditions after the brief "initial" time period. With constant flow conditions the electrical powerdrops to half of its initial value when t reaches t_{c3}, and drops more steeply afterward. At long times electrical power drops roughly as $1/t$ if flow rate remains constant.

otherwise would be. A plot of dimensionless electrical power with this flow strategy is shown in Fig. B-3. Comparison against Fig. B-2 shows that the decreasing flow strategy produces significant gains in electrical power relative to the constant-flow strategy, for $t > t_{c3}$.

Even with the decreasing-flow strategy the electrical power output drops by a factor of ≈ 6 by time $t = 10t_{c3}$ and by a factor of ≈ 10 by time $t = 30t_{c3}$. This appears unavoidable.

B.7 Effects of Finite Spacing

The equations in the previous sections assumed that the rock temperature in the center of the rock between channels (at $x = w/2$ in Fig. B-1)
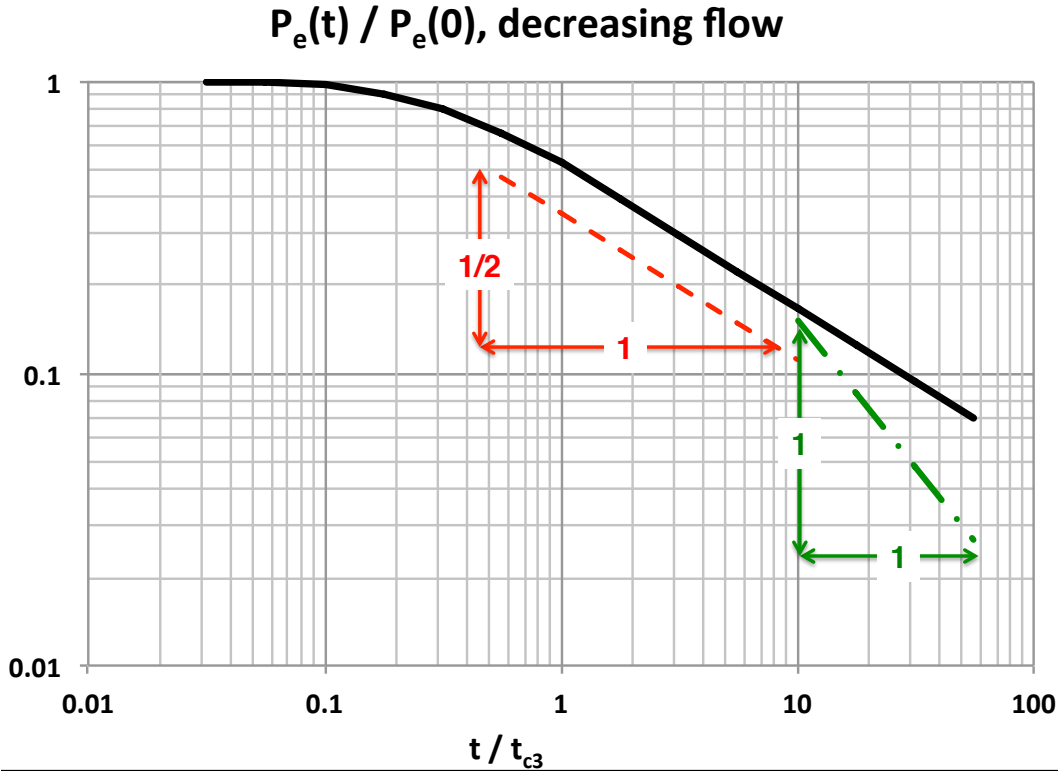
Figure B-3: Electrical power as a function of time for flow that is constant until $l(t){=}z_{ex}$, after which flow speed drops as $1/t^{1/2}$. Curves are shown for cases of $l(t){=}z_{ex}$ (i.e., $t{=}1$) at $t = 0.3$ yr, 1yr, and 3 yr. With this flow strategy, electrical power never drops faster than $1/t^{1/2}$.

remained at its initial value during the time periods of interest. In reality the "cooling waves" that emanate from the water channels will eventually meet in the center (at $x = w/2$), dropping the maximum temperature and causing the temperature gradients in the rock to decrease more quickly than the isolated-channel equations predict. This will happen at different times at different z heights, with different impacts on the performance of the EGS. It will happen first at the inlet (bottom) of the heat-exchange zone and will work its way upward. At the top of the zone, strong cooling waves are not launched until $t \approx t_{c3}$, because until then the water at the top of the zone is not much cooler than the local rock.

We can obtain rough estimates of the time at which the central rock temperature begins to drop from its initial value. If we seek a series solution

of the heat-transfer problem, with a symmetry boundary at $x = w/2$, we find that the nth mode decays at a rate of $\exp(-\kappa_r \beta_n t)$, where

$$\beta_n = \left(\frac{2\pi}{w+b}\right)^2 . \tag{B-48}$$

The time at which the second mode has decayed to 10% of the value of the first mode is given by

$$\frac{\exp\left(-\kappa_r \beta_2 t_{10}\right)}{\exp\left(-\kappa_r \beta_1 t_{10}\right)} = 0.1 ,$$

$$\Rightarrow \kappa_r(\beta_2 - \beta_1)t_{10} = 2.3 ,$$

$$\Rightarrow t_{10} = \frac{2.3}{\kappa_r(\beta_2 - \beta_1)} = \frac{2.3 \text{ s}}{\left(10^{-3}\text{m}\frac{2\pi}{w+b}\right)^2 (4 - 1)} ,$$

$$\approx 2 \times 10^4 \text{ s} \left(\frac{w}{1\text{m}}\right)^2 = 8 \times 10^6 \text{ s} \left(\frac{w}{20\text{m}}\right)^2$$

$$\approx 1 \text{ y} \left(\frac{w}{40\text{m}}\right)^2 . \tag{B-49}$$

Another estimate can be obtained from the isolated-channel model by finding time at which the model predicts a significant drop in the rock temperature at a distance of $w/2$ from the water channel. The error function equals 0.85 when its argument equals 1; thus, when $t = (w/2)^2/(4\kappa_r)$ the isolated-channel rock temperature at $x = w/2$ has moved 15% of the way toward the water temperature at the given height z. This yields a time estimate of the same order of magnitude as was obtained above.

Both of these estimates ignore the time-changing rock/water interface temperature. This "mixes" modes in the series solution and introduces correction terms in the isolated-channel solution. Nevertheless, it is reasonable to conclude that channels begin to communicate significantly after a time that scales like the square of the channel separation, with the clock starting once the rock surface begins cooling substantially. The clock starts sooner at the bottom of the heat exchanger than at the top.

Another conclusion is that the communication between water channels can only reduce the heat transfer to the water, relative to the isolated-channel case that was considered in detail above.

References

[1] N. E. Todreas and M. S. Kazimi, *Nuclear Systems I: Thermal Hydraulic Fundamentals*, Taylor and Francis, New York, 720 pp (1989).

[2] Reimus, P., *et al. Thirty-Seventh Workshop on Geothermal Reservoir Engineering* (Stanford U., Stanford, Cal. 2012) SGP-TR-194.

[3] Rose, P., *et al. Thirty-Seventh Workshop on Geothermal Reservoir Engineering* (Stanford U., Stanford, Cal. 2012) SGP-TR-194.

[4] Reimus, P. email to J. Katz July 24, 2013.

[5] Rose, P. email to J. Katz July 25, 2013.

[6] Rose, P. E. and Adams, M. C. *Geothermal Resources Council TRANSACTIONS* **18**, 237–240 (1994).

[7] Fine, R. A. and Millero, F. J. *J. Chem. Phys.* **59**, 5529 (1973).

[8] Jung, R. *EGS — Goodbye or Back to the Future*, Chap. 5 pp. 95–121 `http://dx.doi.org/10.5772/56458` (2013).

[9] Grant, M. A. and Garg, S. K. *Thirty-Seventh Workshop on Geothermal Reservoir Engineering* (Stanford U., Stanford, Cal. 2012) SGP-TR-194.